ABSTRACT

EMISSIVITY MEASUREMENTS AND MODELING OF SILICON RELATED MATERIALS AND STRUCTURES

by
Sufian Abedrabbo

The objective of this dissertation is to investigate the major issues concerning applications of pyrometry for applications in rapid thermal processing (RTP) of silicon related materials. The research highlights of this work are:

- Establishment of spectral emissometry as a novel, reliable and reproducible technique for:

  - Determination of wavelength and temperature dependent reflectivity, transmissivity, emissivity and temperature, simultaneously, of silicon related materials and structures. The emissometer operates in the wavelength range of 1-20μm and temperature range of 300-1200K.

  - The analysis of the influence of morphological effects on the radiative properties by measurement of (a) front-smooth incidence versus backside-rough incidence of single-side polished silicon wafers and (b) single versus double-side polished wafers. This is the first time in the literature that such a study is devoted to detect differences in the optical properties of the same sample. Attempts have been made to verify the Vandenabeele-Maex one-parameter model against the experimentally obtained optical properties for rough surfaces. The model has been proven to be inaccurate and inadequate for simulating the measured properties.

- Establishment of methodologies and schemes for deconvolution of the measured optical properties to yield the fundamental constants such as absorption coefficient α.

Effects of wavelength, temperature, the total available free carriers both by doping and thermal generation and doping types have been considered in the deconvolution process. Comparisons have been sought with the available knowledge of α in the literature by the extensive use of the Multi-Rad model. This is a state of the art model that has been developed by MIT/SEMATECH.

- The first detailed investigation of the radiative properties of SIMOX has been performed.
- The first detailed experimental measurements of the radiative properties of Si_3N_4 have been performed. The real part of the dielectric constant or refractive index has been deconvoluted from the measured properties in the near-mid IR.
- A thorough testing of the models and simulation tools available to the industry has been made. The models have been utilized extensively in investigating the optical properties, and the effects of surface morphology. The models utilized in performing the simulations of the optical properties of ideally double-side polishes wafers agree in their basic mathematical approaches, i.e. the Abele's matrix theory and differ in the degree of complexity and number of parameters involved. The models utilized to achieve the surface effects task fall under two categories: simple approach that utilizes an extension of the equations that treat the parallel plane properties by relating the roughness effect linearly with the ideally polished plane surfaces, and the other proposed by NREL that utilizes a complex solid-state approach for the optical parameters and a statistical (e.g. Monte-Carlo) technique that tends to average the behavior of a photon incident on the textured surface over all the possible angles and wavelengths.

- Various approaches using wafer emissivity independent tools for non-contact temperature measurements are discussed with emphasis on the advantages and limitations of the technique.

EMISSIVITY MEASUREMENTS AND MODELING OF SILICON RELATED MATERIALS AND STRUCTURES

by
Sufian Abedrabbo

A Dissertation
Submitted to the Faculty of
New Jersey Institute of Technology and Rutgers the State University of New Jersey
in Partial Fulfillment of the Requirements for the Degree of
Doctor of Philosophy

Department of Physics

August 1998

APPROVAL PAGE

EMISSIVITY MEASUREMENTS AND MODELING OF SILICON RELATED MATERIALS AND STRUCTURES

Sufian Abedrabbo

Dr. Nuggehalli M. Ravindra, Dissertation Advisor — Date
Professor of Physics, NJIT

Dr. John C. Hensel, Dissertation Committee Member — Date
Distinguished Research Professor of Physics, NJIT

Dr. Anthony T. Fiory, Committee Member — Date
Member of Technical Staff, Bell Laboratories, Murray Hill, NJ

Dr. Bhushan L. Sopori, Committee Member — Date
Senior Project Leader, National Renewable Energy Lab, Golden, CO

Dr. Earl D. Shaw, Committee Member — Date
Professor, Chairman of Physics Department, Rutgers, Newark, NJ

Dr. John F. Federici, Committee Member — Date
Associate Professor of Physics, NJIT

BIOGRAPHICAL SKETCH

Author: Sufian Abedrabbo

Degree: Doctor of Philosophy

Date: August 1998

Undergraduate and Graduate Education:

- Doctor of Philosophy in Applied Physics,
  New Jersey Institute of Technology and Rutgers the State University of New Jersey, Newark, NJ, August 1998

- Master of Science in Applied Physics,
  New Jersey Institute of Technology and Rutgers the State University of New Jersey, Newark, NJ, October 1997

- Bachelor of Art and Science in Applied Physics,
  Rutgers the State Unioversity of New Jersey and New Jersey Institute of Technology, Newark, NJ, May 1993

Major: Applied Physics

Presentations and Publications:

[1] S. Abedrabbo, J.C. Hensel, A.T. Fiory, B. Sopori, W. Chen and N.M. Ravindra, "Perspectives on Emissivity Measurements and Modeling in Silicon", *Materials Science in Semiconductor Processing*, 1998 (In Press).

[2] S. Abedrabbo, F.M. Tong, O.H. Gokce and N.M. Ravindra, J. Gelpey and S. Marcus and A.T. Fiory", Wafer Emissivity Independent Temperature Measurements", *Journal of Electronic Materials*, Oct. 1998 (In press).

[3] N.M. Ravindra, S. Abedrabbo, O.H. Gokce, F.M. Tong, A. Patel, V. Rajasekhar, G. Williamson and W. Maszara, "Radiative Properties of SIMOX", *IEEE Transactions on Components, Packaging, and Manufacturing Technology*, Sept. 1998 (In press).

To my beloved family

ACKNOWLEDGMENT

The author wishes to express his sincere gratitude to Dr. N.M. Ravindra for his valuable guidance, inspiration and encouragement during the entire course of this research. The author is very thankful to Dr. J.C. Hensel of NJIT, Dr. A.T. Fiory of Lucent Technologies, Dr. B. Sopori of NREL, Dr. E. Shaw of Rutgers and Dr. J. Federici of NJIT for serving as members in my dissertation committee with special thanks to Drs. Hensel, Fiory and Sopori for their invaluable scientific support and contribution.

The interaction with M. Oh, B. Nguyenphu of Lucent Technologies, T. Rieley of AMD, A. Nanda of SEMATECH/Lucent Technologies, C. Schietinger of LUXTRON, D. Lindholm of SEMATECH, M. Yam of Applied Materials, J. Gelpey and S. Marcus of Steag-AST and J. Zobel of Burleigh Instruments is acknowledged.

The author is very thankful to the New Jersey Commission, SEMATECH, DARPA, and the NJIT Physics Department for the financial support through out this study.

The author is greatly indebted to his mother, father , brothers, uncle Abu Musa and especially my dear brother Ghassan for moral support and encouragement. The author would especially like to acknowledge the moral and scientific support of Dr. O.L. Russo of NJIT. The author would like to acknowledge the support of Dr. D. Murnick of Rutgers, Dr. F. Roozeboom of Philips, Dr. A. Johnson of NJIT, Mr. S. Bharati of Intel and Dr. J. Krishnaswami of Plainsboro, NJ. The author is also thankful to Prof. F.M. Tong and colleague W. Chen for their scientific contribution. He expresses thanks to his colleagues in the group - Dr. O.H. Gokce, V. Rajasekhar A. Patel and D. Pattnaik for all

their support. The author is deeply thankful to Dr. R. Kane, Dean of the graduate school and Dr. J. Jaber, Director of the international student office for their advise and moral support throughout the course of his study.

TABLE OF CONTENTS

TABLE OF CONTENTS
(Continued)

TABLE OF CONTENTS
(Continued)

TABLE OF CONTENTS
(Continued)

LIST OF TABLES

LIST OF FIGURES

LIST OF FIGURES
(Continued)

LIST OF FIGURES
(Continued)

LIST OF FIGURES
(Continued)

LIST OF FIGURES
(Continued)

LIST OF FIGURES
(Continued)

CHAPTER 1

INTRODUCTION

In semiconductor manufacturing temperature dependent processes are abundant. In many of these processes, the precise temperature of the wafer surface is the most important parameter [1]. This is important, in particular, in deposition and growth processes such as i) chemical vapor deposition (CVD) [2], ii) batch mode horizontal and fast ramp vertical furnaces [3], iii) chemical mechanical polishing (CMP), iv) photoresist deposition and baking [4], v) molecular beam epitaxy (MBE) and especially in vi) rapid thermal processing (RTP) [5]. Any change in the wafer's temperature means a change in the annealing temperature or thickness and/or uniformity of the grown or deposited film. Thus, a very stringent control over the temperature of the wafer both in equilibrium and non-equilibrium situations is a must. To control the temperature of a wafer in any process, many monitoring techniques are being utilized. The major two monitoring techniques, however, are thermocouples and pyrometers.

The objective of this research is to study in depth the radiative properties of silicon and silicon related materials and structures for temperature determination via pyrometry, in particular, for RTP applications. In this work, some of the most challenging issues that face the industry and prevent accurate measurements of temperature are analyzed, tackled and modeled. To achieve this objective, a novel spectral emissometer has been utilized extensively to yield the emissivity, reflectivity and transmissivity as function of wavelength and temperature range of 1-20μm and 300-1200K, respectively. The spectral emissometer

has been utilized extensively to measure (a) single-versus double-side polished silicon wafers, (b) front- versus back- side of single-side polished silicon wafers, (c) Doping, (d) Si_3N_4, (e) SiO_2/Si, with various oxide thickness, (f) multi-layers of $SiO_2/Si/SiO_2$ and (g)$SiO_2/Si/SiO_2$/polysilicon, with a, b and c being the major issues under focus.

In Chapter 2, the background of RTP and its importance for the cluster tool era is discussed in detailed. Temperature sensors in RTP and other semiconductor processes are the focus of Chapter 3. Spectral emissometry is established as the tool for emissivity and measurement of other optical properties in chapter 4. In the following two chapters the optical properties of silicon and silicon related structures are summarized with emphasis on surface roughness and doping-type as the main problems facing the emissivity at temperatures below the opacity of silicon and for energies in sub-bandgap region of < 1.12 eV. Chapter 7 surveys the models available in the literature and the mathematical approaches utilized by these models. Chapter 8 is dedicated to wafer emissivity independent approaches that lead to a basis for possible solution to the temperature measurement problem. Remarks on the current experimental approach is the subject of chapter 9. Conclusions and recommendations based on these studies are presented in the last chapter.

CHAPTER 2

BACKGROUND

2.1 Rapid Thermal Processing

2.1.1 Why RTP

On the verge of the twenty first century, the demand for larger wafers and scaling of device dimensions seem to be more stringent than ever. The scale of integration of dynamic random-access memory (DRAM) chips, for example, has continued to increase by four times every three years [6]. As a matter of fact, in 1997 the standard MOS active region in metal-oxide-semiconductor (MOS) reached 250nm [5]. Table 2.1 [5], shows clearly the strong decrease in device size with time. This coupled with the need to minimize (a) the temperature-time product or the thermal budget, (b) the process-induced contamination, (c) device failure, (d) thinner gate oxides (e) shallower source/drain junctions and most importantly strong drive for the (f) 300mm diameter silicon wafer [7-12] has led to single-wafer processing techniques such as RTP.

Table 2.1 1997 National Technology Roadmap for Semiconductors (NTRS) [5]

	1997	**1999**	**2001**	**2003**	**2006**	**2009**	**2012**
Technology in production (nm)	250	180	150	130	100	70	50
Equivalent T_{ox} of production technology (nm)	4-5	3-4	2-3	2-3	1.5-2	<1.5	<1.0
T_{ox} thickness (% 3 sigma)	±4	±4	±4	±4-6	±4-8	±4-8	±4-8
X_j at channel (nm)	50-100	40-80	35-65	26-52	20-40	15-30	10-20

RTP is a key technology in the cluster tool, single wafer manufacturing approach. In RTP, a single wafer is heated quickly with ramp rates from 25 to 400°C/sec, at atmospheric or low pressure maintaining uniform temperature across the wafer. RTP offers "the potential to significantly reduce thermal budget, while affording single-wafer granularity and cluster compatibility" [13]. As a matter of fact, when 1 Gbit DRAM with 0.18μm design rule are projected on 300mm diameter wafers, many process steps will have narrow process windows in batch furnaces such as shallower ion implantation junctions and thinner gate oxides. For these process steps, RTP provides the better alternative, if not the only one. This is because of the much shorter time needed in RTP (seconds to minutes) both in ramping up and in the steady state or the entire process itself when compared to the batch mode furnaces (ramp up 25-30 minutes, steady state 30-60 minutes and ramp down 30 minutes). Moreover, cycle time and yield/cost considerations will drive more process applications toward RTP [14].

2.1.2 Applications of RTP

In RTP, the process chamber is made of either quartz, silicon carbide, stainless steel, or aluminum with quartz windows. The wafer holder is often made of quartz and the physical contact with the wafer is in minimum number of places. A temperature measurement system is placed in a control loop to set wafer temperature. The RTP system is interfaced with a gas handling system and a computer that controls system operation. Small thermal mass and stringent ambient and particle control enables RTP to reduce processing times and improve process control in the formation of pn junctions, thin oxides, nitrides and

silicides, thin deposited layers, and flowed glass structures [6]. In addition to this, there are various processes that can be performed with RTP as summarized in table 2.2 [15]:

Table 2.2 Some semiconductor device applications of RTP [15]

APPLICATION	DESIRED PROCESS	UNDESIRED PROCESS
Shallow N+ Doping	Extended defect removal	As Diffusion
Shallow P+ Doping	Conductivity/ Activation	Boron Diffusion, Normal + Enhanced
WSi_2 Annealing	High Conductivity	Boron Diffusion
Si-Ge Superlattice	Abrupt Thin Layers	Graded Interfaces
Self Aligned $CoSi_2$	Nucleation, Smooth Surface	Grain Growth, Rough Surface
Al-Si Contacts	Form Ohmic Contact	Al Spiking
Trench Capacitor	Grow and Flow Oxide	Breakdown Due to Strain, Thinning
Self Aligned MISFET	Activate Source/ Drain	Contact Alloying, AlGaAs Evaporation
High Mobility III-V Heterostructure	Active Si Donors	Diffusion of Si
RTCVD	Metal and Dielectric Deposition	Temperature Non-uniformity

2.2 NJIT RTP Systems

At NJIT, there are two RTP systems [15]. One of the systems is manufactured by Process Products/CVC. It is comprised of linearly arranged tungsten-halogen lamps, and is similar to those used in mass production in the industry. The other RTP system, the Advanced Vacuum Processor (AVP), is a state-of-the-art system designed by Texas Instruments. It features three concentric rings of tungsten halogen lamps: 24, 1-KW lamps in the

outermost ring, 12, 1-KW lamps in the middle ring, and a 1, 2-KW lamp in the center. The configuration of the lamp in the AVP chamber is shown in Fig.1. The lamps are isolated from the process chamber by a quartz window as shown in Fig.2. This system is fully vacuum compatible and can handle two gases, such as N_2 and O_2. It can attain temperature up to 1000°C and is provided with two real-time temperature sensors- a chalcogenide fiber bundle sensor for monitoring the reflected component of the radiation and a fluoride fiber bundle sensor for monitoring the temperature of the quartz window. The TI-RTP system is also equipped with a PC-based thermocouple data acquisition system for monitoring temperature by using silicon wafers instrumented with thermocouples. Fig.3 shows a detailed schematic for the temperature data acquisition using the TI-RTP system.

2.3 Challenges to RTP

Temperature measurement and control is a fundamental challenge in RTP. This is because of the non-equilibrium nature of the process and the time constants associated with the silicon wafer, the chamber walls and the sensors. It is said that RTP still has inadequate temperature measurement and control capability for applications more critical than current silicides [13]. Poor RTP reactor designs can indeed lead to significant temperature differences across the wafer, thus causing stress. Moreover, for silicon device processing, the control of temperature in the RTP system, of ±2°C, (table 2.1,) is critical because of the need to [15]:

- minimize dopant redistribution,
- improve electrical characteristics of devices,

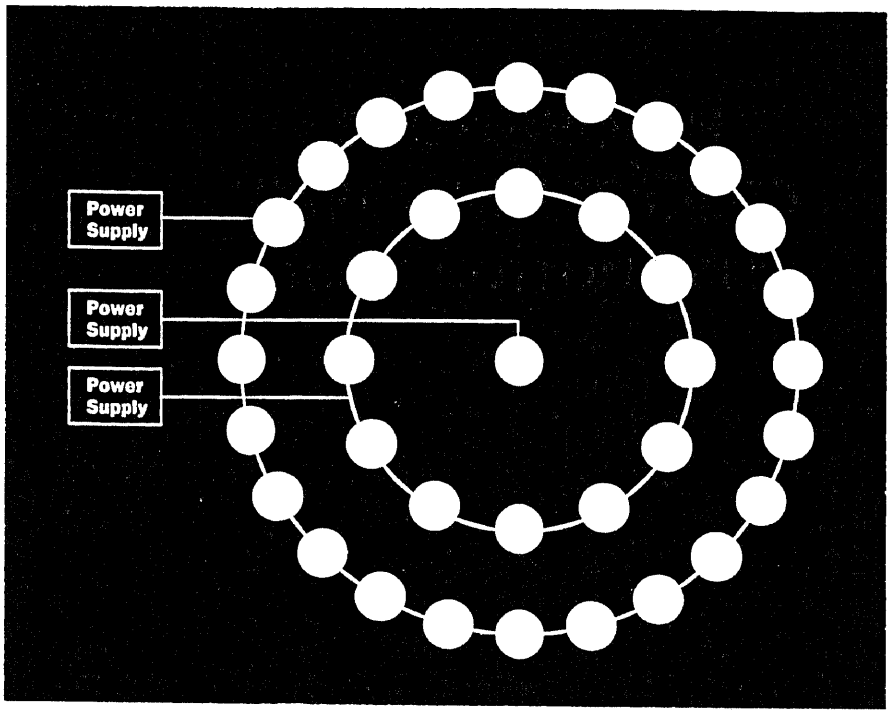

Fig.1 A configuration of the tungsten-halogen lamps in the TI-RTP system

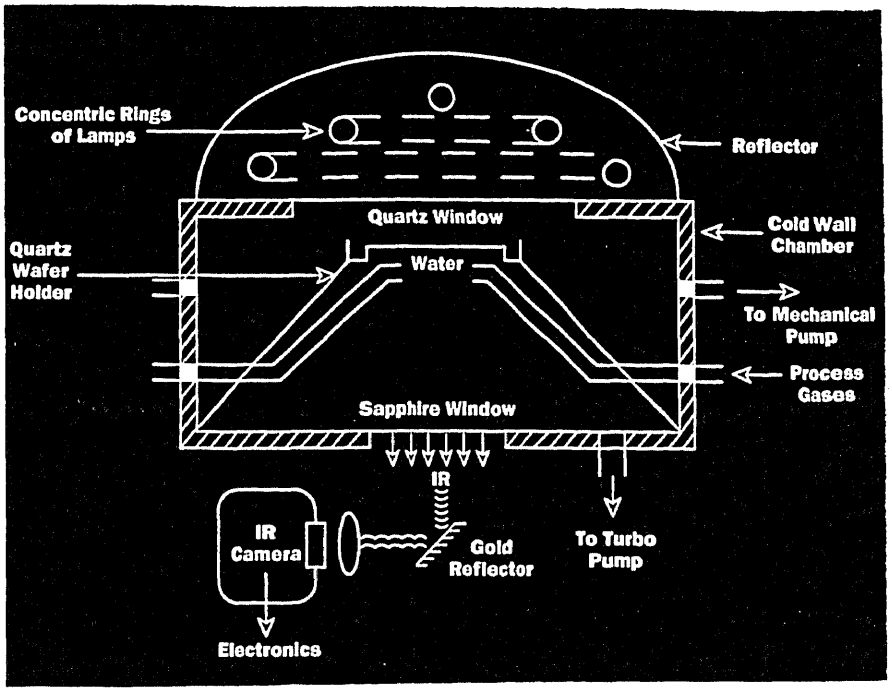

Fig.2 A schematic of the TI-RTP system

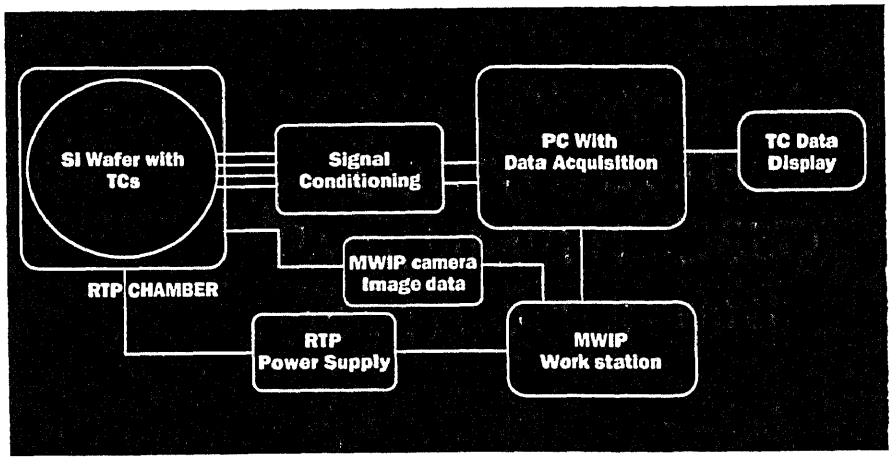

Fig.3 A schematic of temperature data acquisition using RTP

- minimize slip dislocation lines,
- improve electrical characteristics of devices,
- minimize gate oxide thickness non-uniformity,
- improve yield.

CHAPTER 3

TEMPERATURE MEASUREMENT TECHNIQUES IN RTP

In RTP the chamber walls and the wafer are not in thermal equilibrium. This is due to the very nature of the short duration of the process. Thus it is very important to know the exact temperature of the wafer surface. The fact that non-uniformity of wafer temperature at different points on the wafer surface exists forces us to determine the spatial distribution of temperature across the wafer surface. This complicates the monitoring process even further.

The most widely used techniques to measure temperature in RTP are optical pyrometry and thermocouple embedded wafers. This chapter will present an overview of these two techniques and their limitations. Following that light will be shed on some of the techniques studied and considered as possible alternatives for temperature measurements in RTP. The final section will introduce the optical properties, reflectivity, transmissivity and emissivity.

3.1 Contact Sensors

3.1.1 Thermocouples

Thermocouples: They are defined as a junction of two dissimilar materials that, upon heating, will produce a voltage across the two open leads. This effect is referred to as thermovoltaic effect. The junction is referred to as a thermocouple and it is the responsive element in this temperature measurement technique. When two or more of these junctions

are combined together in a single responsive element, it is defined as a thermopile. The signal produced by the thermocouple is translated into temperature. Thermocouples are affected by both the radiative portion of heat irradiated from the wafer surface and by the conductive element of heat by means of contact, with the last being the major factor. Thus, for a thermocouple to determine the exact temperature of a wafer, it has to be in contact with the surface of the wafer. Furthermore, it is now known that for most accurate temperature measurement, the thermocouple is to be embedded inside the wafer, i.e. the backside of the wafer is physically drilled and a much longer wire than the hole diameter is embedded in a zigzag shape to obtain the maximum signal. It is worthwhile to note some of the following features of thermocouples [16]:

(a) Thermocouples measure both the temperature of the wafer (via Peltier effect) and the temperature gradient of the wire (Thomson effect).

(b) Thermocouples measure an approximate temperature of the wafer [17].

(c) As has been pointed out before, the electrical signal is translated into temperature by many methods. One common conversion is to use of standard reference table such as the International Temperature Standard ITS-90 and then interpolating from a number of ITS-90 fixed points [18,19].

Despite its limitations, the thermocouple is still the best contact method of determining temperature of an object and is used for calibration purposes in RTP. Furthermore, for annealing applications thermocouples are used as the technique for temperature measurements. One such RTP system is the 1987 NJIT CVC/Process Products RTP.

3.1.2 Problems with Thermocouples

For a thermocouple to operate, it has to be in physical contact or be embedded in the object under investigation. This has not prevented it from being the standard technique for measuring temperature in both horizontal and vertical batch-mode reactor furnaces. This is simply because the wafer is in complete equilibrium with its surroundings, and hence determining the furnace temperature decides the wafer temperature. Thus in furnaces, the thermocouple will be embedded or in contact with the furnace and the temperature reading of the furnace will be equal to that of the wafer because of the long duration of such a process. On the other hand, this is not the case in the RTP chamber, where the wafer is not in equilibrium with its surroundings. This means that for the thermocouple to determine the temperature of the surface of the wafer in RTP, it has to be embedded in the wafer which means that at elevated temperatures the wafer is exposed to contamination. Thermocouple embedded wafers cannot be used for real-time temperature monitoring in rapid thermal deposition or growth processes, such as RTCVD and RTO, respectively. In addition, during the operation of some RTP systems e.g. Applied Materials Centura the wafer is under constant rotation in order to distribute the radiated energy uniformly over the wafer. Thus, definitely a thermocouple embedded wafer cannot be the choice for temperature measurement in this case. Finally, the temperature non-uniformity across the surface of a large diameter wafer is a critical issue in silicon process monitoring. This requires that sensors be distributed on several locations across the wafer surface.

3.2 Non-Contact Sensors

3.2.1 Pyrometers

Pyrometry is an optical technique that determines the surface temperature of the sample by detecting its radiated flux. Pyrometers consist of responsive elements for IR detection, software and hardware coupled with them as part of the control system to determine the temperature of the object under investigation. The responsive element in a pyrometer can be one of the following [20]:

(a) Bolometers: Incident IR photons cause an increase in the bolometer temperature. Since the bolometer resistance versus temperature curve has a non-zero slope, a change in temperature leads to a change in the bolometer resistance.

(b) Photoconductive detector: A change in the incident photon flux on the semiconductor surface causes a change in the generated free-carriers, thus, causing a change in the electrical conductivity.

(c) Photoelectromagnetic detector: IR photons absorbed by the detector generate free-carriers which diffuse in the bulk and are separated by a magnetic field. The charge separation causes an electric signal that is proportional to the number of photons.

(d) Photovoltaic detector: changes in the number of incident photons cause a change in the voltage generated by the junction.

(e) pyroelectric detector: IR photons change the temperature of the crystalline responsive element. This alters the dipole moment which produces an external electric field.

There are other types of responsive elements that can be utilized in pyrometers but they are out of the scope of this work.

In all of the responsive elements cited above, the change in the number of incident photons, which is a function of the radiating source, causes a change in the electrical signal. Upon monitoring the electrical signal that results in voltage or conductivity change in a coupled electronic circuit and analyzing the resulting I-V curves from the pyrometer the accurate IR intensity is determined. The object temperature is determined by relating the IR intensity to the known Planck function. As a common practice, the manufacturers of RTP systems as well as the users determine the control recipes after calibrating the pyrometer with multi-point thermocouples embedded into a control wafer to attain maximum accuracy, repeatability and reproducibility. Thus, for an ultra-clean environment and a tight control over contamination in processes like RTP, pyrometers will be the choice for temperature measurements and control. Furthermore, it is possible to increase the area of detection (limited by the detector solid angle) by utilizing many pyrometers over several positions of the chamber to achieve the best process uniformity and control. The RTP system "Centura" made by Applied Materials, utilizes more than 7 pyrometers.

3.2.2 Limitations of Pyrometers

Pyrometers are limited by their operating wavelengths which can limit sensitivity to samples depending on the radiation at that particular wavelength as function of temperature. Pyrometers are also limited by their spatial resolution, which is a direct function of the exitance detector solid angle [21]. Other problems can arise from the lack of knowledge of the emissivity data of particular samples due to changes in morphology [22] or extrinsically deposited or grown structures [23]. In RTP, pyrometers are situated

at the lower wall of the chamber and sometimes at the back of a shield located below the wafer to eliminate stray lamp radiation as in the AG Associates design [23]. To achieve maximum performance of a pyrometer, an accurate and precise pre-knowledge of the emissivity model of the wafer under consideration is a necessity.

Thermal radiance of an object is characterized by Planck's blackbody spectral radiance $M_{\lambda,b}(T,\lambda)$, the wafer emissivity $\varepsilon(\lambda,T)$, and is given by [24]

$$P_\rho = Af(h)\varepsilon(\lambda,T)M_{\lambda,b}(T,\lambda), \qquad (3.1)$$

where T is the wafer temperature, λ is the pyrometer operating wavelength(s), A is the area of the wafer that contributes directly to the pyrometer signal, and f(h) is a function dependent on the distance h between the wafer and the pyrometer. In order to determine the accurate temperature of the wafer according to the requirements of the industry, i.e. $\pm 3°C$, emissivity is the term that will stand out as the most important factor that has to be determined precisely.

3.3 Other Temperature Measurement Techniques

3.3.1 Raman Scattering

The Raman effect is a well studied phenomena in physics. Inelastic scattering of a photon by a crystal involves absorption or emission of a phonon. The two processes result in two sharp peaks on an intensity plot [25]. One peak is called Stokes line and has the frequency of $(\omega-\Omega)$, where ω is the incident photon frequency and Ω is the frequency of the created phonon. The other is called anti-Stokes line and has the frequency $(\omega+\Omega)$, where Ω is the frequency of the absorbed phonon. Since initially the phonon population is in thermal

equilibrium, the ratio of intensities is given by a Boltzmann factor,

$$I(\omega-\Omega)/I(\omega-\Omega) = \exp(-h\Omega/2\pi kT) \qquad (3.2)$$

where k is the Boltzmann constant, and T is the absolute temperature.

Limitations: One of the major problems in using this technique is the long time response of 1-10 seconds, which is inadequate for RTP applications. Another limitation to this technique is its high cost of $50-70K.

3.3.2 Laser Interferometric Thermometry

In this technique, the temperature of the wafer is determined utilizing its direct relation to slight changes in the refractive index of the semiconductor [26]. As the optical path length difference resulting from the two components of a monochromatic light refracted by a polished wafer is known, the refractive index is determined according to the following relation:

$$\Delta L = 2nh \cos\theta' = 2nh\,[1-(\sin(\theta)/n)^2]^{1/2} \qquad (3.3)$$

where n and h are the refractive index and thickness of the plate, respectively, θ' and θ are inner and outer angle of incidence, respectively. Then using typical interferogram data as a function of wavenumbers or wavelengths the temperature is determined by observing a number of fringes in the interferogram. Limitations: Since there is no reliable data for the refractive index at temperatures above the opacity of the wafer, it is very hard to determine the exact temperature of the wafer depending on the refractive index. Another problem is that as the temperature is increased, the absorption of the sample is enhanced which makes it difficult to have any photon interferogram transmitted through the sample.

Some of the other temperature measurement techniques under investigation are: Photoacoustic Thermometry, Optical Fiber Thermometry, Dual Wavelength Pyrometry and Ellipsometric Pyrometry. These techniques as well as the currently used techniques are summarized in table 3.1 [25]

Table 3.1 Summary of thermometry techniques [25]

Name	Mfg. cost ($)	Remote Sensing	Precision (°C)	Range (°K)	Response Time (s)
Optical Pyrometry	$2K	Easily implemented	10-50C	500-1600K	300ms-10s
Raman Scattering	$50-70K	Almost impossible	50C	77-1500K	1-10s
IR Laser Interferogram	$3.8K	Very Flexible	3C	300-900K	>300ms
Optical diffraction thermometry	$30-50K	Up to 40 cm	2C	290-1000K	1 sec
Photo-acoustic thermometry	not known	not known	1C in principle	not known	not known
Optical fiber thermometry	$13-30K	Fiber optics	0.05%	500-1900C	20-1000ms
Dual wavelength pyrometry	$3.875K	Fiber optics	0.8C	700-1100K	200ms
Ellipsometric pyrometry	$15-30K	Similar to pyrometry	1C	500-2500K	10ms

Only the dual wavelength pyrometry and the optical fiber thermometry are in use in RTP systems today along with the optical pyrometry and thermocouples. The first three methods depend heavily on the emissivity of the wafer which is the subject of the next section.

3.4 Emissivity and Other Optical Properties

Emissivity is defined as the ratio of the radiation emitted by a wafer with temperature T, at a given wavelength λ, angle of incidence θ, and plane of polarization φ, to that emitted from a blackbody under the same conditions [27]. It is a function of the azimuthal angle if the surface does not have azimuthal symmetry. Since this definition is for narrow spectral intervals, it refers to spectral emissivity [20]. As observed, spectral emissivity is a complicated function of the (a) intrinsic emissivity of the substrate, (b) extrinsic emissivity of the layers or thin films on top of substrate, and (c) optical properties of the reflective chamber walls and lamps radiation that might transmit through the wafer and get detected by the pyrometer. A combination of all these is defined as the effective emissivity. To be able to calibrate for the effective emissivity, it is essential to measure and model both the intrinsic and the extrinsic emissivity separately and accurately.

3.4.1 Intrinsic Emissivity

In the course of this study, this term - "intrinsic emissivity" will be referring to the emissivity of the silicon substrate unless specified otherwise. The first detailed study performed on silicon specimen has been performed by Sato as shown in Fig.4 [28]. For normal incidence, the emissivity ε of a plane parallel specimen is given by (see pg.127):

$$\varepsilon(\lambda) = [1-\rho]\,[1-\tau] / [1-\rho\tau] \qquad (3.4)$$

where ρ is the true reflectivity, i.e. the reflective component of light from the front side of the wafer only, and τ is the true transmissivity, i.e. internal transmissivity before passing through the backside of the wafer, both of which are functions of wavelength λ.

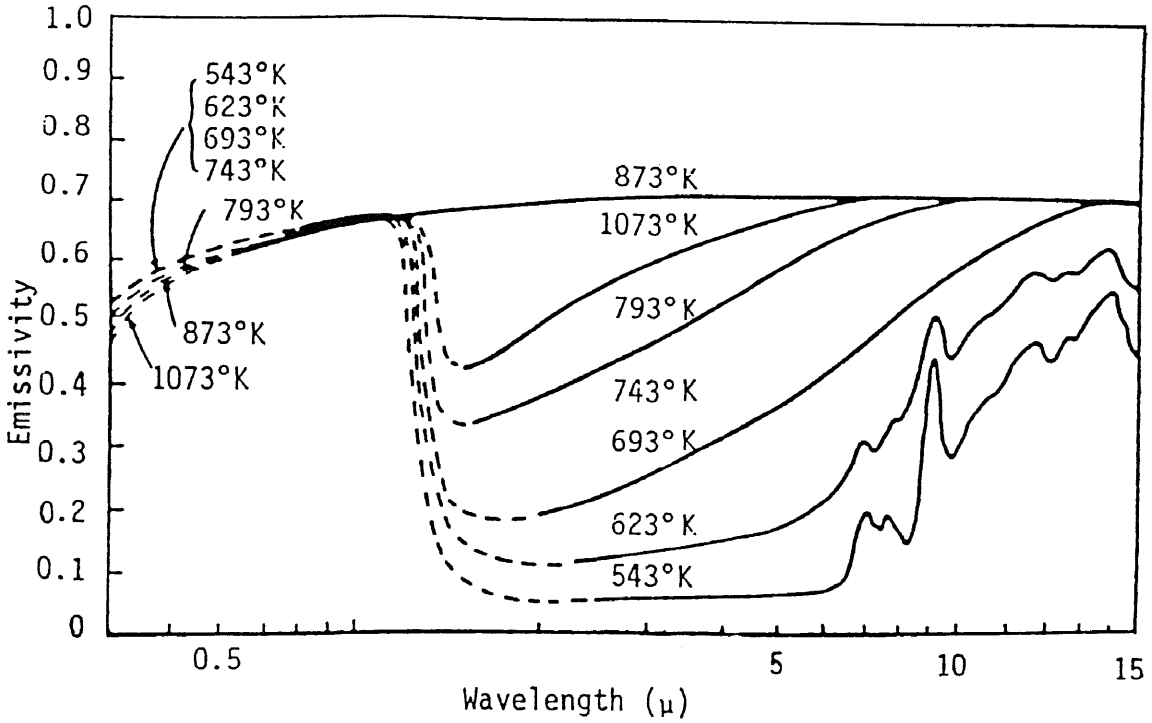

Fig.4 Spectral emissivity of a single-crystal n-type double-side polish silicon disc, 1.77 mm thick, $\rho = 15\Omega.cm$, as function of wavelength and temperature [28]

τ is also referred to as the attenuation factor. ρ and τ are related to fundamental optical constants -- n, the refractive index and k, the extinction coefficient for a normal incident light by the following relations:

$$\rho(\lambda) = [(n-1)^2 + k^2] / [(n+1)^2 + k^2] \tag{3.5}$$

$$\tau(\lambda) = \exp[-\alpha t] = \exp[-4\pi k t / \lambda] \tag{3.6}$$

where $\alpha(\lambda)$ is the absorption coefficient and t is the thickness of the specimen. Thus, from equation (3.4), for a perfect opaque body, since $\tau = 0$, emissivity follows as:

$$\varepsilon(\lambda) = [1-\rho] \tag{3.7}$$

The experimentally measured values of transmissivity, and reflectivity include extra effects like multiple internal reflection depending on the angle of incidence, surface roughness and interface roughness, etc. These values are called apparent transmissivity, $\tau(\lambda)^*$, and apparent reflectivity, $\rho(\lambda)^*$, respectively, as referred to by Sato [28] and reflectance and transmittance, respectively, as referred to in the Handbook of Optics [29,30]. They are related to the true values, only for a double side polished specimen, by the following mathematical relations [28,31] (Fig.5):

$$\tau(\lambda)^* = \tau(\lambda) \frac{(1 - \rho(\lambda))^2}{(1 - \rho(\lambda)^2 \tau(\lambda)^2)} \tag{3.8}$$

$$\rho(\lambda)^* = \rho(\lambda)\left\{1 + \frac{\tau(\lambda)^2 (1 - \rho(\lambda))^2}{1 - \rho(\lambda)^2 \tau(\lambda)^2}\right\} \tag{3.9}$$

The following relation holds:

$$\rho^* + \tau^* + \varepsilon = 1 \tag{3.10}$$

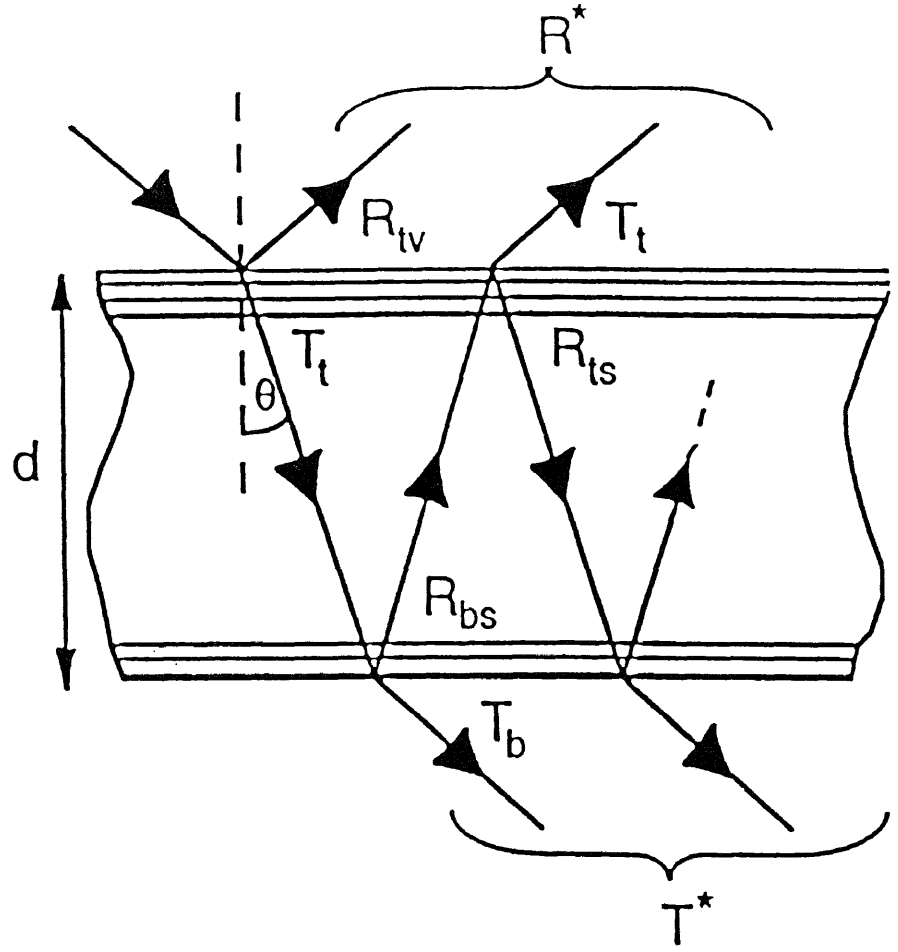

Fig.5 The effect of multiple internal reflections on the apparent reflectivity and transmissivity of a double-side polished specimen which has coatings on both surfaces [31]

Kirchhoff's law states that the emissivity for a Lambertian (diffuse) radiator that is in thermodynamic equilibrium with its surroundings is equal to its absorptivity a:

$$\varepsilon(\lambda,T) = a(\lambda,T) \tag{3.11}$$

Absorptivity of the silicon substrate depends on several factors:

(a) Surface roughness: rough surfaces increase light trapping resulting in increased emissivity.

(b) Surface temperature and wavelength of the absorbed and emitted radiation as is shown in Fig.4.

(c) Number of free carriers which is a function of doping and temperature.

In the chapter on modeling the absorptivity of silicon will be treated from first principles in optics and in more detail.

3.4.2 Extrinsic Emissivity

The emissivity of the wafer will be effectively changed upon adding a new layer of dielectric or metal or another semiconductor [32,33]. Hence in-situ emissivity compensation is needed in this case.

3.4.3 Effective Emissivity

An experiment performed by Pettibone et al. [34], is presented here to show the importance of additional factors on the emissivity detected from a wafer in a chamber. Pettibone et al. have measured the reflectance of a silicon wafer during the growth of a thermal oxide of 0.4μm in a chamber with highly reflective walls for temperatures

>600°C. Using (3.7) to determine the emissivity ($\rho(\lambda) \sim \rho(\lambda)^*$ for T>600°C), they noticed that the emissivity increased from 0.71 to 0.87. Theoretically in a chamber such as theirs a change in emissivity would represent a temperature difference of more than 100°C. Surprisingly, the actual difference in temperature was in the range of 10-50°C. The discrepancy is attributed to the highly reflecting walls of the chamber which enhance the effective emissivity of the wafer. Another study by Nulman et al. [35] has reported that decreasing the chamber walls reflectance by using pyrometers operating at wavelength (λ = 4.5μm) at which the inner quartz chamber becomes opaque, i.e. the quartz and not the gold represents the walls of the chamber, causes the emissivity changes due to the growth of oxide layer to be larger.

The above studies lead to the conclusion that the control of temperature in RTP requires accurate calculations and models of the RTP chamber components and their influence on emissivity.

CHAPTER 4

PROPOSED APPROACH

4.1 Spectral Emissometer

The schematic of the spectral emissometer is presented in Fig.6. It consists of a hemi-ellipsoidal mirror providing two foci, one for the exciting source in the form of a diffuse radiating near-blackbody source and the other for the sample under investigation. A microprocessor controlled motorized chopper facilitates in simultaneous measurement of sample spectral properties such as reflectivity, transmissivity and emissivity. A carefully adjusted set of five mirrors provide the optical path for measurement of the optical properties. The source of heating of the samples is provided by an oxy-acetylene/propane torch. However, because of safety considerations and potential sample contamination, various alternatives to heat the samples, uniformly in a controlled environment, are being investigated.

The spectral emissometer consists of three GaAs lasers to facilitate in aligning the sample at the appropriate focus. A high resolution Bomem FTIR, consisting of Ge and HgCdTe detectors, interfaced with a Pentium processor, permits data acquisition of the measured optical properties. Further, this on-line computer enables the user to flip the mirrors to acquire transmission/reflection spectra via software configurations such as Spectra Calc and GRAMS. The system, acquired by NJIT from On-Line Technologies through a research grant from the Defense Advanced Research Projects Agency (DARPA), is the third of its kind in the United States.

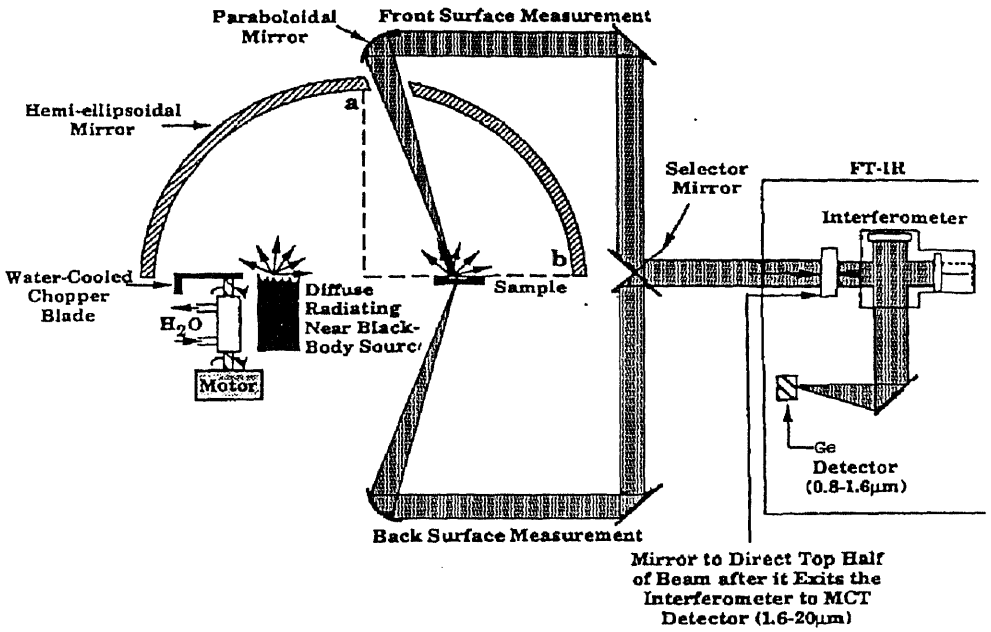

Fig.6 Schematic of bench top emissometer showing components and optical paths for radiance, reflectance, and transmittance

4.2 Temperature Measurement

The spectral emissometer allows for simultaneous measurements of radiance, reflectance, transmittance and the temperature of the sample at the measured point. The theoretical background and methodology is as follows [36]. A sample is placed at one of the foci of the hemispherical ellipsoidal mirror while the source, a blackbody at 900°C, is at the other foci. The chopper (in Fig. 6) permits the simultaneous acquisition of the radiative properties of interest including the sample temperature. A front-surface sample measurement, with the chopper closed, yields the sample's directional spectral radiance:

$$M_o(\text{closed}) = BR_\nu(T) = B\varepsilon_\nu(T)\, R_\nu^b(T) \qquad (4.1)$$

where in $B = Ad\nu d\Omega\cos\theta$ we lump together various factors fixed by the experimental situation; $d\nu$ is the frequency interval, $d\Omega$ is the solid angle, and A is the sample area at angle θ with respect to a given direction. $\varepsilon_\nu(T)$ is the emissivity of the sample at temperature T, and R_ν^b is the blackbody radiance at temperature T of the sample. Radiance $R^b{}_\nu(T)$ is defined as the rate that energy is radiated at frequency n from a blackbody at temperature T per unit frequency per unit solid angle per unit normal area.

When the chopper is open, the measured radiation M_0 will include that emitted by the sample and the blackbody source radiation reflected by the sample in spectral directional-hemispherical mode,

$$M_o(\text{open}) = BR_\nu(T) + B\rho_\nu(T)\, R_\nu^b(T_{bb}) \qquad (4.2)$$

where T_{bb} is the constant blackbody source temperature, which is maintained at 900°C, and ρ_ν is the apparent reflectivity. The difference in the two measurements is thus $\rho_\nu(T)$ $R_\nu^b(T_{bb})$. The constant source radiation $R_\nu^b(T_{bb})$ is quantified by replacing the sample assumed to be perfect reflector (a gold mirror, $\rho_\nu^{gold} = 1.0$) and measuring the spectrum in the chopper open condition. Thus, the apparent reflectivity of the sample, $\rho_\nu(T)$, can be determined.

For an opaque sample, the spectral emittance, $\varepsilon_\nu = 1 - \rho_\nu$. For non-opaque samples, the apparent transmissivity, τ_ν, is measured by flipping the selector mirror and measuring the back surface radiance and back surface radiance plus transmittance. The source radiation is quantified with the sample absent, and the analysis to determine τ_ν follows that for ρ_ν. The full closure relationship, $\varepsilon_\nu = 1 - \rho_\nu - \tau_\nu$, is then used to determine ε_ν. By re-

arrangement of equation (4.1), $R_\nu^b(T) = R_\nu(T) / \varepsilon_\nu(T)$, the surface temperature of the sample can be determined by two methods: one is direct integration over the whole spectral region,

$$\int R_\nu^b(T)\, d\nu = \sigma T^4 \qquad (4.3)$$

The Stefan Boltzmann constant $\sigma = 5.67\times10^{-12}$ W·cm^{-2} K^{-4}. The sample temperature can be obtained to within ±10°C. The other method is to fit the calculated experimental radiance of the sample with that of the theoretical Planck function calculations of temperature under the same experimental conditions and range of wavelengths. This method is the one utilized by the software (Array basic) acquired from Advanced Fuel Research. Fig.7 shows the method utilized in determining the temperature for a hot surface of graphite (G-96). This temperature determining methodology utilizing the spectral emissometer has been verified by a thermocouple embedded wafer supplied by CGS. The wafer was heated up to 300°C. The thermocouple data agreed with the fitted data to within 20°C.

4.3 Reciprocity Principle

The design and operation of the spectral emissometer is based on the Helmholtz's principle of reciprocity. This principle allows one to conclude that when the incident radiation is hemi-spherical and the collection path is directional, it is equivalent to the incident radiation being directional and the collection path being hemi-spherical. This is demonstrated by Fig.8. In this figure, the point source at p_o irradiates spherical waves. Each wave is being obstructed by an aperture that allows a certain solid angle to pass. This

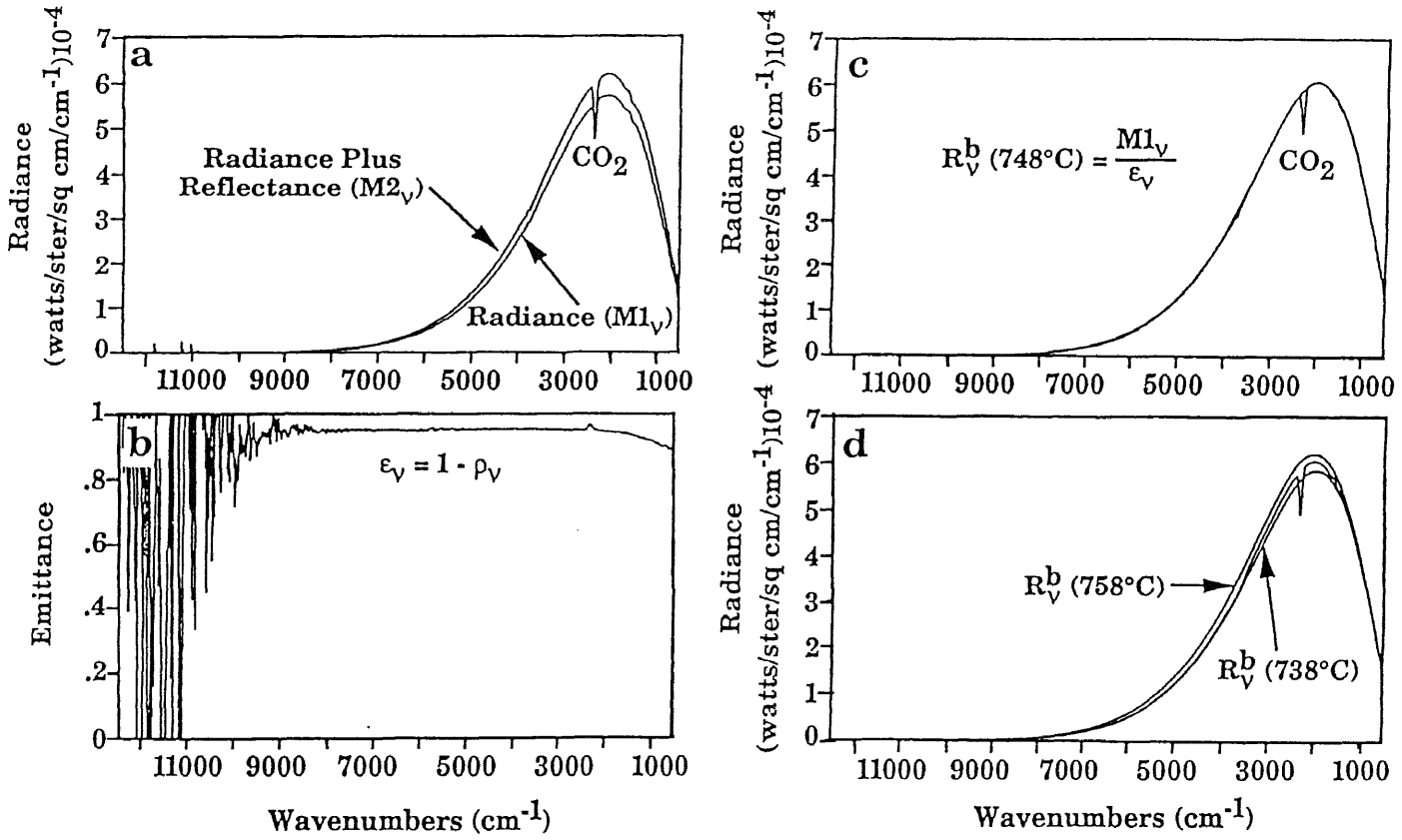

Fig.7 Spectral emittance and temperature determination for a hot surface of graphite G-96. a) Sample radiance (chopper closed) compared to radiance + reflectance (chopper open), b) spectral emittance by closure $\varepsilon_\nu = 1 - \rho_\nu$, and c-d) surface temperature determination by overlaying radiance/ε_ν with theoretical blackbody temperature curves.

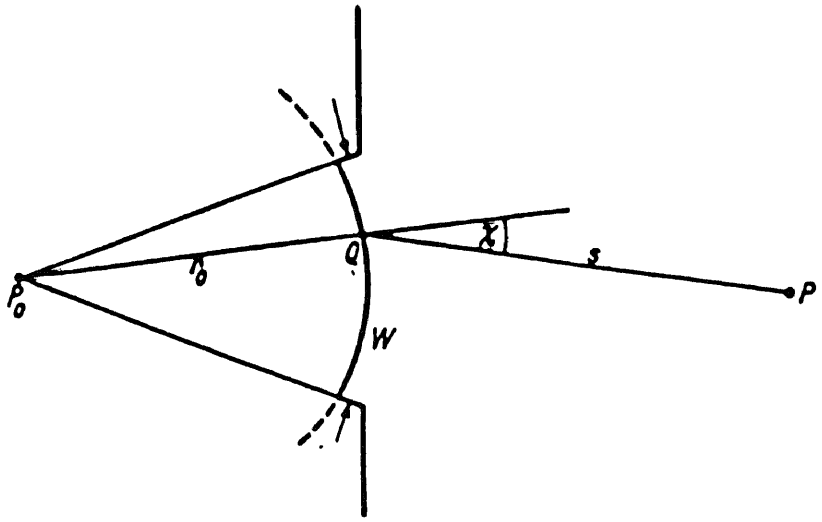

Fig.8 Illustration of the Helmholtz reciprocity theorem

allows some part of the radiation to be collected at p directionally. The same effect will be produced at p_o if a point source with the same intensity is situated at p. In the emissometer case, the blackbody represents p_o since it is exciting the sample hemi-spherically, and the paraboloid mirrors in both the reflection and transmission paths represent the point p or the collection point directionally. This methodology has been accepted as the best way of measuring the radiative properties of any material [37]. In Fig.9, the collection paths are demonstrated, with the path being illuminated using laser 1, which is used for alignment purposes before the actual experiment takes place.

4.4 Applications of Emissometry

In addition to the important radiative and optical properties that the spectral emissometer obtains it is also capable of:

I) Verifying the existence of components or impurities in the sample as sharp features observed in the wavelength range of 1 μm (10000 cm^{-1}) to 20 μm (500 cm^{-1}). These peaks represent molecules such as:

(a) C in Si -- 607 cm^{-1},

(b) SiO_2 -- 1110 cm^{-1},

(c) interstitial oxygen in Si -- 1130 or 900cm^{-1},

(d) water -- 1600, 3500 cm^{-1},

(e) CO_2 -- 2400 cm^{-1},

(f) Si_3N_4 -- 1206 cm^{-1}.

II) Determining the concentration of O_2 molecules depending on the size of the peak [38].

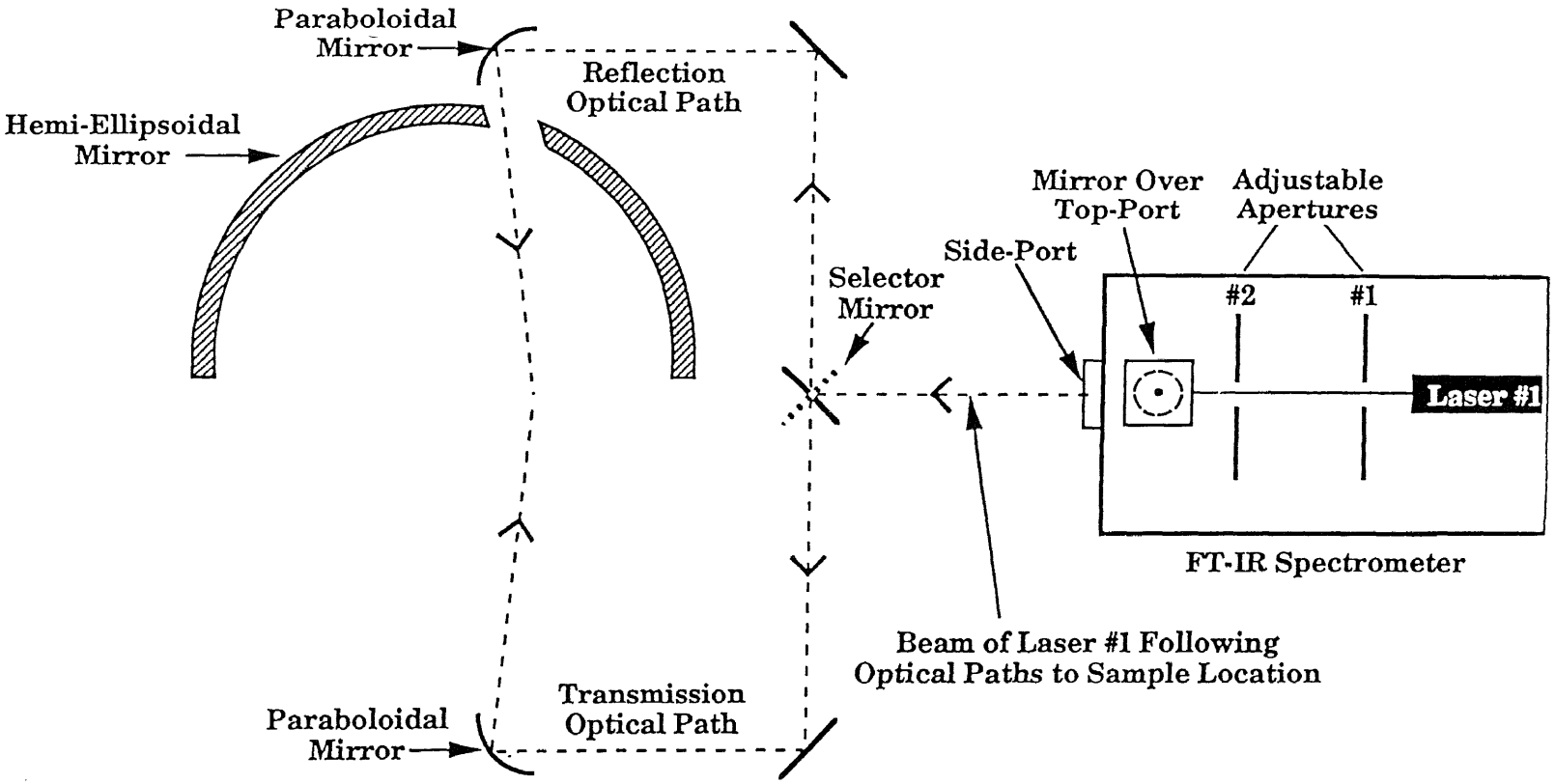

Fig.9 Top-view schematic of the beam collection paths of laser #1, reflection and transmission, when FTIR spectrometer is aligned with transfer optics and hemi-ellipsoidal mirror.

III) Ability to detect changes in thickness of the dielectric interfaces at refractory metal base barrier, W-Si-N/SiO_2/Si or structural changes in W-Si-N after RTA [39].

IV) Ability to detect changes in titanium films on silicon from C49 to C54 structures of $TiSi_2$ by analyzing emissivity changes [40].

V) The determination of electron and hole masses [41] or the optical mobilities once the absorption coefficient is known as [42].

CHAPTER 5

RESULTS AND DISCUSSIONS (I)

5.1 Double-Side Polished Crystalline-Silicon Wafers

The applications of spectral emissometry to obtain emissivity as function of wavelength and temperature for various types of silicon are illustrated in the following two chapters.

Two double-side polished low doped silicon wafers have been considered in this part of this study: a) n-Si, orientation <100>, t = 650 microns, ρ = 1--3Ω·cm and b) p-Si, orientation <100>, t = 250-275 microns, ρ = 10--100Ω·cm.

In. Fig.10, the experimentally obtained results of the transmittance, reflectance and emittance spectra of the n-type double-side polished Si wafer are presented for two different temperatures: 30 and 947°C. As can be seen in Fig.10, the emittance of this wafer is negligible at room temperature while at high temperatures, it approaches that of a gray body and saturates around 0.7. At room temperature, the transmittance of this wafer is shown to be in excess of 55% of the incident light. As a matter of fact, double side polished silicon wafers are considered as IR windows and are used in making silicon micro lenses that can enhance the efficiency of charge-coupled devices (CCD) [4]. As the temperature is increased to 947°C, the wafer becomes opaque. It is also important to notice that the reflectance is decreasing as function of temperature from above 0.42 to below 0.35. The sharp features below 2000cm^{-1} (5 μm) are mainly due to lattice vibrations in silicon [43]. In addition, some of the peaks are due to the existence of IR sensitive molecules in the wafer such as interstitial oxygen at 900cm^{-1} as has been pointed out in the

previous chapter. In Fig.11, the measured optical properties for the p-type double-side polished Si wafer are presented. In this figure, results similar to that in Fig.10 are obtained. The results of Figs.10,11 are expected and can be explained in the following manner:

Since the wafers resulting in the measured spectra as reported in the last two figures are double-side polished, they can be simulated by two parallel planes that sandwich a medium different from the above and below as described in Fig.5 but without the layers on the wafer. This medium has its own bulk properties of refractive index n and extinction coefficient k. As the light is incident on the top specular surface, a part of it will be reflected with an angle equal to its angle of incidence and a part will be transmitted after being refracted according to Snell's law

$$n_1 \sin\theta_1 = n_2 \sin\theta_2 \qquad (5.1)$$

where n_1, θ_1, n_2 and θ_2 are the refractive index and angle of incidence in air and the medium, respectively. For silicon, $n_2 \approx 3.43$. If the incident light is normal or slightly off normal to the top surface of the wafer, the reflected light intensity will follow from equation (3.5). In silicon the value of ρ is typically 0.3 and it rises as the temperature increases due to increases in n and k to the value of 0.32 at 800°C [28]. This is the true reflectivity of silicon. The rest of the light will transmit through the top surface with an intensity I_o. If the extinction coefficient k of this medium is very small or the medium is a dielectric, then the light travels with almost the same intensity throughout the bulk of the medium and impinge on the bottom plane. The ratio of the two intensities is given by equation (3.6). The true transmissivity of the medium is equal to unity and corresponds to

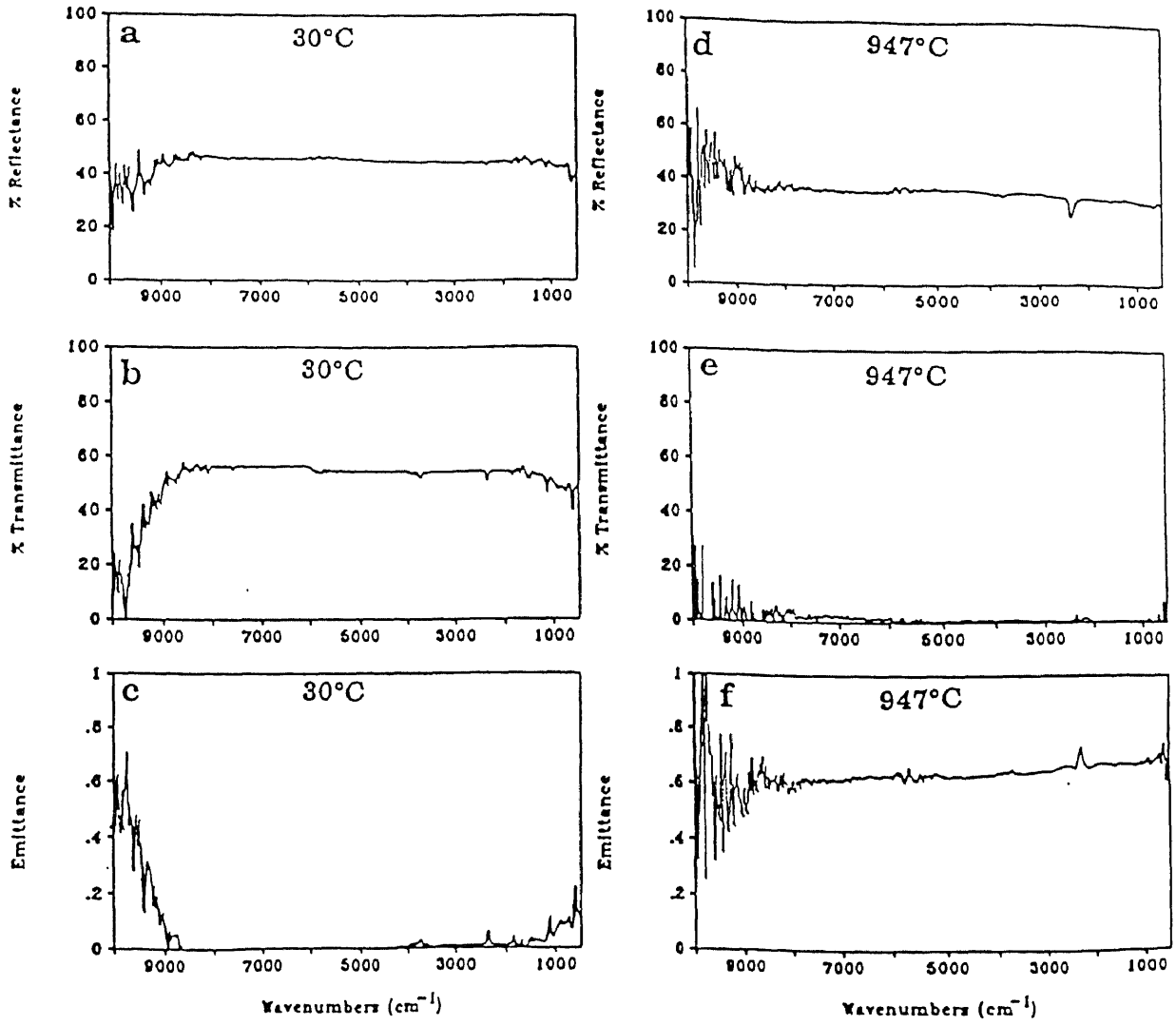

Fig. 10 Comparison of measured reflectance, transmittance and emittance of n-Si polished both sides at 30°C (a,b,c) and 947°C (d,e,f)

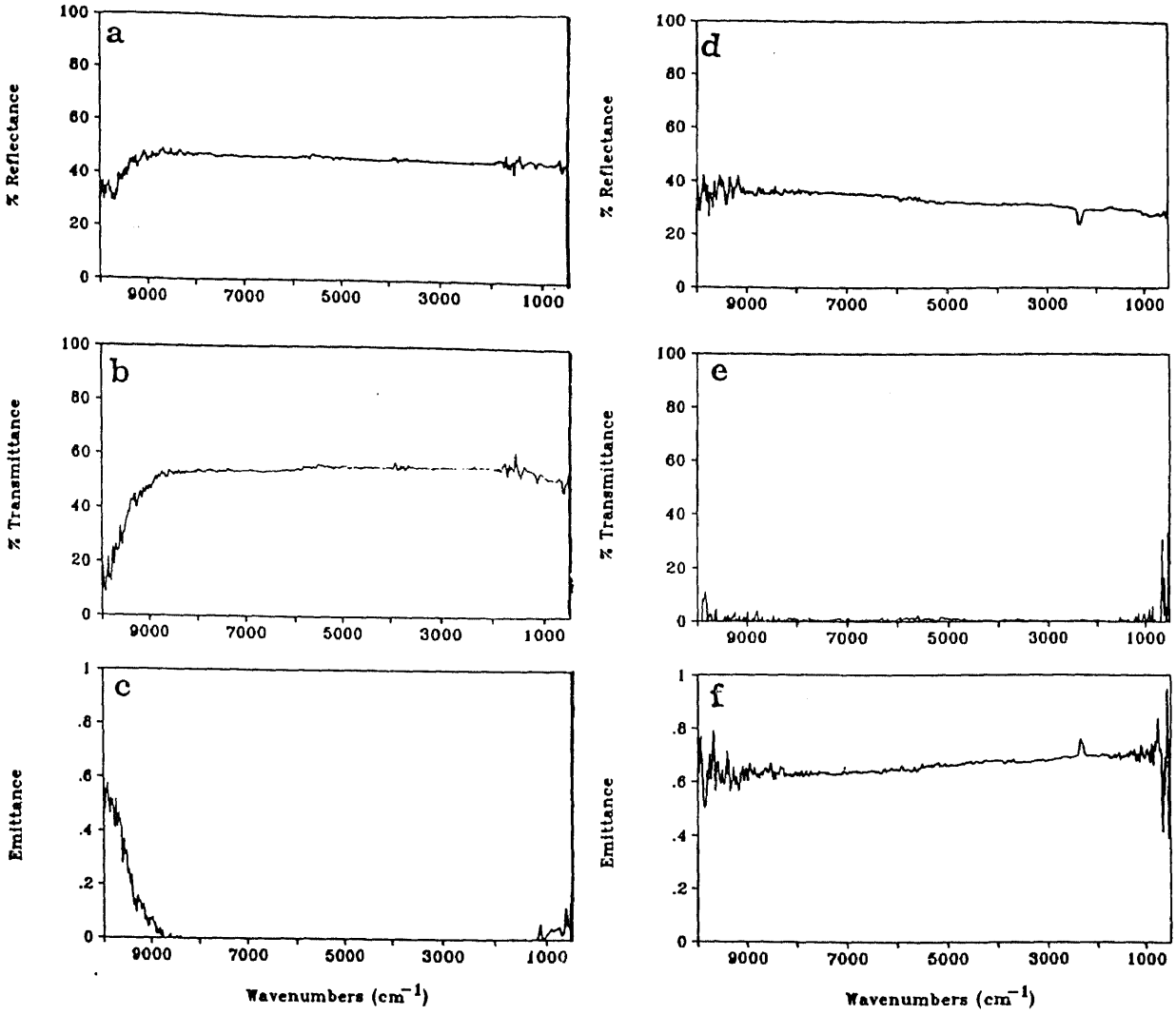

Fig.11 Comparison of measured reflectance, transmittance and emittance of p-Si polished both sides wafer at 24°C (a,b,c) and 900°C (d,e,f)

the absorption coefficient $\alpha(\lambda) \approx 0$. On the other hand, if the medium is an absorber, i.e. k is appreciable, then the transmitted light will be attenuated as it is traveling throughout the medium towards the bottom plane. As the light beam impinges on the bottom plane, it will posses a new intensity I_1 in which the ratio $I_1/I_o < 1$ and $\alpha(\lambda) = 4\pi k(\lambda)/\lambda$ becomes appreciable. As can be seen in Fig.5, part of the light impinging on the bottom plane gets reflected and the rest will transmit through the plane and into the air again. The same applies to the light reflected at the bottom and top plane. The spectral emissometer detects the signal reflected and is denoted by ρ^* as in equation (3.9) for reflection and the signal transmitted is denoted by τ^* as in equation (3.8). These are referred to as apparent reflectivity and apparent transmissivity, respectively. By looking carefully at (3.8) and (3.9), which are the result of multiple-internal reflections and will be derived below, it becomes clear why the apparent reflectivity of both the n-Si in Fig.10 and the p-Si in Fig.11 is different from 0.3 (in both figures $\rho^* > 0.4$). This difference is due to the contribution of the backside of the sample. The measured apparent transmissivity is the same for the two samples and is typical for samples under the same specifications. To understand the emissivity data, it is important to distinguish the various contributions to emissivity in different regions of the spectrum. It is known that the intrinsic emissivity, defined in chapter 4, of a specimen depends on the total absorption coefficient consisting of several contribution:

$$\alpha(\lambda,T)_{total} = \alpha(\lambda,T)_{bg} + \alpha(\lambda,T)_{ag} + \alpha(\lambda,T)_{fc} + \alpha(\lambda,T)_{phonon} \qquad (5.2)$$

where $\alpha(\lambda,T)_{bg}$ is the absorption coefficient due to the fundamental absorption edge, $\alpha(\lambda,T)_{ag}$ is the absorption coefficient due to above fundamental edge absorption, $\alpha(\lambda,T)_{fc}$

is the absorption coefficient due to the free carriers, and $\alpha(\lambda,T)_{phonon}$ is the absorption coefficient due to the phonon absorption. Absorption due to the fundamental edge is seen clearly from both Figs.10,11 from 10000-9000cm^{-1} or 1-1.1μm at room temperature. The second term in equation (5.2) is not within the wavelength range of our emissometer, 0.4-0.8μm. The absorption due to free carriers is dominant >1.5μm. At wavelengths > 5μm, the phonon contribution to the absorption in silicon starts being dominant at room temperature. Equation (5.2) applies to all semiconductors and is not restricted to silicon. Free carriers can be the result of two sources - a) thermal generation and b) impurities due to doping. Since both the samples used here are lightly doped as can be seen from the resistivity values, it is clear that the absorption due to free carriers at room temperature should be minimal. Equation (3.11) implies that under equilibrium, the absorptance is equal to emissivity. This explains the low emissivity of both n and p-Si at room temperature. As the temperature increases, more free carriers and hole-electron pairs are thermally generated, thus increasing the extinction coefficient $k(\lambda)$ and hence the absorption coefficient $\alpha(\lambda)$. Hence the attenuation of the light in a single pass through the wafer increases according to $e^{(-\alpha(\lambda)t)}$, with t being the thickness of the wafer. As a result, with increasing temperature and decreasing contribution of the backside, the apparent reflectivity decreases to ~0.32. This value is typical of true reflectivity of silicon at high temperature when the medium is fully opaque and the backside has no contribution [28]. The loss in both transmission and reflection is accounted for by increase in absorption.

In this section, an experimental study has been performed on thin double-side polished silicon slabs of various thickness - $t \approx 35\mu m$, ρ = 5.0-12.0Ω.cm, and $t \approx 10\mu m$,

and a low resistivity (with ±20% deviation in the wafer thickness). The details of the samples were supplied by the manufacturer, Virginia Semiconductors. The properties of the first sample of thickness t = 35μm is compared with the p-Si double-side polished sample of thickness t = 250μm. This study has been inspired in part by the pioneering work of Minkov and Swanepoel [44-50]. In their study, Minkov and Swanepoel use the interference fringes to determine the optical refractive index of thin dielectric films deposited on quartz substrates.

A number of studies aimed at determining the refractive index n and extinction coefficient k of silicon at various ranges of wavelengths and temperatures have been reported [51-57] in the literature. The most conclusive study so far has been by Li [58], in which he covered a wavelength range from 1.2 to 14μm and temperature from 100-750K. To the best of the knowledge of this author, no other study exists in the literature relating to these parameters at temperatures above 600°C in the IR range, where the bulk silicon becomes opaque. Goldsmid et al. [59] have studied the emission of thin (10μm) silicon slabs up to 1200K but they have only reported the absorption coefficient at high temperatures. A complete knowledge of the bulk properties is of great importance to predict the behavior of very thin films of silicon when grown or deposited at high temperatures. Fig.12 shows a comparison of the optical properties of double-side polished silicon samples of thickness t = 35μm and t = 250μm, respectively. It is clear from this figure that the intensity of reflection and transmission are almost the same. At 5800cm^{-1}, where the wavelengths start becoming comparable to the optical path of the thin slab, and k attains smaller values, fringes start appearing. Another expected phenomenon is the

increase in the amplitude of the fringes with increasing wavelengths. This phenomenon is referred in optics as the visibility of the fringe [60]. Here, the intensity of each fringe is:

$$I(\delta) = \{\sin(\delta/2)/(\delta/2)\}^2 I_{max} \quad (5.3)$$

where

$$\delta = (2\pi/\lambda)(2ndcos(\theta)) \quad (5.4)$$

δ is the phase difference between the two or more interfering waves, θ is the internal incident angle and d is the film thickness. One observation in this analysis was an irregular variation of intensity as a function of wavelength rather than sinusoidal shape expected for fringes. This is due to the critical number of fringes, which is a function of the sample thickness, versus the resolution power of our instrument, i.e. $16cm^{-1}$. Thus, we were able to collect an average of 2.8 data points between every two fringes. Naturally, the next step is to perform the experiment on a thinner slab of double-side polished silicon with similar conditions and comparable resistivity with thickness $t \approx 10\mu m$. In Figs.13(a) and 13(b) the optical properties of the $10\mu m$ sample are shown as function of wavenumber (5000-500 cm^{-1})and wavelength (2-20μm), respectively. Fig.13(a) is utilized for the deconvolution of the refractive indices and Fig.13(b) is presented to show the resolved sinusoidal shape of the fringes. The idea is to compare the refractive indices acquired by the fringe method with those acquired from the reflectivity and transmissivity of a silicon slab. A comparison is made in Fig.14 in which we see that the fringe dependent refractive index n has irregular oscillations at short wavelengths. This is understandable since at such wavelengths the visibility of the fringes is small and the compatibility of the wavelengths to the optical path difference and hence phase difference is not good. Fig.15 shows the optical properties of

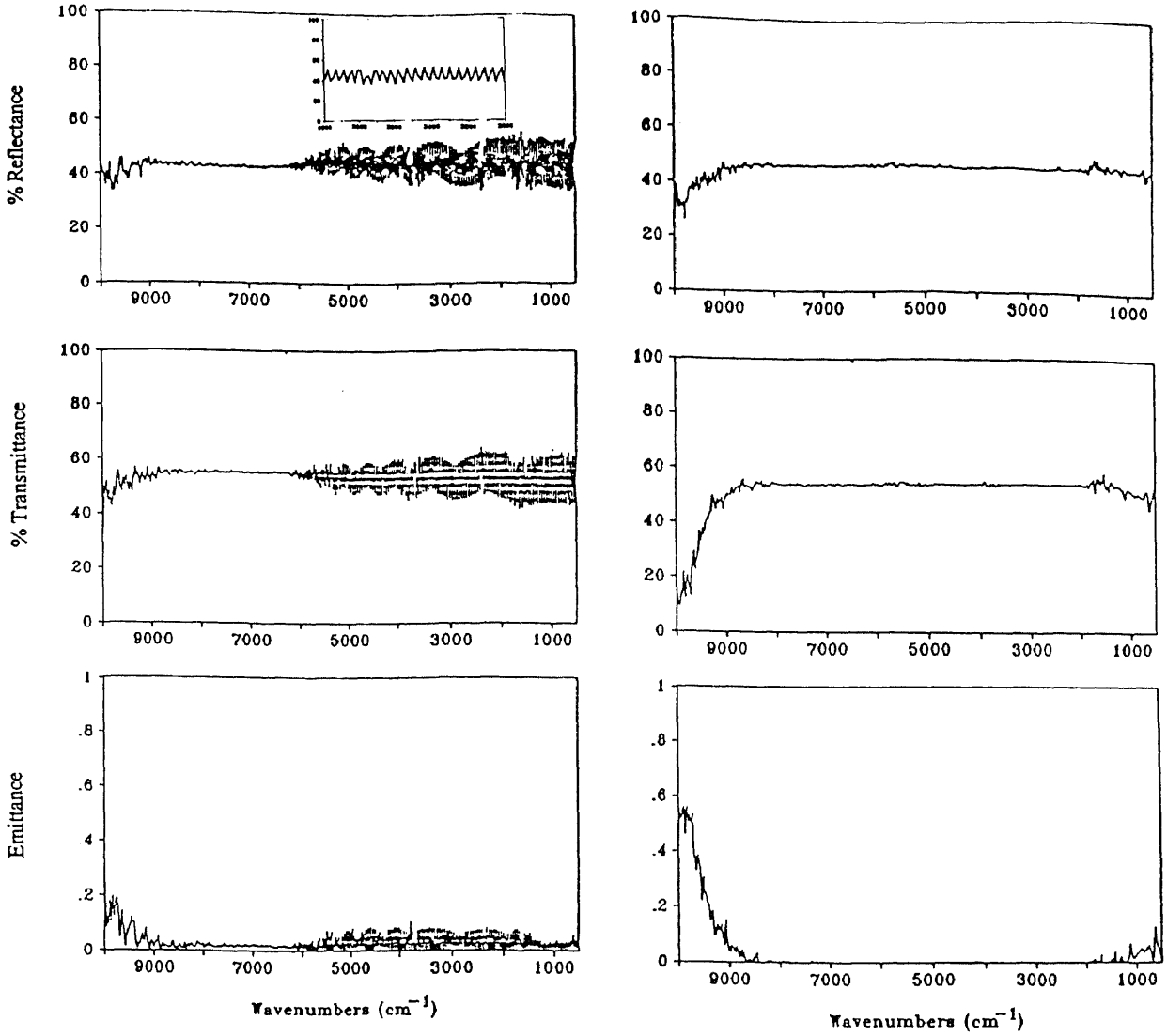

Fig.12 Comparison of measured reflectance, transmittance and emittance of (a) n-Si 35.2μm and (b) p-Si 250μm at room temperature

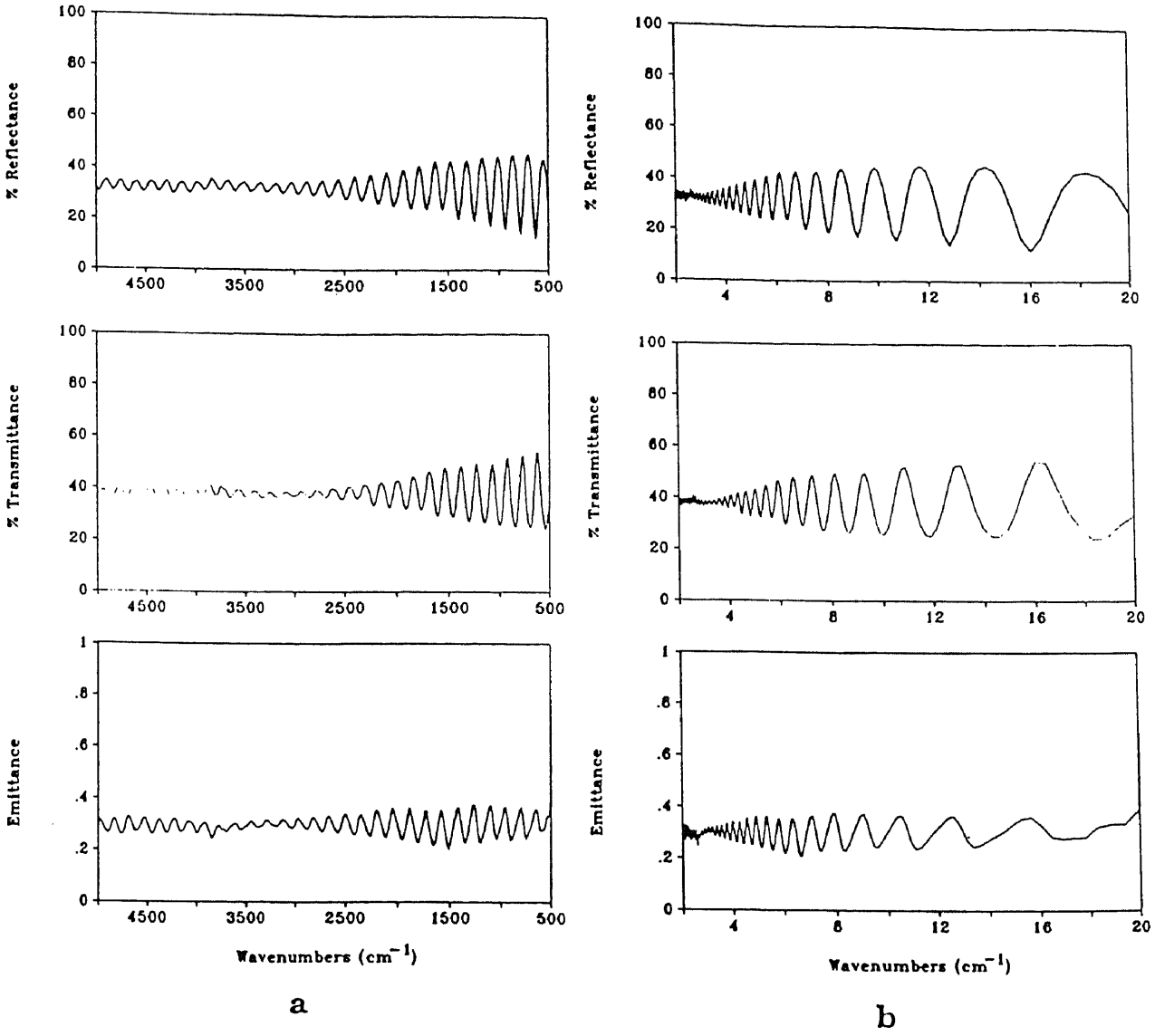

Fig. 13 Optical properties of ~10μm n-Si sample as function of (a) wavenumber (5000-500cm^{-1}) and (b) wavelength (2-20μm)

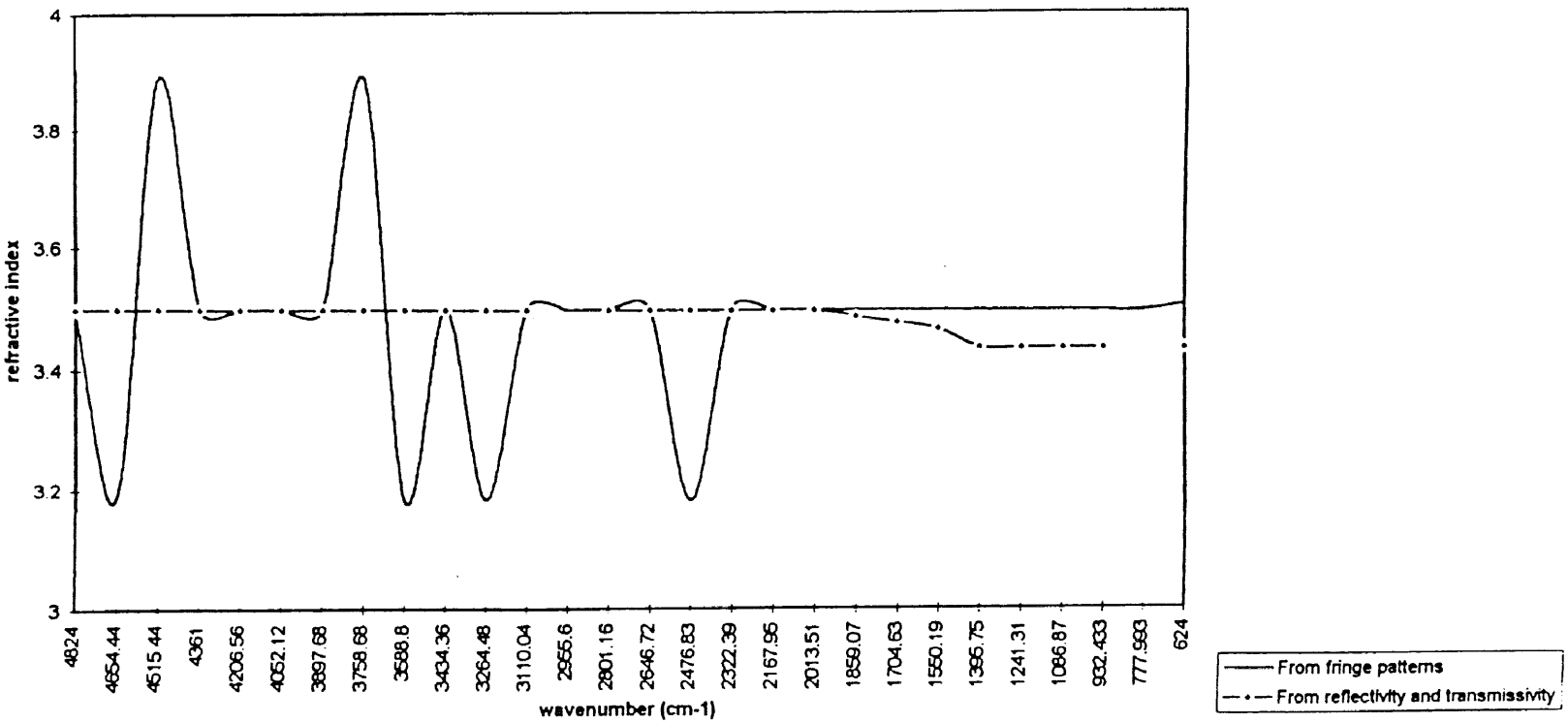

Fig. 14 Comparison of refractive index of ~10μm obtained by two different methods

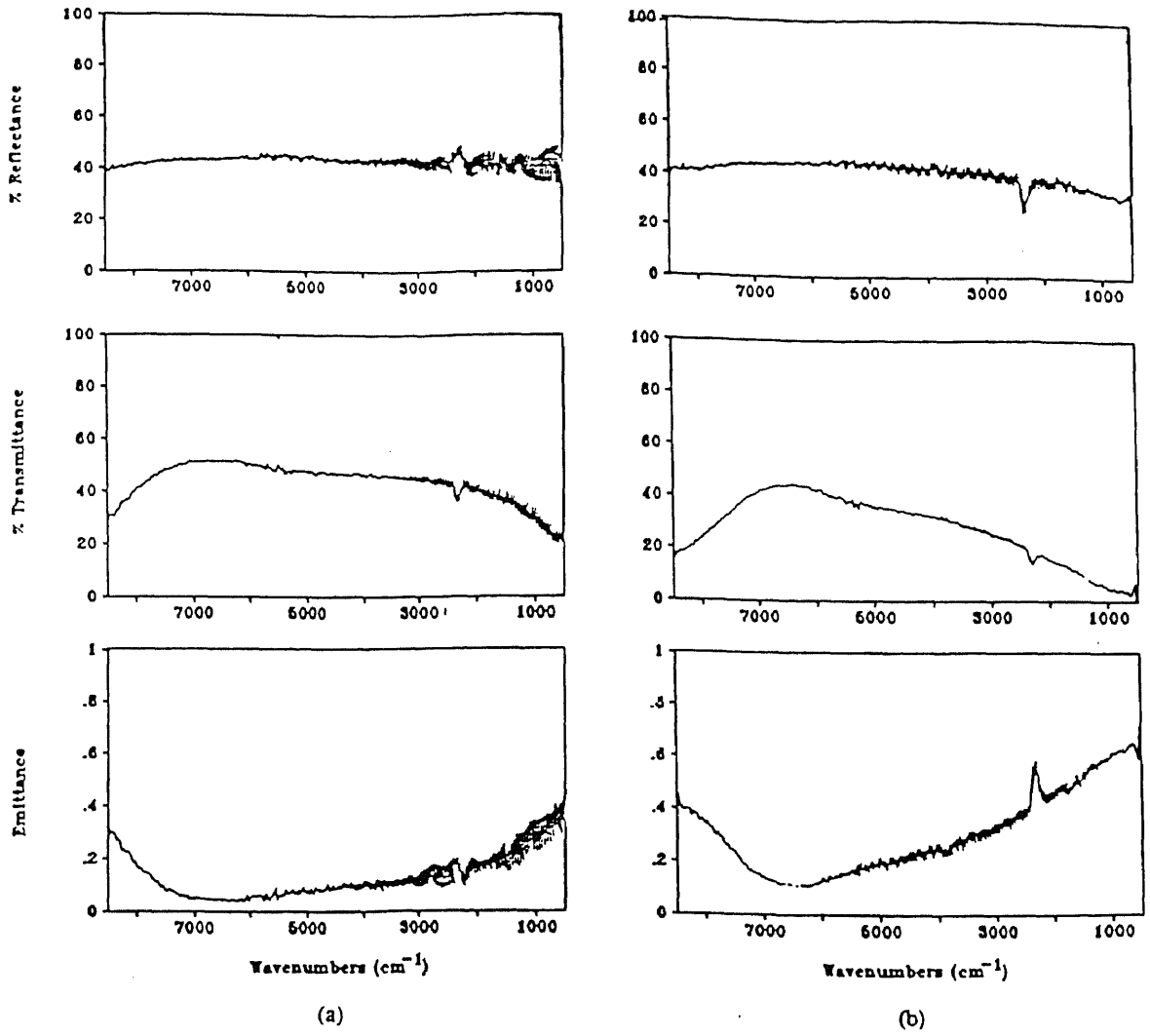

Fig.15 Measured reflectance, transmittance and emittance of ~35.2μm n-Si at two different temperatures, (a) 408°C and (b) ≥650°C

the 35μm thick sample at two different temperatures. We believe that due to the high specularity of the sample surface and the strong pressure induced by the heating source in the form of a flame which leads to vibration of the sample, the temperature fittings with Planck function are not so reliable. This work demonstrates the capability of the emissometer to yield important fundamental data such as n and k. Alternative methods of heating and temperatures measurements would be more desirable.

5.2 Single-Side Polished Wafers

In this section, measurements of the radiative properties on samples with single-side polish are considered. This study is extremely important because it represents the situation in the silicon industry currently. If the pyrometer is calibrated with double-side polished wafer, the influence of surface roughness of the monitored single-side polish wafers becomes a very practical and challenging problem. These aspects are discussed in this section.

In order to make a valid comparison with the double-side polished wafer, single-side polished wafer with similar specifications has been used. The wafer is n-Si, 650μm thick, <100>, ρ = 8-24Ω·cm which corresponds to $5.5\text{-}2.2\times10^{14}cm^{-3}$, respectively, with industrially rough backside of ~1μm. In Fig.16, the room temperature measured apparent reflectivity, transmissivity and emissivity of the polished side, light incident on the polished side, of this sample are shown. As can be seen in this figure, the effect of roughness on the optical properties seems to be considerable when compared with Fig.10. The difference in emissivity at room temperature is >0.08. This difference is due to surface roughness since the doping concentration of the two wafers is of the same order of magnitude. In order to understand the magnitude of roughness and its uniformity, (the emissometer focus size = 3mm) the surface morphology of the wafer has been analyzed utilizing a Burleigh Instruments Horizon-200 microscope and scanning electron microscopy (SEM) as shown in Figs.17 and 18. Over an area of $211\times211\mu m^2$, the roughness seems to be uniform according to Fig.17. The root mean square (rms) and average roughness are both ~1μm and the peak to valley extremes is up to 9μm. It can be seen from Fig.18 that even with extreme peak to valley values, the hills and the valleys look flat. To the best of our

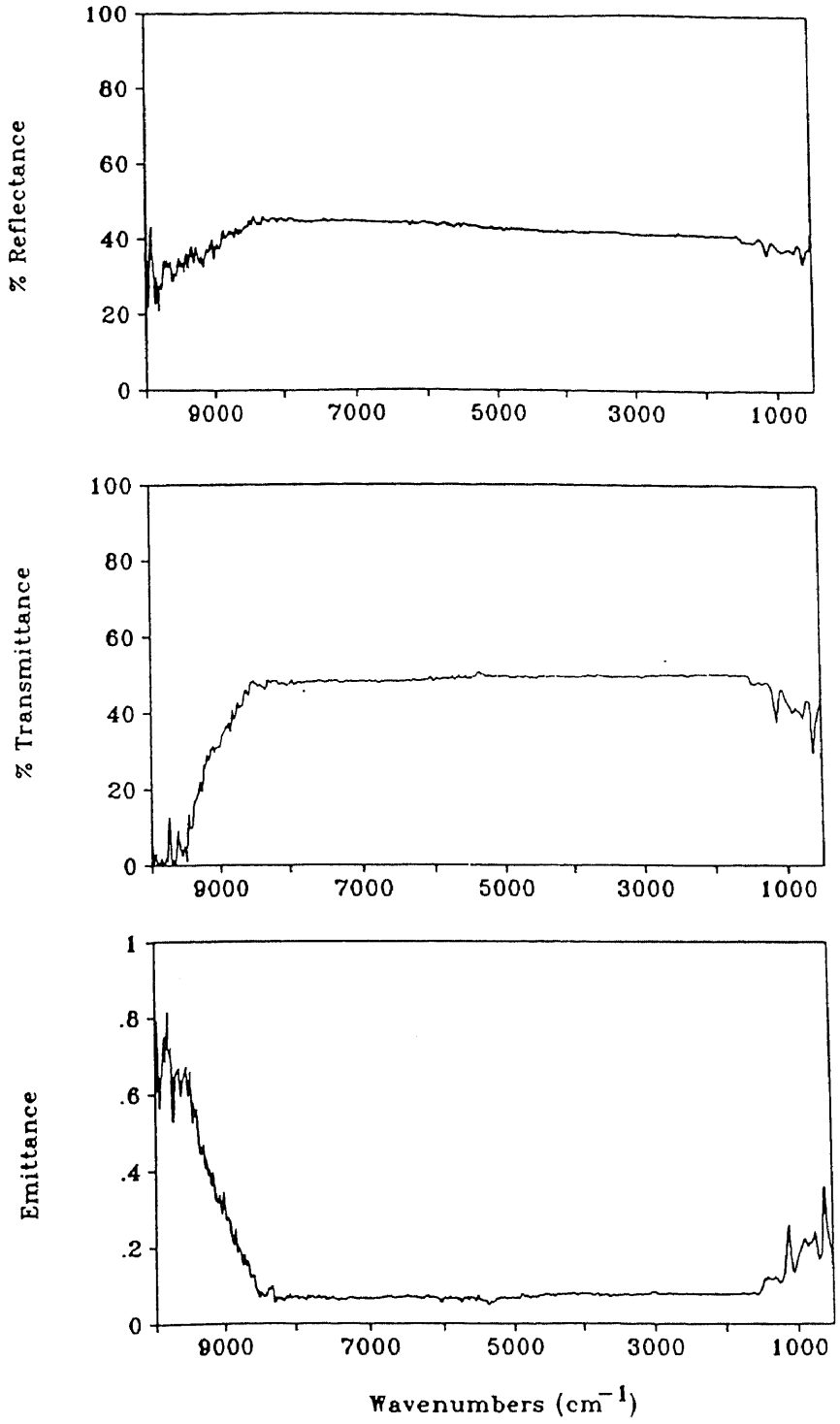

Fig.16 Measured reflectance, transmittance and emittance of the front polished side of a single-side polished n-Si at 45°C

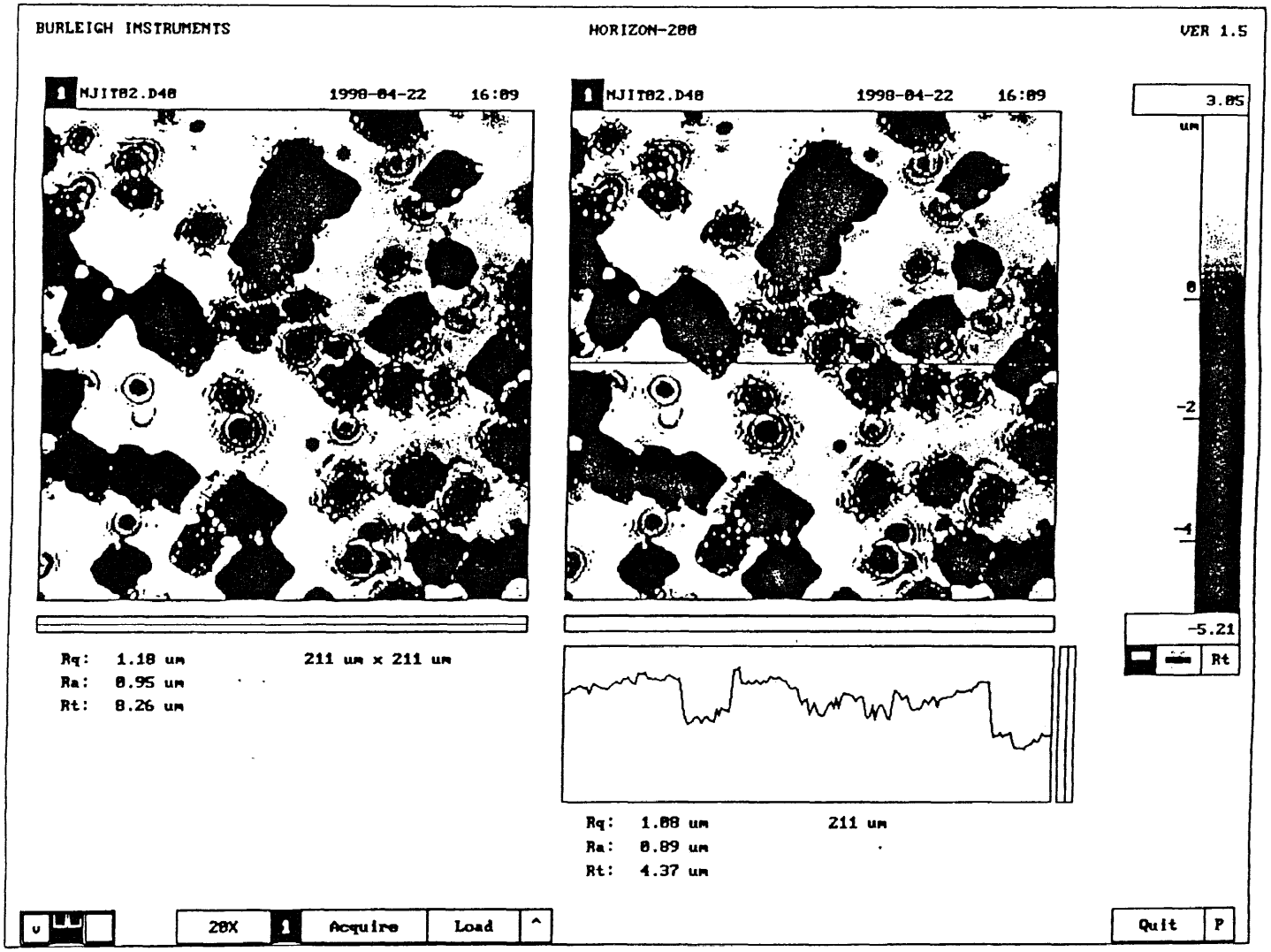

Fig.17 Horizon-200 optical microscope picture of the rough side of n-Si over an area of 211×211μm. Rq: root mean square roughness, Ra: average roughness and Rt: peak to valley roughness. Courtesy of Burleigh Instruments

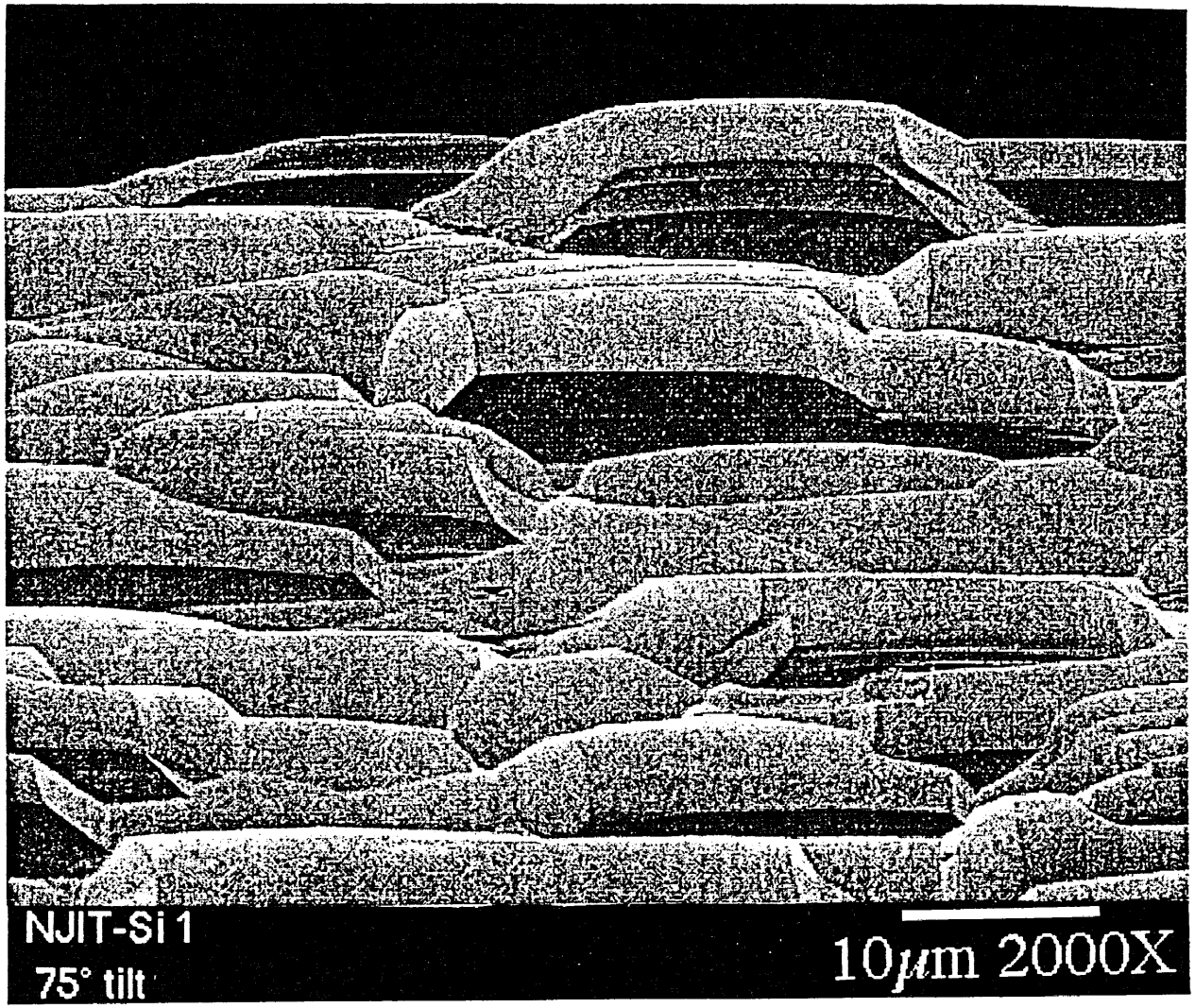

Fig.18 SEM (2000X) picture of the rough side of n-Si. The sample is tilted 75°.
Courtesy of Dr. B. Sopori and Mr. Wei Chen at NREL

knowledge, there only exist a few studies that are focused on the issue of roughness effects on the optical properties of silicon in the infrared range [22,61,62]. Only one study by Vandenabeele et al. has attempted to model the effect of roughness on emissivity of implanted silicon samples from 400-700°C, by a simplified one-parameter model [63]. In the following section the application of the Vandenabeele-Maex model on the experimental properties obtained in this work, to understand the effects of roughness on these properties, will be discussed.

5.2.1 The Vandenabeele-Maex (VM) Model

In their work, Vandenabeeble and Maex [63,64] have found that the influence of backside roughness on the emissivity is different for partially transparent and opaque wafers. For opaque wafers, only a slight dependence of the emissivity on roughness for rough-side incidence is observed, except for an extremely rough surface. For partially transparent wafers, a strong dependence of the emissivity on the roughness is observed. They modeled this by employing the same form for the expression (3.4) for emissivity, derived for smooth surface with the simple replacement of the true transmissivity $\tau_r(\lambda) = e^{-\alpha t}$ by an effective true transmissivity $\tau_r^*(\lambda) = Fe^{-\alpha t}$, linearly related to $e^{-\alpha t}$. Here F is a constant whose value lies between 1 and 0 according to the degree of roughness of the surface of incidence; F represents the ratio of the true transmissivity of rough-side incidence of the single-side polished sample to that of the double-side polished one. They have reported that this model works well. It is noteworthy that Vandenabeele-Maex (VM) have measured emissivity only for rough (backside) incidence for their single-side polished

samples and hence model for it. In other words, they have not made measurements for the smooth side of the single-side polished samples. It is also important to note that VM have measured only the emissivity of silicon for two discrete wavelengths - 1.7 and 3.4μm. They deduced the true reflectivity from the high temperature emissivity data by closure, i.e. equation (3.7), assuming that the reflectivity does not vary with temperature. They then substituted in equation (3.4) the value of true reflectivity and the measured emissivity at that particular temperature yielding the true transmissivity. The advantage in using equation (3.4) was that the change in transmissivity is somehow minimized even if there is a large error or change in reflectivity. VM have reported high value of F for smooth samples and low value of F for rough surfaces. The F value for the double-side polished wafer is considered to be 1. They have attributed the increase in emissivity with temperature for rough silicon wafers to the phenomena of light trapping and total internal reflection [22,61] which will be discussed in the next section.

5.2.2 Application of the Vandenabeele-Maex (VM) Model

The first step in this direction would be to get the optical properties of the rough backside, i.e. when the sample is excited from the backside (facing the inside of the mirror in Fig.6). In Figs.19(a)-(f), the emissivity as measured when the light is incident on the front polished side "smooth" and when the light is incident on the back rough side "rough" of the silicon wafer as a function of wavelength at specific temperatures is shown. As can be seen in these figures, the emissivity of the rough side is greater than that of the polished side. This remains the case until the sample becomes opaque to sub-bandgap radiation at

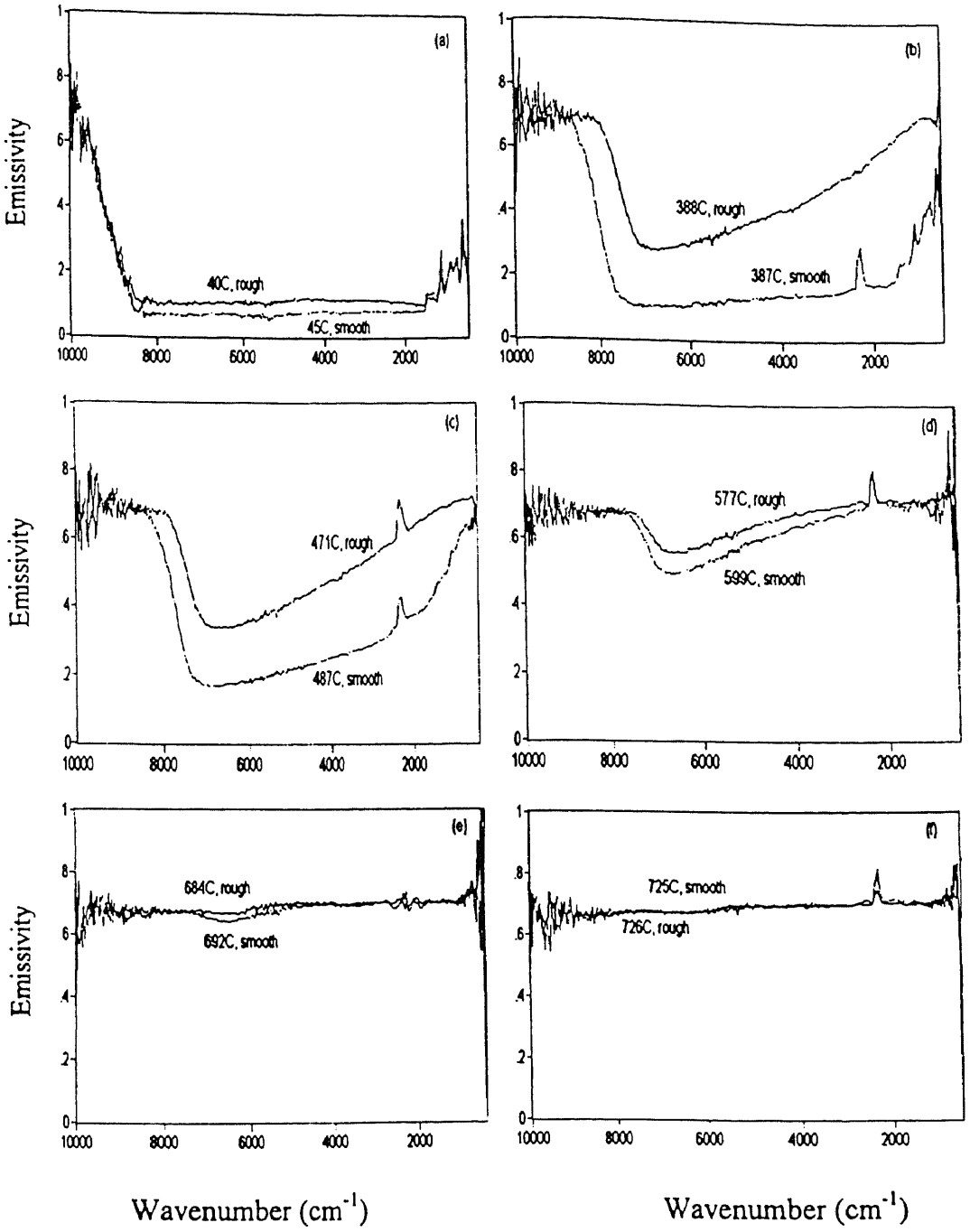

Fig. 19 Emissivity of back-rough vs. front-smooth sides of n-Si as function of wavenumber for specific temperatures: (a) 40, 45°C (b) 388, 387°C (c) 471, 487°C (d) 577, 599°C (e) 684, 692°C and (f) 726,725°C, respectively

temperatures above 700°C. In the range of temperatures investigated, the greatest difference in emissivities is observed at 387°C. Even though changing the surface morphology does not affect the optical constants of materials, i.e. refractive index n and extinction coefficient k, it does however change the absorptance of the substrate but in the following fashion:

Light beam incident on the rough side of the sample perpendicular to or with a slight angle of 15° with respect to the plane of the wafer, as in our experiment, faces non-uniform steps that could be modeled as V-grooves [63]. The sides of the V-grooves make acute angles with the incident rays. This may produce a backside angle of incidence of 16° corresponding to the critical angle of silicon whose refractive index n ~ 3.43. Once the interior angle of incidence exceeds the critical angle, the light is trapped and experiences total multiple internal reflection from the polished backside of the wafer until the inner angle of incidence becomes less than 16° whereupon the part of the ray is able to exit the sample. Eventually, the absorption mechanisms at the wavelength range of interest such as free carriers will lead to the absorption of photons in the material. The chance of having the same exact scenario for the light incident on the smooth, i.e. specular, side of the sample is minimal. Figs.20(a)-(c) show the transmittance and reflectance as measured from the front and the backsides of the same wafer compared for three representative temperatures. From these figures the major effect on the emissivities is seen to be from the change in transmissivities for the given sample for incidence on the polished side as opposed to the incidence on the unpolished rough side. In our measurements, the magnitude of the effect of roughness has been more to decrease the transmissivity than

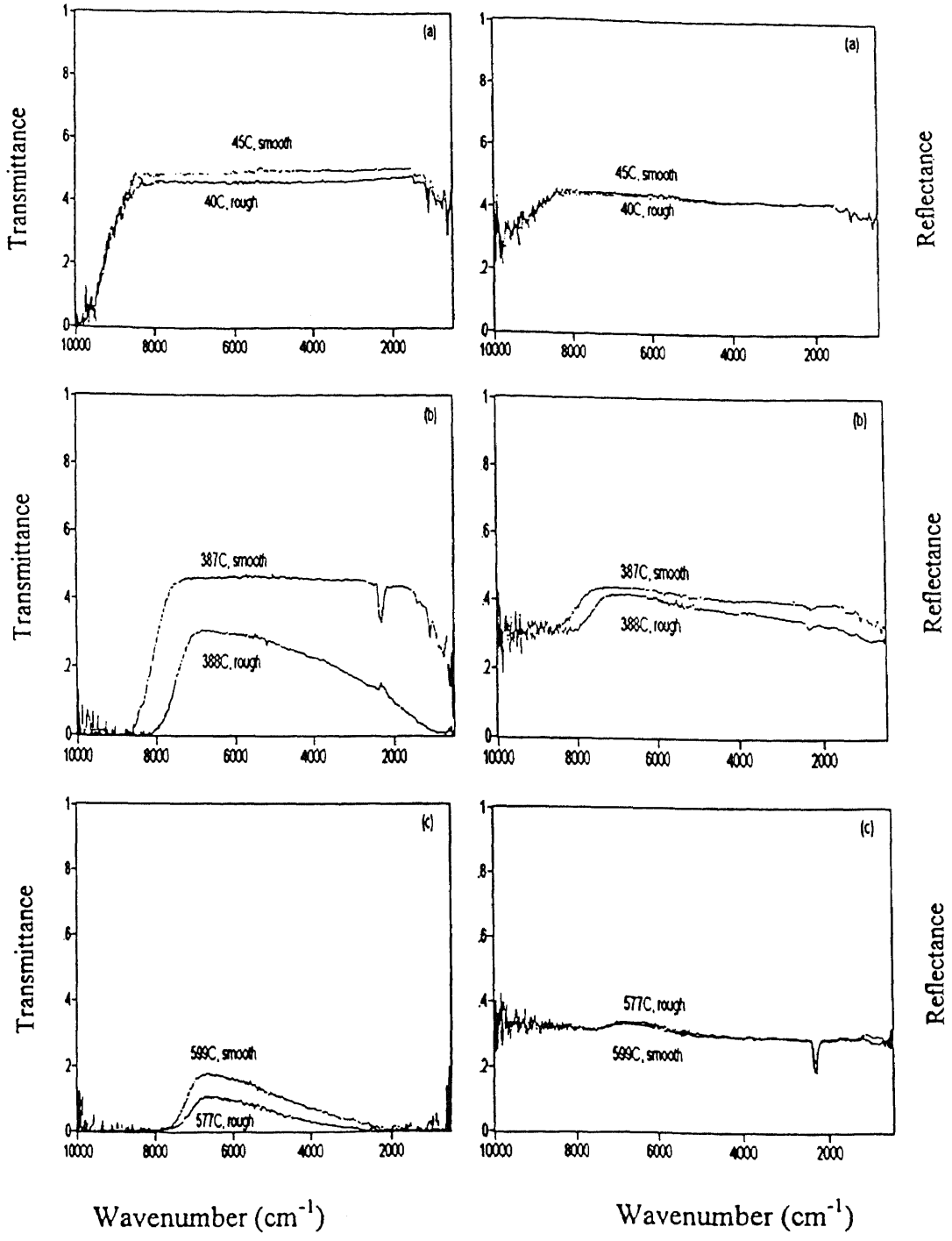

Fig.20 Transmittance and reflectance of the rough vs. smooth sides of n-Si as function of wavenumber for three specific temperatures: (a) 40,45°C (b) 388,387°C (c) 577,599°C, respectively

the reflectivity as function of temperature and wavelength thus leading to an increase in the emissivity. This shows that for opaque samples, roughness effects are minimal. This observation is in agreement with VM. One main concern regarding the data comes from the reflectivity. At room temperature it is seen that both the rough and smooth side incidence of the same wafer have the same apparent reflectivity. The same is true for temperatures near the opacity of the sample. The difference shown near 388°C could mean that the temperature might be off from the value given by the fit to the Planck's function. This issue will be addressed below. Figs.21(a)-(d) show the difference of the emissivities of the back and the front sides of the same silicon wafer for four specific wavelengths of interest to the RTP community. The change in emissivity $\Delta\varepsilon$ is maximum at 387°C independent of the wavelength of interest. At room temperature the contribution to the emissivity of silicon due to free carriers is low. At temperatures corresponding to opacity of silicon, the free carrier effects reach saturation equivalent to that of a gray body. Given that light trapping due to surface morphology is independent of temperature and that at high temperatures silicon becomes opaque, there must exist a temperature for which there is a maximum difference between the backside and front side emissivities. Our observations at 387°C are close to this condition.

In RTP, 400°C is a temperature commonly used for forming alloys and contact formations and as such is a representative temperature for the RTCVD era. Thus, a thorough knowledge of the effect of surface morphology on wafer emissivities is needed for temperature calibration. As a matter of fact the calibration problem could be particularly severe in RTP if the pyrometer has been calibrated with double-side polished

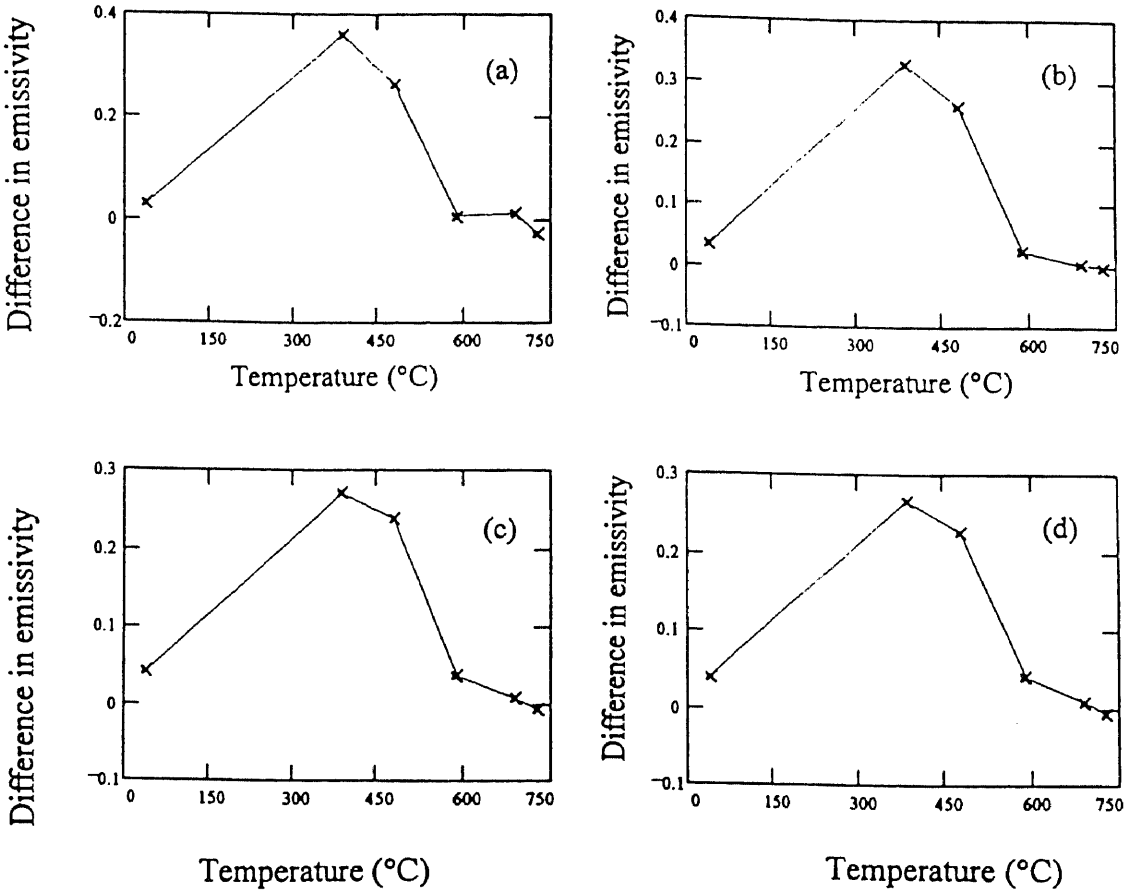

Fig.21 Difference in emissivity as function of temperature for four specific wavelengths: (a) 4.5, (b) 3.3, (c) 2.7 and (d) 2.5μm

or smooth side of a single-side polished wafer and monitoring the rough backside of a wafer heated by lamps from top with near/or at normal incidence. According to our results, this means that the pyrometer will detect less transmitted radiation from the lamps, at temperatures below the opacity of silicon, than from a double-side polished wafer and more transmission than if the pyrometers are detecting the smooth side with the rough side being heated. This causes errors in calibration for the unwanted transmission and hence in temperature measurement.

At energies less than the bandgap, the main mechanism for the absorption of radiation in Si samples is free-carrier absorption with an absorption coefficient given by [65]:

$$\alpha = e^2 N / \varepsilon_o c n m^* \omega^2 \tau \qquad (5.5)$$

where $\omega = 2\pi c/\lambda$, N = density of free carriers, n = refractive index, m^* = conductivity effective mass, τ = the relaxation time at frequency ω. Towards longer wavelengths the absorptivity of the free carriers is enhanced, increasing the absorption of the light being trapped inside the wafer with a concomitant increase in $\Delta\varepsilon$. This effect can be seen in Fig.19 up to the temperature at which the sample becomes opaque.

One interesting feature seen in absorptivity in Fig.19 that cannot be explained by the free carrier mechanism is the shift to longer wavelength of the absorption edge for rough side incidence as compared to smooth side incidence. Since the band gap of semiconductors is a bulk property, it is hard to explain this experimental observation. In quantitative terms at 387°C the maximum shift is 0.14μm corresponding to an apparent band gap shift of -0.10eV. There is an alternative way this apparent "horizontal" shift of

the edge could arise, namely by a vertical displacement of the sharply rising portion of the "rough" trace, i.e. an increase of ε (although in no way could this be a "uniform translation"). This latter interpretation is in fact strongly supported by the following argument*:

Let us make the not unreasonable assumption that ε depends only on two factors: the absorption coefficient α and "geometry", i.e. degree of roughness, and we further assume that in the present context α is an intrinsic property solely a function of wavelength and that the "geometrical effect" is independent of wavelength. Now consider any energy on the absorption edge, let's say for definiteness ~ 7700cm^{-1} in Fig.19(b), and note the corresponding two values of emissivity, ε = 0.2 (smooth trace) and ε = 0.6 (rough trace). Upon projecting there values, ε = 0.2 and ε = 0.6, parallel to the horizontal axis across the minima of the traces to the right side of the figure one obtains a second pair of intersections at ε = 0.2 and ε = 0.6 for smooth and rough traces, respectively. The important observation is that these intersections occur at essentially the same energy, ~1600cm^{-1}. But in this low energy regime of free carrier absorption the difference in ε from smooth to rough can be rather unequivocally ascribed to roughness enhanced absorption. Therefore, the corresponding difference in pairs of e values on the absorption edge must similarly be due to roughness enhanced absorption with no need to invoke an energy shift of the edge. In other words the apparent edge shift can be completely accounted for in terms of enhanced absorption in the "rough" case, i.e. "vertical" shift rather than a "horizontal" shift.

* J.C. Hensel, Physics Dept., NJIT, personal communication, May-Aug. 1998

Following the steps used by VM in the application of their model, the true transmissivities can be obtained in the following manner:

I) Use the 250μm thick double-side polished (DSP) p-Si lightly doped which allows comparison with a similarly lightly doped single-side polished (SSP) n-Si sample in the intrinsic temperature regime, T~400°C.

II) The temperatures chosen for comparison are : (a) 40, 20, (b) 388, 359, (c) 471, 479 (d) 577, 605, (e) 684, 632 and (f) 726, 759°C for the SSP and DSP, respectively. Obviously the temperatures are not an exact match but are close to each other in the range where the thermally generated free carriers play the dominant role throughout the range of wavelengths considered and they are off at the non-sensitive region slightly below and at the opacity level of silicon. For the "extrinsic" comparison, pair (a), the difference in mobilities between majority carriers in both samples tends to offset the fact that the carrier concentration of the n-Si is substantially higher than p-Si.

III) To obtain true reflectivity of both SSP and DSP, the closure relation for high temperature emissivity data has been used, i.e. equation (3.7).

IV) Rearrange equation (3.4) to obtain the transmisivities:

$$\tau = ((\varepsilon(\lambda,T)/(1 - \rho(\lambda,T))) - 1)/((\rho(\lambda,T)\varepsilon(\lambda,T)/(1 - \rho(\lambda,T))) - 1) \qquad (5.6)$$

V) Obtain α (cm^{-1}) for the DSP by rearranging equation (3.6) to:

$$\alpha = -\ln(\tau(\lambda,T))/(250\times10^{-4}) \qquad (5.7)$$

then the τ is scaled to 650μm to simulate the SSP wafer.

VI) Finally extrapolate each point of $[F(x,y) = F(\tau_{DSP}(T), \tau_{SSP}(T))]$.

But before discussing the results of these simulations, it is important to show the small influence of large changes ρ, which is known not to change by more than 0.02 [28], on τ. So first if the apparent reflectivity at room temperature from Fig.20 (a) is taken at both 1.7 and 3.4μm (0.438 and 0.418, respectively) to be the true reflectivity and is substituted in equation (5.6) it results in $\tau(1.7) = 0.895$ and $\tau(3.4) = 0.873$. Subsequently, considering the reflectivity values as VM suggested, i.e., at 726°C, $\rho(1.7) = 0.313$ and $\rho(3.4) = 0.302$, we obtain $\tau(1.7) = 0.898$ and $\tau(3.4) = 0.878$. These results prove that VM choice of reflectivity does not affect the transmissivity values and is appropriate.

The results of the application of the VM model to interpret the emissivity of SSP and DSP silicon samples in terms of the *F* factor are shown in Figs.22(a),(b). The six data points available to us for the plot is sufficient to show a trend in the rough side transmissivity of the SSP as function of the transmissivity of the DSP. As can be seen in Fig.23(a) the linear relation proposed by VM is not valid at two regions. The first is the low temperature regime ($\tau>0.9$). The other regime is at temperatures higher than 577°C ($\tau<0.2$). This is because the absorption in SSP owing to roughness is higher than that in DSP at similar temperatures. Similar conclusions can be drawn from Fig.22(b) except for the fact that at 3.4μm α is much larger than at 1.7μm. The results of the simulated transmissivity data for DSP as calculated by Multi-Rad (see sections 5.3.2 and 7.3) and the measured transmissivity data for SSP (rough side incidence) are summarized in Figs.23(a),(b) [66]. In this figure, it is clear that *F* is not a straight line confirming the previously obtained results in Figs.22(a) and 22(b). As a matter of fact, the plot is almost an exponential. In order to make the factor *F* look linear, the low and high temperature

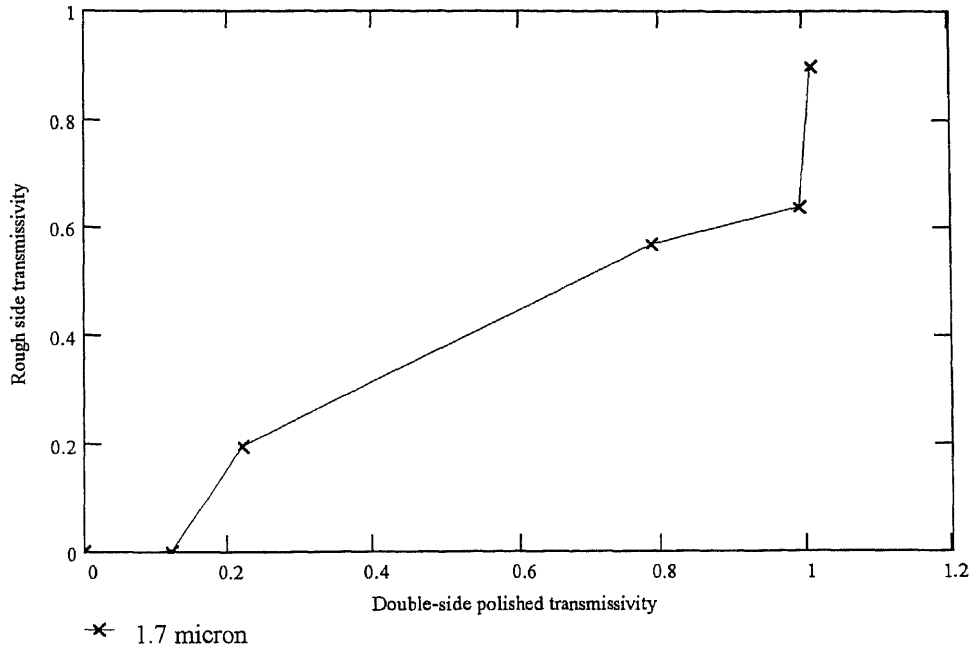

(a)

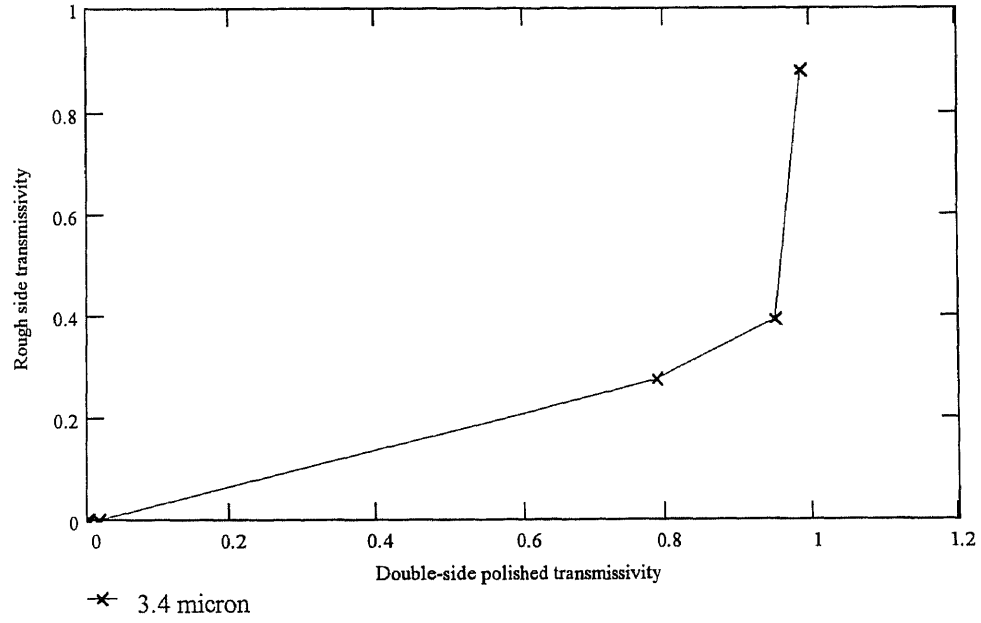

(b)

Fig.22 Correlation between the true transmissivity of the double-side polished p-Si wafer and of that of the rough side of the single-side polished n-Si wafer for (a) 1.7 and (b) 3.4 micron

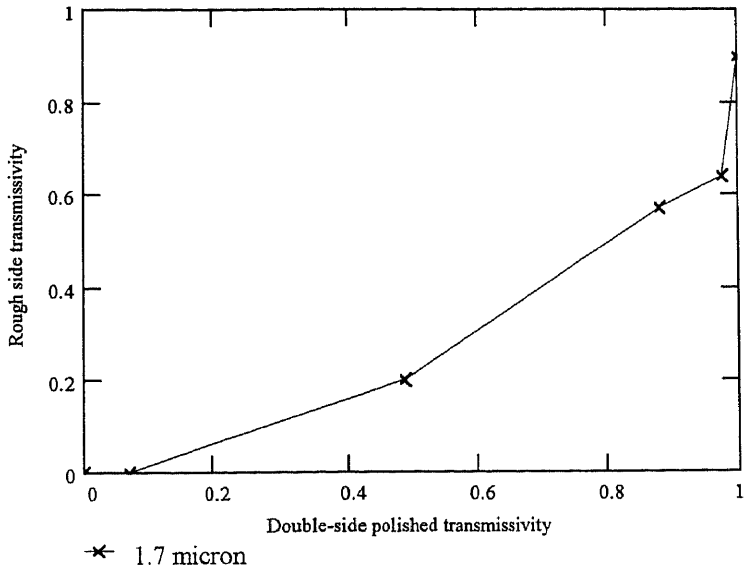

(a)

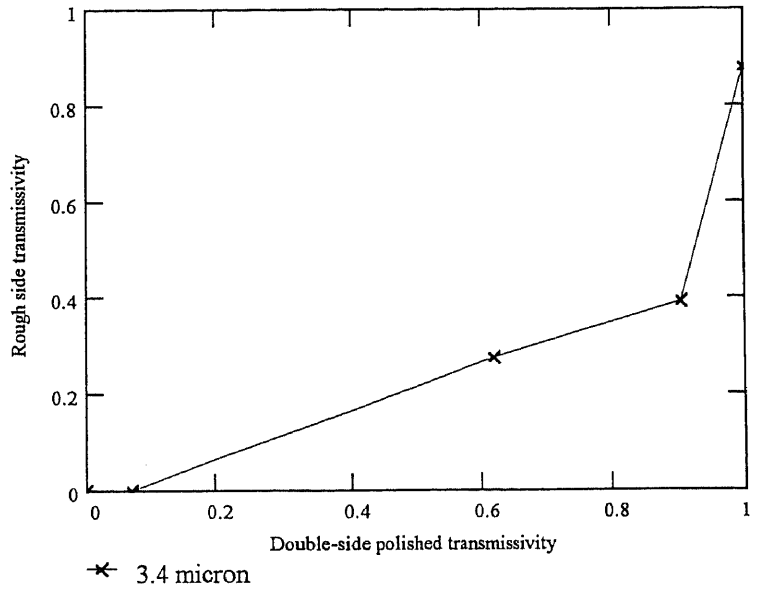

(b)

Fig.23 Correlation between the true transmissivity of a double-side polished n-Si wafer as calculated by Multi-Rad and of the measured rough side incidence of the single-side polished n-Si wafer for (a) 1.7 and (b) 3.4 micron

data have to be omitted. The deviation from linearity is not apparent in VM analysis because of the restricted range of the data. In reality, the model does not work and has many limitations.

5.2.3 Effective Path Length in SSP Wafers

One can express the factor F in the following way from its definition:

$\tau_{SSP}/\tau_{DSP} = \exp(-\alpha t_{SSP})/\exp(-\alpha t_{DSP}) = \exp(-\alpha \Delta t)$, where Δt is the difference in the effective light paths in the rough and smooth samples.

Assuming the transmissivities ratio or F factor to be valid, Δt is determined in an attempt to give a physical interpretation to the problem and the results are summarized in Figs.24(a)-(e). In order to obtain this difference in the light path, the absorption coefficient $\alpha(\lambda,T)$, corresponding to doping concentration = $5.8\times10^{14}cm^{-3}$ added to the thermally generated free carriers is determined using a numerically fitted equation [63] (cm^{-1}):

$$\alpha_{fc}(\lambda,T) = 1.069 \times 10^{21} \times (\lambda^{1.51})(T^{1.45})N(T) \qquad (5.8)$$

where N is the total number of free carriers. Effective thickness is determined by (μm) by:

$$\Delta t = \ln(\tau_{smooth}(\lambda,T)/\tau_{rough}(\lambda,T)) \times 1/\alpha_{fc}(\lambda,T) \times 10^4 \qquad (5.9)$$

As can be seen from Fig.24, the values of effective thickness at low temperature are much larger than the wafer thickness - a possible implication of a large number of multiple internal reflections.

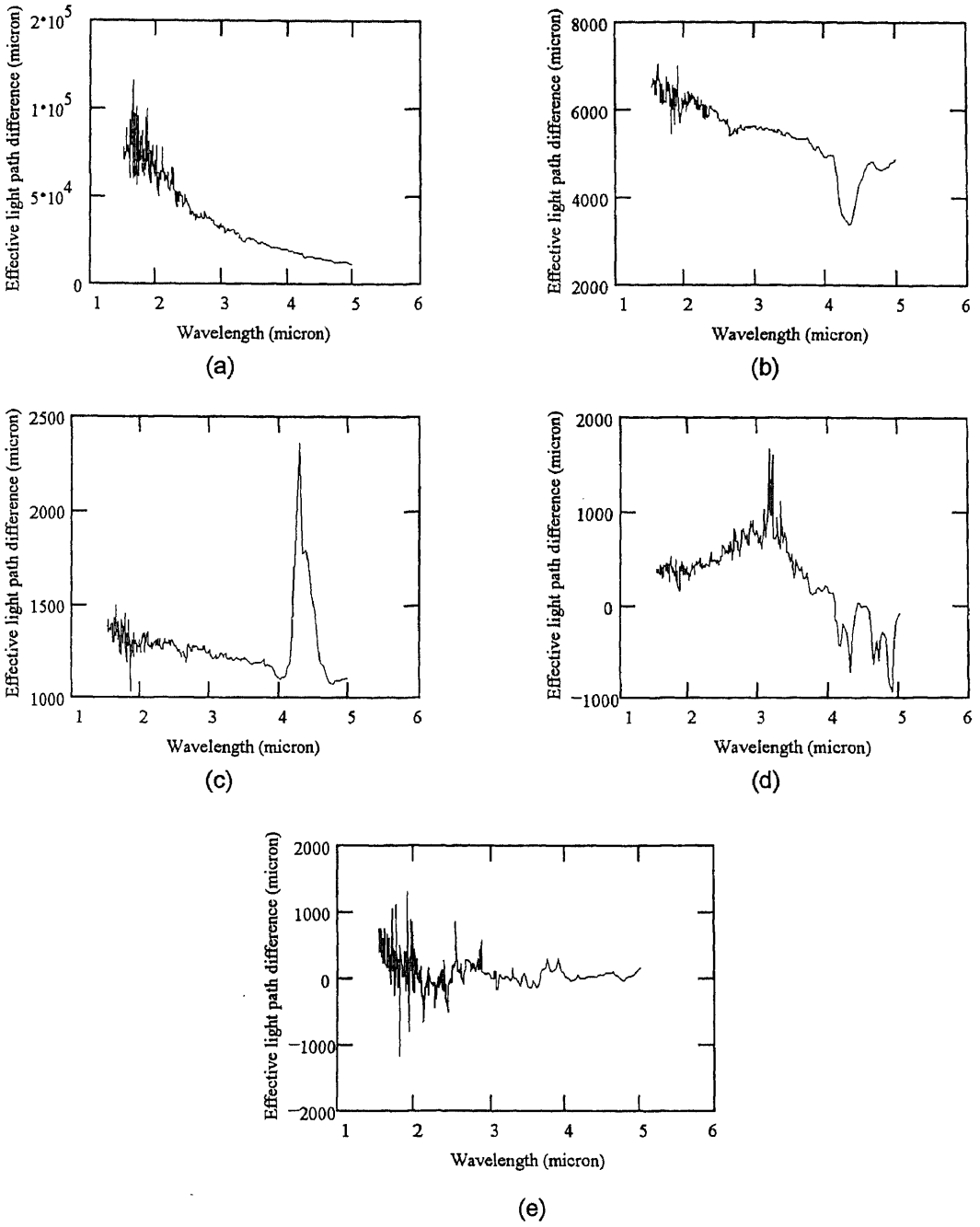

Fig.24 Difference between the effective light path with incidence on the rough side and that with incidence on the smooth side of an n-Si for: (a) 40,45 (b) 388,387 (c) 471,487 (d) 577,599 and (e) 684,692°C for rough and smooth, respectively

5.2.4 One-parameter Model Vs. Two-parameter Model and Some Suggestions

It has been shown in the previous section that VM model has limitations. In order to understand its weaknesses, a thorough analysis has to be made.

It has been shown that the model gives the emissivity as a function of the true transmissivity, i.e., equation (3.6), while keeping the true reflectivity constant. Thus, the only variable is the absorption coefficient α. Hence it is a one-parameter model. It is reasonable, therefore, to attempt to work the problem in a forward calculation to investigate the problems with the model in the following manner:

I) Multiply Δt by α to yield a dimensionless parameter that can be utilized to compare with the forward calculations. The results are shown in Figs.25(a)-(e).

II) Use a fixed true reflectivity value, as was the case in the VM model, which matches the literature values, i.e. 0.31. Sato has reported that the true reflectivity of silicon, which is a direct function of the dielectric constant of the material, is 0.3 and that it increases to 0.32 above the opacity of silicon. In order to avoid changing this value, an average of the two numbers has been chosen. This matches the value extracted from Li's data of n at 388°C, i.e., 0.308 [58].

III) A large range of the absorption coefficient α, 0.5-15cm^{-1}, has been chosen for the calculations. This choice represents a reasonable range for a lightly doped sample for the range of temperatures considered.

IV) A Mathcad program which consists of equations (3.8) and (3.9) as function of one-parameter αt, with t as the actual thickness of the wafer = 0.065cm, is implemented resulting in Fig.26.

V) Apparent reflectivity and transmissivity at 388°C, 6000cm^{-1} for the smooth and rough sides incidences using Fig.20(b) are extracted and plotted on Fig.26. The corresponding values of αt are determined in Fig.26 and listed in Table 5.1.

Table 5.1 Results of a one-parameter model in matching the experimental data in Figure 20(b) for 1.67μm

	Rough	α (cm^{-1})	(α × thickness)	Smooth	α (cm^{-1})	(α × thickness)
Transmissivity	0.3	7.65	0.497	0.47	1.45	0.094
Reflectivity	0.41	3.45	0.224	0.43	2.1	0.1365

From this table, it is seen that for the rough surface incidence, the values of αt that will yield the experimental transmissivity does not match the one that yield the experimental reflectivity. This means that the one-parameter model cannot predict the behavior of a rough surface optically. In the light of the discussion following Figs.19 and 20, this is perfectly clear since the dominant factor in the additional absorption is the increased effective light path that was caused by the roughness. The results of the smooth side incidence, on the other hand, have shown a somewhat better match both in α and the dimensionless parameter αt.

In order to test further the applicability of the model on the smooth side incidence, the comparison has been extended to more wavelengths, 1.42, 3.4 and 5μm. Table 5.2 lists the results of reflectance and transmittance extracted from Figs.20(b) for the wavelengths cited above. From the table, it is very clear that for λ<1.67μm, i.e. 1.42μm, and for smooth side incidence, a perfect agreement is achieved for αt. For longer wavelengths,

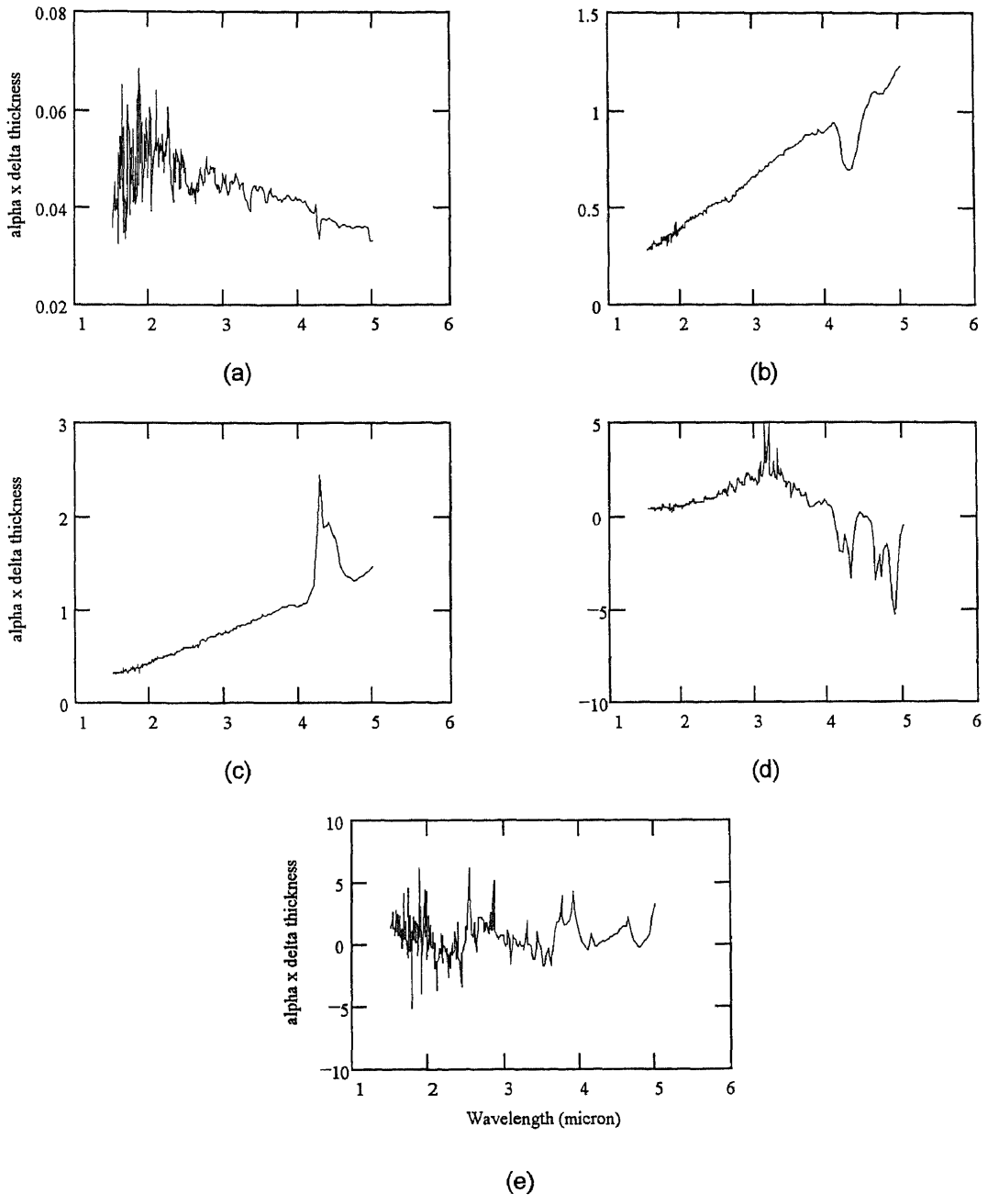

Fig.25 Product of the difference in effective light path between the front and back side times the absorption coefficient for five different temperatures: (a) 45,40 (b) 387,388 (c) 487,477 (d) 599,577 (e) 592,684°C for smooth and rough, respectively

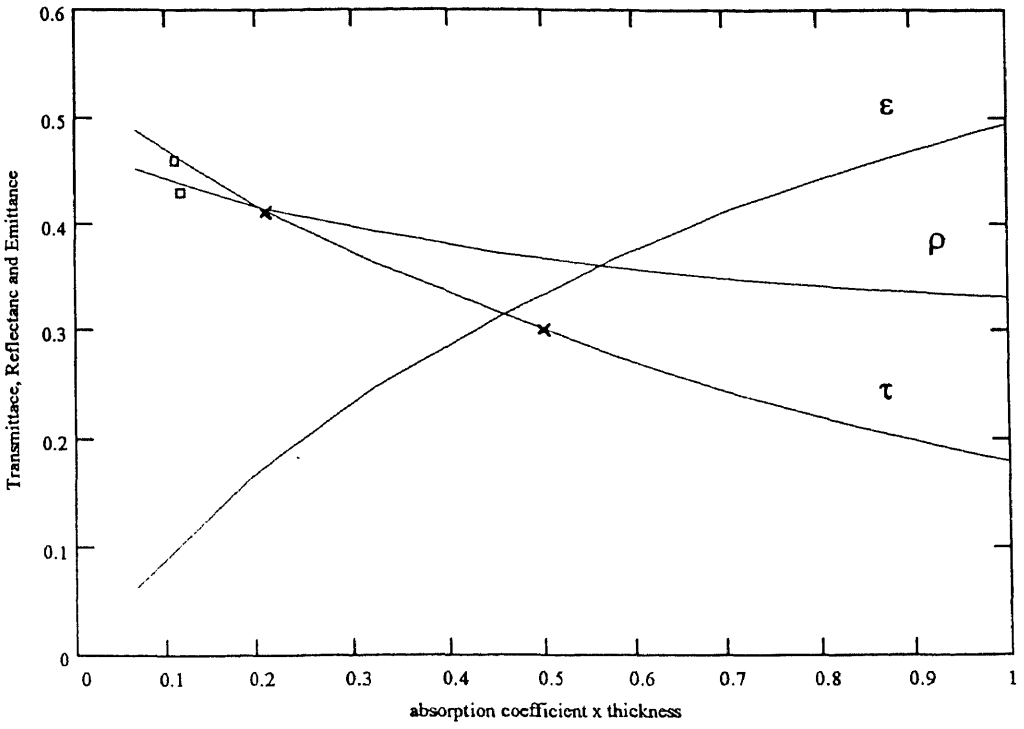

Fig.26 Transmittance, reflectance and emittance of a silicon sample 0.065cm thick as a function of absorption coefficient × thickness or the dimensionless parameter

Table 5.2 Results of a one-parameter model in matching the experimental data in Figure.20(b) for 1.42, 3.4 and 5μm. T for transmissivity and R for reflectivity.

	Rough	α (cm^{-1})	(α × thickness)	Smooth	α (cm^{-1})	(α × thickness)
T(1.42μm)	0.3001	7.5	0.4875	0.459	1.79	0.11635
R(1.42μm)	0.419	2.95	0.19175	0.43656	1.79	0.11635
T(3.4μm)	0.167	16.35	1.06275	0.4546	1.9	0.1235
R(3.4μm)	0.3511	10	1.65	0.397	4.5	0.2925
T(5μm)	0.0934	25.1	1.6315	0.4365	2.45	0.15925
R(5μm)	0.3291	16	1.04	0.3899	5.2	0.338

however, no single value parameter is found to give the experimental reflectance and transmittance data. It is also noticed that the discrepancy between the values of αt needed to simulate the experimental results increases further as the wavelength becomes longer. The smooth side incidence data reported in Table 5.2 are summarized in Fig.27. Fig.28 shows the αt values required to obtain the experimental reflectance and transmittance in Fig.20(b) as function of λ assuming a true reflectivity of 0.308. It is important to know that even though the model has worked out for short wavelengths such as 1.42μm when the light is incident on the smooth side, the emissivity of this sample is still much higher than a perfectly double-side polished sample with the same characteristics. As a matter of fact equation (5.8) does not allow the absorption coefficient at 388°C for such doping concentration as in this sample to exceed $0.4cm^{-1}$(α obtained from this model ~ $1.5cm^{-1}$). The difference is due to the multiple internal reflection causing a new effective thickness.

If a two-parameters model is applied to the single-side polished sample, utilizing the assumption that Eq. (3.4) is still applicable, different results will be obtained. In such

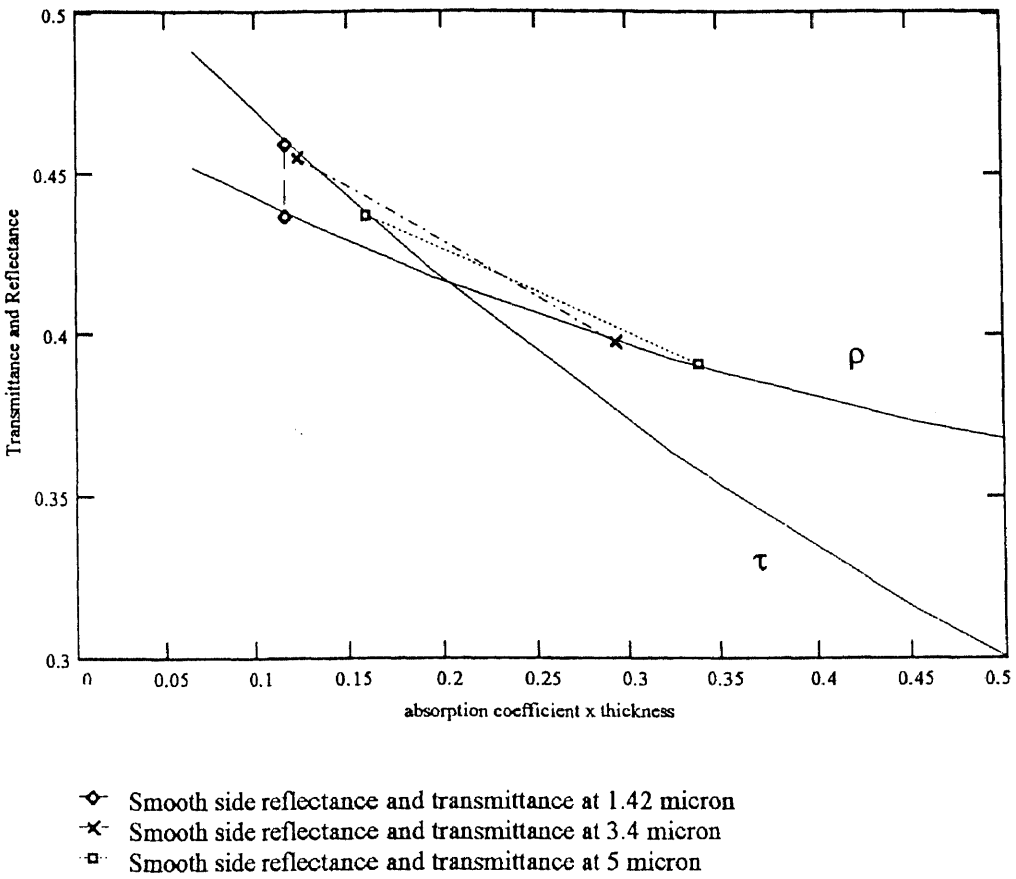

Fig.27 Smooth side incidence transmittance and reflectance measured data as function of αt for 1.42, 3.4 and 5μm

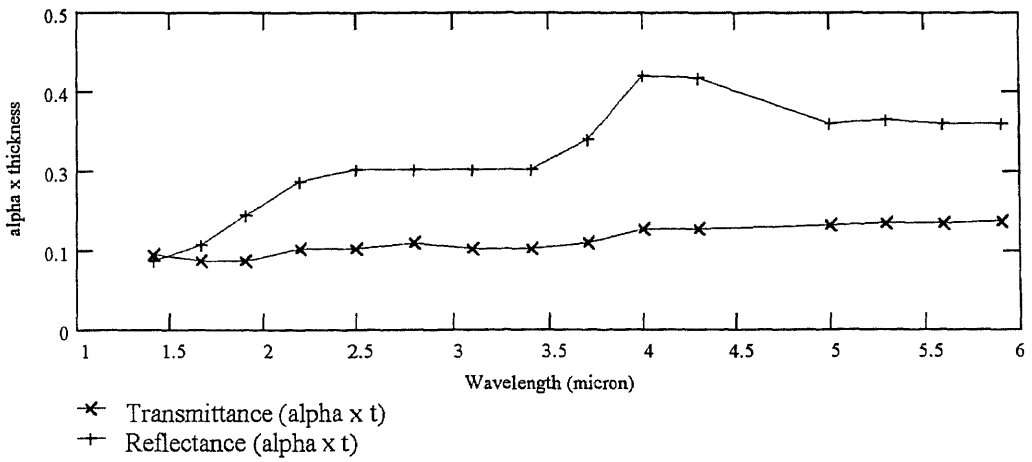

Fig.28 Comparison between the transmittance and reflectance dimensionless parameter αt for smooth side incidence as function of wavelength

a model, the absorption coefficient α is still the major contributor to the changes in the true transmissivity. The other parameter is the true reflectivity. Next, solving equations (3.8) and (3.9) for the true reflectivity and transmissivity, respectively yield:

$$\rho = \{(\tau^{*2}-\rho^{*2}+2\rho^{*}+1) \pm [\tau^{*2}(\tau^{*2}+2(-\rho^{*2}+(2\rho^{*}+1))) + (\rho^{*4}-1)^{4}]^{1/2}\}/\ 2(2-\rho^{*}) \qquad (5.10)$$

$$\tau = (\rho^{*}/\rho - 1) / \tau^{*} \qquad (5.11)$$

where ρ, ρ^{*}, τ and τ^{*} are the true and apparent reflectivity and transmissivity, respectively. Applying this two-parameter model to the rough incidence results of table 5.1 yields: $\rho = 1.7419 \pm 0.6531 / 3.18$, Taking first the (+) sign gives ($\rho = 0.7531$, $\tau = -1.5186$). This is non-physical where even if ρ is allowed to be 0.7531, τ cannot be negative. Allowing the (-) sign gives ($\rho = 0.3424$, $\tau = 0.6581$). Hence, the dimensionless parameter $\alpha t = 0.4184$. Since α does not change with changing the surface morphology, the same value works out good for the smooth side of the sample, i.e. $\sim 1.5 cm^{-1}$, the

effective thickness becomes ~ 0.2787cm. In this case one value of αt is achieved to obtain the true reflectivity and transmissivity for the rough side incidence. This might be an improvement over the results of the rough side incidence one-parameter model but on the account of the true reflectivity which has been never reported to exceed 0.32 for non-metallic non-degenerate silicon [28].

From the above discussions it is clear that the major reason a one-parameter model such as the VM model will fail, is the assumption that equation (3.4) applies for a single-side polished sample in the case of rough incidence. Stretching the model further by allowing a second parameter works out for the rough side incidence however, this will be on the account of the true reflectivity which is also rejected.

Surface roughness can be non-uniform and in some cases it is very difficult to simulate the surface by a simple textured geometry. But for a given batch of wafers, one wafer may represent the entire batch for process calibration. Thus, by taking micrographs, as in Figs.17 and 18, a general idea can be made about the degree and uniformity of roughness of the entire batch of wafers. Since the laws of optics still apply for a non-specular surface, this knowledge of the roughness can serve as a prototype to a model. Treatment of the light incident from all possible angles on such a surface can be considered. In such a treatment, all the rules that govern an ideal double-side polished sample, ray optics, diffraction theory, light trapping applies [22,67,68]. To quantify the theory, a Monte-Carlo type technique can be applied on a single ray which can be traced all the way until it either gets absorbed, transmitted or reflected by the sample. Next the ray is taken as a representative of all the other rays incident with the same angle. Given a

certain incident intensity, portions that are transmitted, reflected or absorbed are determined. This represents an ideal and simplified picture that does not show the degree of complexity that faces the industry in trying to model for such non-intrinsic feature. There exists a mathematical model by Sopori that attempts at determining the optical properties of non-specular silicon by utilizing optical ray tracing techniques to its full extent [69]. This model, PV-Optics, is the result of 8 years work and a budget of $500,000. In this model, surface morphology alone or combined with thin film layers can be treated in the range of 0.4-1μm. The model has been demonstrated on numerous occasions especially in the field of photovoltaics [69]. Attempts to extend the range of operations to near-mid IR range is being implemented at this time. One major obstacle is the lack of knowledge of bulk properties of silicon and other materials beyond opacity. It may be noted here that both NREL and NJIT are working closely to resolve this issue. One final obstacle that remains is the time budget for the simulation for a reasonably thick sample and the limited number of grooves that has different shapes. The end result is that until the RTP industry limits itself to double-side polished wafers, surface roughness will remain an obstacle especially if the temperature accuracy of $\pm 2°C$ per 3σ is required.

5.3 Sub-Bandgap Absorption:

Free Carriers and Doping Type Effects on Emissivity

The importance of emissivity due to non-contact temperature measurement techniques such as pyrometry and RTP has been established in chapter 4. The choice of the RTP

industry as it applies to silicon processing has focused on 5 wavelengths for pyrometer operation. These wavelengths are: 0.95, 2.5, 2.7, 3.3 and 4.5μm. Except for 0.95μm, all these wavelengths fall in the free carrier absorption domain. Therefore the understanding of this absorption mechanism is critical to obtain accurate results of the absorption coefficient and hence emissivity and other radiative properties. Equation (5.5) describes the wavelength and bulk property dependence of the absorption coefficient due to free carriers. This equation has been derived from Drude's classical free electron theory [70]. This section is devoted to the understanding of free carrier absorption mechanism, its dependence on material parameters, survey of the literature and the accuracy of the simulated results.

5.3.1 Drude Model

The Drude model has been described in detail in many standard solid state physics text books such as Ashcroft & Mermin [70] and Hummel [71], to name a few. In this section, only a brief description of the theory is addressed with the main focus being the mathematical aspect of the model. Three years after the discovery of the electron by Thomson, Drude established his famous free electron model on metals by applying the kinetic theory of gases. Later it was extended to include semiconductors. In this theory, the molecules of the gas are considered as solid spheres that move in straight lines until they collide with other molecules or boundaries. The negatively charged electrons represent these molecules whereas the positive charge is attached to much heavier particles which Drude considered immobile. In other words, each single metallic atom has

a charge = eZ, where e is the electron charge = 1.6×10^{-19}C and Z is the atomic number. Only a few of the electrons in each atom are loose enough to cause chemical reactions and to be labeled conduction electrons while the rest remain tightly bound to the positive nucleus. The basic assumptions of the model are as follows:

1) Interaction with ions and other electrons are neglected between collisions.

2) Major scattering mechanism is the heavy positive ions or nucleus.

3) Probability of collision for an electron per unit time is $1/\tau$, where τ is the time between two collisions.

4) Thermodynamic equilibrium is maintained during collisions, i.e. after every collision the electron velocity emerges with a new and random velocity and direction.

Based on these assumptions and through the well known Maxwell's equations a mathematical formula for the absorption due to free electrons is deduced:

Ohms law states that

$$V = IR \tag{5.12}$$

where V is the potential drop along a wire with resistance R and a passing current I. The electric field

$$E = \rho j \tag{5.13}$$

where ρ is the resistivity and j is the current density.

$$j = I/A \tag{5.14}$$

where I is the current and A is the cross sectional area. If L is the length of the wire, then $V = EL$ implies that $V = I\rho L/A$. Hence the resistance of the wire $R = \rho L/A$. Since every electron carries a charge -e, the charge crossing A in time dt will be -NevAdt, hence the

current density is:

$$j = -Nev \tag{5.15}$$

where N is the number of carriers and v is the average velocity of each electron. Momentum

$$p = -eE \tag{5.16}$$

where the negative sign is for the electron charge. Thus, the new average velocity after each collision is

$$v_{avg} = p\tau/m = -eEt/m \tag{5.17}$$

$$j = -Nev \times -eEt/m = (Ne^2\tau/m)E \tag{5.18}$$

If $\sigma = 1/\rho$, where σ is the conductivity, then equation (5.13) becomes $j = \sigma E$. Thus,

$$\sigma_o = (Ne^2\tau/m) \tag{5.19}$$

where σ_o is the conductivity at zero frequency. Maxwell's equations states (Gaussian units):

$$\nabla \times E = -1/c(\partial H/\partial t) \tag{5.20}$$

where E is electric field, c is the speed of light in vacuum and H is the magnetic field.

$$\nabla \times H = 4\pi j/c + \varepsilon/c(\partial E/\partial t) \tag{5.21}$$

where e is the dielectric constant. Now if $E = E(r)e^{-i\omega t}$, and $H = H(r)e^{-i\omega t}$, where E(r) and H(r) represent the position functions and the exponential components represent the time dependent functions, then by substituting them into (5.20) and (5.21) yield,

$$\nabla \times H = (4\pi\sigma/c)E + \varepsilon/c(-i\omega)E = \nabla \times H = 1/c(4\pi\sigma - i\omega\varepsilon)E \tag{5.22}$$

$$\nabla \times \varepsilon = -i\omega/cH \tag{5.23}$$

rearranging (5.23) gives $H = -ic/\omega(\nabla \times \varepsilon)$. Then, by substituting this back into (5.11) gives

$$-ic/\omega \nabla\times\nabla\times\varepsilon = 1/c(4\pi\sigma - i\omega\varepsilon)E \quad (5.24)$$

But $\nabla\times\nabla\times\varepsilon = \nabla(\nabla.E) - \nabla^2E$, and $\nabla.E = 0$, leading to

$$ic/\omega\nabla^2E - 1/c(4\pi\sigma - i\omega\varepsilon)E = 0 \quad (5.25)$$

$$\nabla^2E + i\omega/c^2(4\pi\sigma - i\omega\varepsilon)E = 0 \quad (5.26)$$

$$\nabla^2E - \omega^2/c^2(4\pi i\sigma/\omega + \varepsilon)E = 0 \quad (5.27)$$

If $E = E(r)$ is expressed exponentially as $E = E_oe^{\pm iK\cdot r}$, where $\pm$ means that the motion is in either ways towards or opposite to the original direction and K is the wave vector, then upon substituting in (5.27),

$$K^2 = \omega^2/c^2\,[4\pi i\sigma/\omega + \varepsilon] \quad (5.28)$$

So if $K^2 = \omega^2/c^2\varepsilon(\omega)$, where $\varepsilon(\omega)$ is the complex dielectric constant, then

$$\varepsilon(\omega) = \varepsilon[1 + 4\pi i\sigma/\varepsilon\omega] \quad (5.29)$$

Let $(\varepsilon(\omega))^{1/2} = n + ik$, where $(\varepsilon(\omega))^{1/2}$ is the complex refractive index, n is the real refractive index and k is the extinction coefficient, then $Re[\varepsilon(\omega)] = n^2 - k^2$, and $Im[\varepsilon(\omega)] = 2nk$. To get σ as function of frequency, substitute $p(t) = p(\omega)e^{-i\omega t}$ in the equation of motion, i.e. $dp/dt = -p/t - eE$. The result is

$$-i\omega p(\omega) = -p(\omega)/t - eE(\omega) \quad (5.30)$$

By rearranging (5.30), $p(\omega) = -eE/(1/\tau - i\omega)$. Then by substituting in $j = -Nep/m$

$$j = (-Ne/m)[-e/(1/\tau - i\omega)]E \quad (5.31)$$

Thus, $\sigma(\omega) = (Ne^2\tau/m)/(1 - i\omega\tau) = \sigma_o/(1 - i\omega\tau) = \sigma_o(1 - i\omega\tau)/(1 + \omega^2\tau^2)$. Substituting this value of σ into (5.29) yields:

$$\varepsilon(\omega) = \varepsilon[1 + (4\pi i/\varepsilon\omega)(\sigma_o(1 - i\omega\tau)/(1 + \omega^2\tau^2)] \quad (5.32)$$

Define a plasma frequency $\omega_p^2 = 4\pi ne^2/\varepsilon m$. Then (5.32) becomes $\varepsilon(\omega) = \varepsilon[1 + (\omega_p^2/\omega)\tau(i + \omega\tau)/(1 + \omega^2\tau^2)]$. Thus,

$$\mathrm{Re}[\varepsilon(\omega)] = n^2 - k^2 = \varepsilon[1 + \omega_p^2\tau^2/(1 + \omega^2\tau^2) \tag{5.33}$$

$$\mathrm{Im}[\varepsilon(\omega)] = 2nk = \varepsilon\omega_p^2\tau/\omega[1/(1 + \omega^2\tau^2)] \tag{5.34}$$

In the High frequency regime, i.e. near-mid IR, which covers the free carrier range, $\omega^2\tau^2 >> 1$ implies that

$$n^2 - k^2 = \varepsilon[1 + (\omega_p/\omega)^2] \tag{5.35}$$

$$2nk = \varepsilon\omega_p^2/\omega^3\tau \tag{5.36}$$

As $2nk << 1$ for the range of wavelengths considered here, and since $n^2 \approx \varepsilon + k^2$,

$\therefore k^2 << 1$, and $n^2 \approx \varepsilon$. Hence,

$$k = \varepsilon\omega_p^2/(2n\omega^3\tau) \; (\; n\omega_p^2/(2\omega^3\tau) \tag{5.37}$$

Since the extinction coefficient k is related to the absorption coefficient α by

$$\alpha = 2(\omega/c)\, k \tag{5.38}$$

Then by substituting the value of k we get,

$$\alpha = 2(\omega/c)n\omega_p^2/(2\omega^3\tau) = n/c\tau(\omega_p/\omega)^2 \tag{5.39}$$

By substituting for ω_p and ω in (5.39), α takes the form of equation (5.5) but in Gaussian units. In order to transform the result into SI units, $\sigma \rightarrow \sigma/4\pi\varepsilon_o$ yielding (5.5). Equation (5.5) shows that α for silicon will depend on the following parameters: i) total number of free carriers both by impurities and thermal generation, ii) refractive index and hence the dielectric constant, iii) conductivity effective mass m* of the carriers electron or hole, iv) wavelength and v) scattering or collision time. For silicon the temperature dependent

refractive index $dn/dT \sim 10^{-4}$ /°C [56]. The total number of free carriers can be determined to a high accuracy and up to high temperatures. Since RTP applications are usually above 300°C, all the impurities are activated and the thermally generated electron-hole pairs can be calculated using the standard equation [72]

$$n = p = 3.73 \times 10^{16} T^{3/2} \exp(-7014/T) \qquad (5.40)$$

where T is the absolute temperature in Kelvin. This equation has been utilized in many models that aim at determining the free carrier contribution to α. The only problem is that Eq. (5.40) depends on the density of state effective masses values for the carriers which are not known in the literature above 700K. The effect of change in density of state mass on the total number of carriers is yet negligible. The conductivity effective mass for electrons has been found to be $0.26m_o$, where m_o is the free electron mass = 9.1×10^{-31}kg. This value utilizes the longitudinal and transverse masses of electron, assuming ellipsoidal energy band shape, as has been measured by Hensel et al. [73]. The hole conductivity effective mass, on the other hand, depends on the temperature due to non-parabolicity in the hole bands. Models such as the MIT/SEMATECH model, use $0.34m_o$ or the band edge hole mass. This value is valid only at low temperatures, i.e. < 20K. Further, at intrinsic temperatures, the holes and electrons are equal in number making the hole effective conductivity mass a very important parameter for both n and p-Si. Thus, the real m_c^* can be a major source of error in determining α. This error can range from 2 to 3 times the value obtained using $0.34m_o$. α is proportional to λ^2 and is easily predictable according to equation (5.5). Finally, the scattering time (i.e. mobility $\mu = e\tau/m^*$) plays a major role in determining the free carrier absorption. Most of the data available in the literature are for

the DC-mobility and there is no a priori reason to expect these results to be applicable at optical frequencies [62]. A comparison of the absorption coefficient α obtained from the DC-mobility data with α extracted from recent IR transmission data [63,75] reveals discrepancies as has reported by Hebb [76]. The difference noticed could be because the DC-mobility is not the same as the optical mobility in the IR photon absorption.

5.3.2 Free Carrier Absorption Coefficient - A Literature Survey

Free carrier absorption in silicon has been studied extensively in the literature. In this section, a brief summary of the findings of some of these studies is presented.

Spitzer and Fan have conducted one of the most extensive early studies on the IR absorption in n-Si in the wavelength range of 1-45 μm [77]. Their study includes different doping types: As, Sb and P and a range of doping concentration from 1.4×10^{16}-$10^{19}cm^{-3}$ as shown in table 5.3.

Table 5.3 List of samples, doping concentration and room temperature carrier concentrations [77]

Sample No.	Donor Impurity	$N_{300K}(cm^{-3})$	$N_{doping}(cm^{-3})$
1	arsenic	1.4×10^{16}	-
2	antimony	8.0×10^{16}	0.95×10^{17}
3	antimony	1.7×10^{17}	5.5×10^{17}
4	phosphorous	3.2×10^{17}	1.26×10^{18}
5	arsenic tin alloy	6.1×10^{18}	4.6×10^{19}
6	arsenic	1.0×10^{19}	6.6×10^{19}

The results of the absorption coefficient as function of wavelength are shown in Fig.29. The figure shows the major absorption mechanisms in the near-mid IR, i.e. absorption edge, free carriers, and lattice vibration or phonons. From the figure, it is clear that samples #4, 5 and 6 behave according to equation (5.5), i.e. $\alpha \propto \lambda^2$, but only for $\lambda >$ 4μm. Samples #1,2 and 3 do not show this behavior clearly because of the strong phonon absorption that masks the free carrier absorption. From Table 5.3, it is clear that for samples 4-6, the available free carriers at room temperature is $> 3\times10^{17}cm^{-3}$ while the other samples have fewer free carriers. At high carrier concentrations the free carrier absorption becomes dominant over the phonon contribution and thus behaves according to (5.5) while at low carrier concentrations the phonon absorption becomes dominant and hence increases faster than λ^2. An interesting phenomenon that Spitzer and Fan [77] have observed in this study is the absorption band that appears between 1-5μm for n-Si and that not been seen for p-Si. In Fig.29, this band appears in the shape of a hump and adds to the λ^2 free carrier absorption expected. Spitzer and Fan have attributed this band to a possible conduction intraband absorption, i.e. electron transitions from a conduction band minima to a higher band. They have identified the peak of this band is around 2.3μm. Later, Hensel et al. [73] reported that energy gap between the conduction minima and next higher band is ~0.5eV, which corresponds to ~2.4μm. Thus, the absorption band that appears in Fig.29 is indeed the result of a conduction intraband transition of electrons which adds to the free carriers contribution and rises faster than λ^2. Sato [28] has also performed a similar study of the free carrier absorption as function of wavelength and temperature. Figs.30(a) and 30(b) show Sato's results on an n-Si, doping concentration

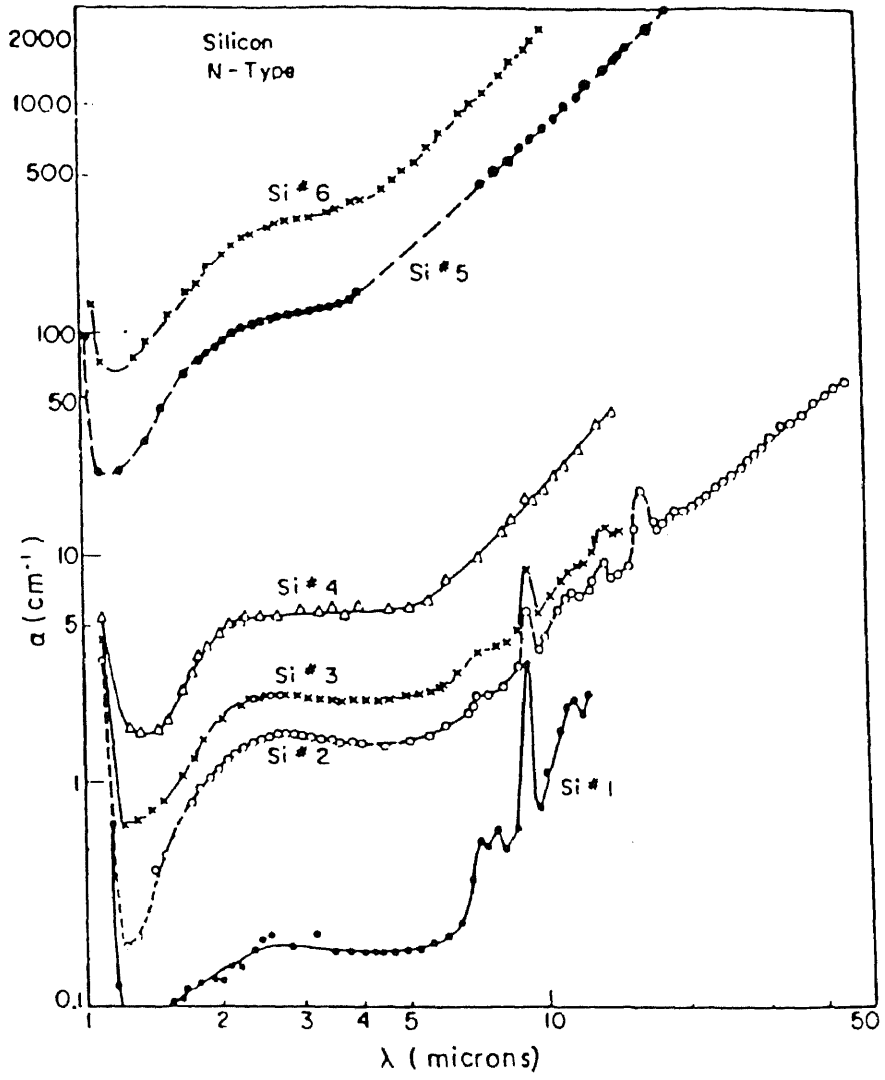

Fig.29 Room temperature absorption coefficient as function of wavelength for: #1) $1.4\times10^{16}cm^{-3}$, As doped, #2) $8\times10^{16}cm^{-3}$, Sb doped, #3) $1.7\times10^{17}cm^{-3}$, Sb doped, #4) $3.2\times10^{17}cm^{-3}$, P doped, #5) $6.1\times10^{18}cm^{-3}$, arsenic tin alloy, and #6) $1\times10^{19}cm^{-3}$ As doped samples [77]

~$2.4\times10^{14}cm^{-3}$. It has been shown from these figures that the free carrier absorption has a λ^2 dependence for $\lambda > 3\mu m$. Sato did not cover the region of the 2.3μm absorption band observed by Spitzer and Fan. Recent studies on n-Si by Vandenabeele et al. [63], Timans [78] and n and p-Si by Sturm and Reaves [75] aimed at understanding the free carrier absorption as function of temperature, have resulted in a numerical model [63] and first-principles model [75,78] for the absorption coefficient. These studies have been performed at a limited number of specific wavelengths: Vandenabeele and Maex have conducted their study at 1.7 and 3.4μm, Timans at 1.15-1.55μm, and Sturm and Reaves at 1.3 and 1.55μm. Thus, the sparseness of the data from these studies for free carrier absorption does not permit a general picture to be constructed for α and ε over the range of 1-5μm and beyond. They may, however, yield adequate results above 650°C because a) the free carrier absorption may tend to mask the electron intraband absorption and b) the emissivity of silicon saturates at such temperatures and small errors in α do not matter any more. Another approach is to calculate the free carrier absorption from equation (5.5) using the present knowledge of the parameters involved in this equation, namely refractive index, scattering time (or mobility), and conductivity effective mass. This has resulted in the Multi-Rad model and a model suggested by Wood et al. [79]. The Multi-Rad model has used the lattice scattering formula by Morin and Maita [80]

$$\mu_l = \mu_o (T/300)^{-\alpha} \tag{5.41}$$

where $\mu_l = \mu_o = 1440cm^2/Vs$ for electrons and $480cm^2/Vs$ for holes at 300K [81], and the exponent α is chosen to fit the transport data in the literature. The model due to Wood et al. has utilized exclusively the DC-mobility data available both due to lattice scattering

(5.41), with $\alpha = 2.2$ for both carrier types, and impurity scattering [82,83]

$$\mu_i = c_d T^{1.5}/XN_d \tag{5.42}$$

$$X = \ln(1 + c_b T^2/n) - c_b T^2/(n + c_b T^2) \tag{5.43}$$

where N_d represents the concentration of ionized impurities and n is the carrier density (either electrons or holes). Then the net carrier mobility μ is modeled as [84]

$$\mu = \mu_l[\{1.025/(1 + (Y/1.68)^{1.43})\} - 0.025] \tag{5.44}$$

$$Y = (6\mu_l/\mu_i)^{1/2} \tag{5.45}$$

where the empirical constant c_d is $10^{17}cm^{-1}V^{-1}s^{-1}K^{-3/2}$ for holes and $4.61\times10^{17}cm^{-1}V^{-1}s^{-1}K^{-3/2}$ for electrons, c_b is $6.25\times10^{14}cm^{-3}K^{-2}$ for holes and $1.52\times10^{15}cm^{-3}K^{-2}$ for electrons, N_d is the dopant concentration (cm^{-3}). The final mobility μ is then substituted into equation (5.5) along with the other parameters to obtain the absorption coefficient and the radiative properties. This model is expected to have a higher percentage of error than the Multi-Rad model because it depends solely on the DC-mobility mentioned above without fitting it with the experimental data reported for α and modifying it accordingly as the Multi-Rad model. Carrier mobilities have also been determined from thermal conductivity data [85,86]. Other studies are aimed at measuring or predicting the minority carrier mobility [87-90], carrier mobilities due to impurity scattering [91-95] and modeling for mobility in general [96-101]. Any difference in simulated and measured α's are due to possible differences in DC-mobility and optical mobility [76]. The following section will discuss some of the discrepancies between the measured and the simulated α using the Multi-Rad model.

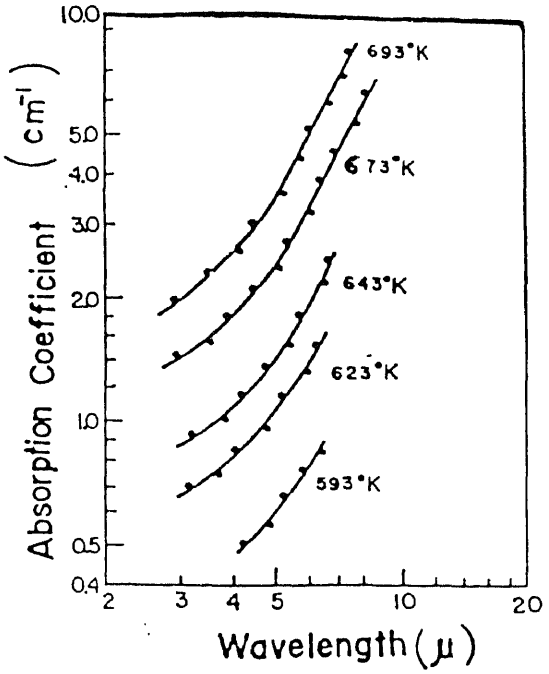

Fig.30(a) Spectral dependence of the absorption coefficient due to free carriers for n-Si, ~$3\times10^{14}cm^{-3}$, 1.77mm thick sample [28]

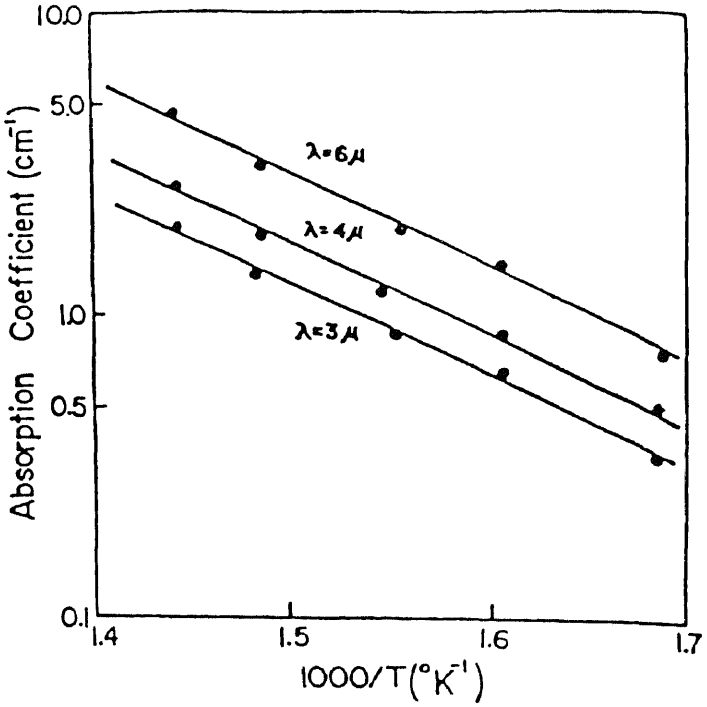

Fig.30(b) Temperature dependence of the absorption due to free carriers for n-Si, ~$3\times10^{14}cm^{-3}$, 1.77mm thick sample [28]

5.3.3 Comparison Between Measured and Simulated α Using Multi-Rad

In this section a comparison of the experimentally measured absorption coefficient of silicon from the literature with the simulated values for the same doping, temperature, and wavelength is presented. Figs.31(a)-31(c) show the comparison of measured α values by Spitzer and Fan [77] with those simulated by Multi-Rad for n-Si with three different doping: a) 1.4×10^{16}, b) 8×10^{16} and c) $3.2\times10^{17}cm^{-3}$ or samples #1, 2 and 4, respectively, at room temperature. The figures show clearly that the model data does not take into account the intraband conduction transition mentioned in the previous section; it does rather use a λ^2 dependence that rises smoothly as function of wavelength. In Fig.31(c) the spectrum range has been increased to include $\lambda > 6\mu m$ because for this sample in particular the phonon contribution to α has been overshadowed or masked by the free carrier contribution as can be seen in Fig.29. Thus, a comparison between the measured and simulated data can be made even in the phonon regime. It can be seen from the figures that the disagreement does not end at 4μm at which the free carrier absorption becomes dominant. The simulated α exceeds the measured α for $\lambda > 4\mu m$ in Figs.31(a)-31(c), with Fig.31(c) having the largest difference by a factor of at least 2. This means that either λ^2 dependence is not very clear for the room temperature data or that the available parameters utilized by the model in equation (5.5) are not valid. In Figs.32(a)-(e), another comparison is made between the α measured by Sato [28] and the Multi-Rad simulation for n-Si, $2.9\times10^{13}cm^{-3}$ at: a) 593, b) 623, c) 643, d) 673 and e) 693K. Sato's measurements did not cover the intraband conduction transition which peaks at 2.3μm resulting in less disagreement with the model. The comparison proves again that even

though a λ^2 behavior is shown by the temperature dependent data, the magnitude of the model values are still 1.5 times the measured data. This is an improvement over the larger discrepancy seen in Fig.31(c) and can be explained by taking into account the increasing lattice scattering as a function of temperature. The model may have underestimated the lattice scattering mechanism assuming smaller change in τ with temperature resulting in less differences between α's. Figs.33(a)-33(f) show a similar comparison between the data measured by Timans [78] and those simulated by Multi-Rad for n-Si, $5.5\times10^{13}cm^{-3}$ at: a) 430, b) 450, c) 500, d) 525, e) 555 and f) 600°C. In his study Timans has covered a narrow band of wavelengths ranging from 1.15-1.55μm where absorption, dominated by band edge absorption, can be rather accurately modeled. A comparison is made in Figs.34(a) and 34(b) between the three experimental results considered so far. Fig.34(a) presents the measured data of Timans at 703K, Spitzer and Fan at room temperature for 8×10^{16}, Sato at 693K. The thermally generated electron-hole pairs at 693K has been calculated to be $3.42\times10^{16}cm^{-3}$, which is almost equal to the number of the available free carriers in the sample investigated by Spitzer and Fan. Fig.34(a) shows the difference in α at the short wavelength end between the data of Spitzer and Fan [77] and Timans [78]. Similarly, a comparison is shown at longer wavelengths between data of Spitzer and Fan and data of Sato. The studies of Sato and Timans do not cover the intermediate wavelength range corresponding to the conduction intraband transition region. These discrepancies between data of Spitzer-Fan and other authors can be attributed to the fact that at higher temperatures, the lattice vibration scattering time τ decreases resulting in enhanced absorption, cf. Eq. (5.5). An attempt to simulate this effect by use of a sample

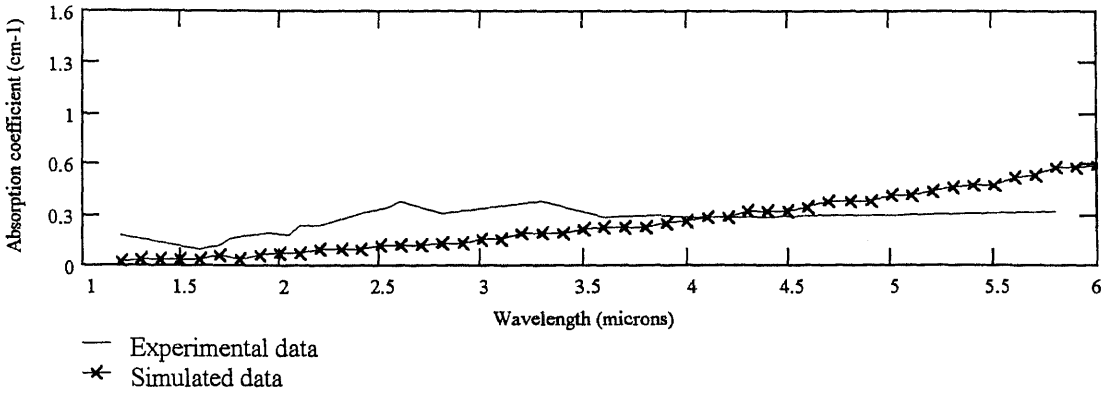

(a)

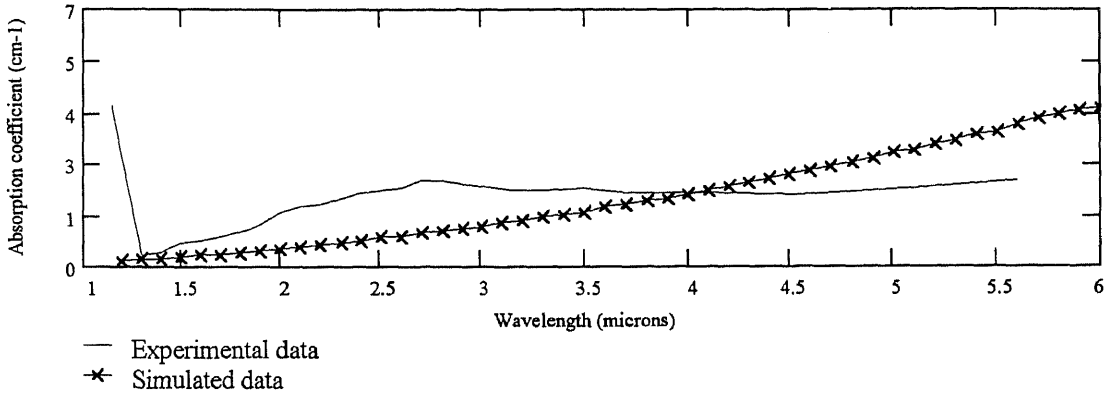

(b)

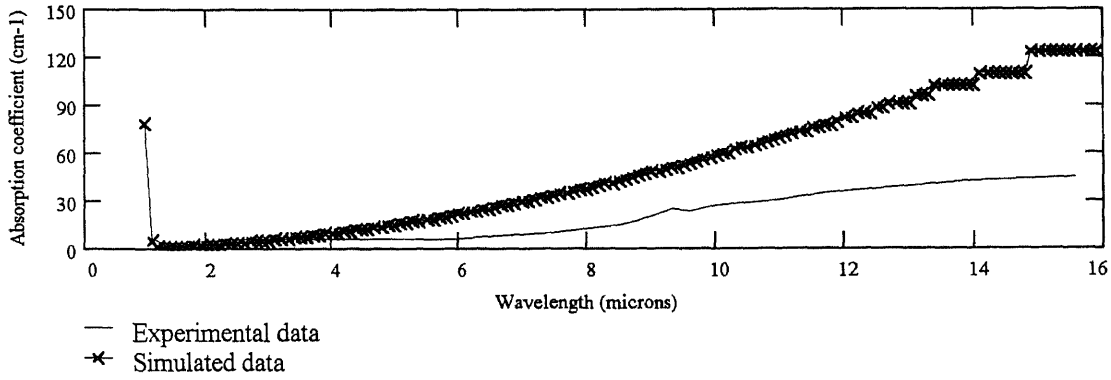

(c)

Fig.31 Comparison between the absorption coefficient values obtained experimentally by Spitzer and Fan with those obtained by simulation by Multi-Rad for n-Si: a) 1.4×10^{16}, b) 8×10^{16} and c) $3.2\times10^{17}cm^{-3}$ at room temperature

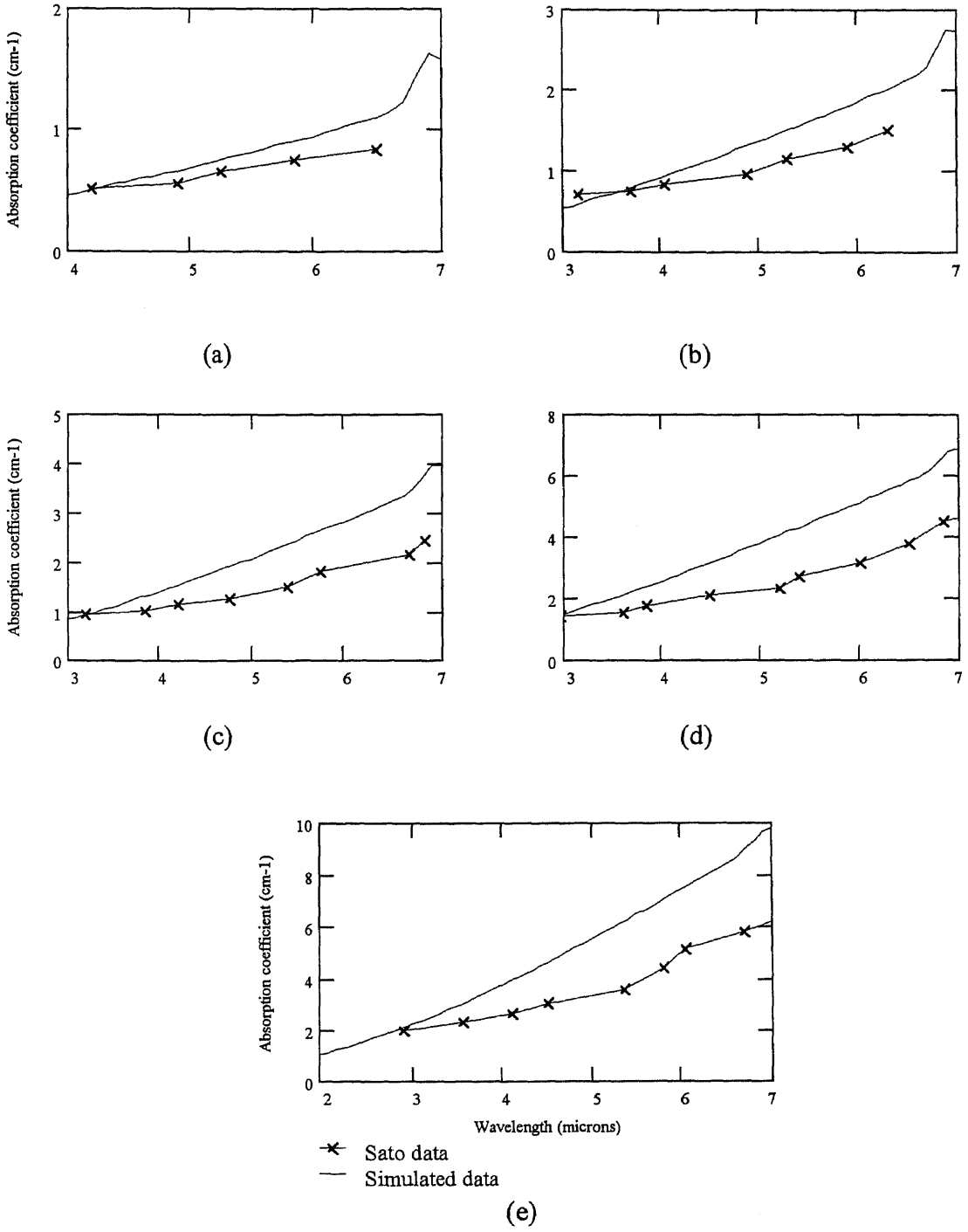

Fig.32 Comparison between the measured absorption coefficient by Sato and the simulated by Multi-Rad for n-Si, $2.9\times10^{14}cm^{-3}$ at: a) 593, b) 623, c) 673 and d) 693K

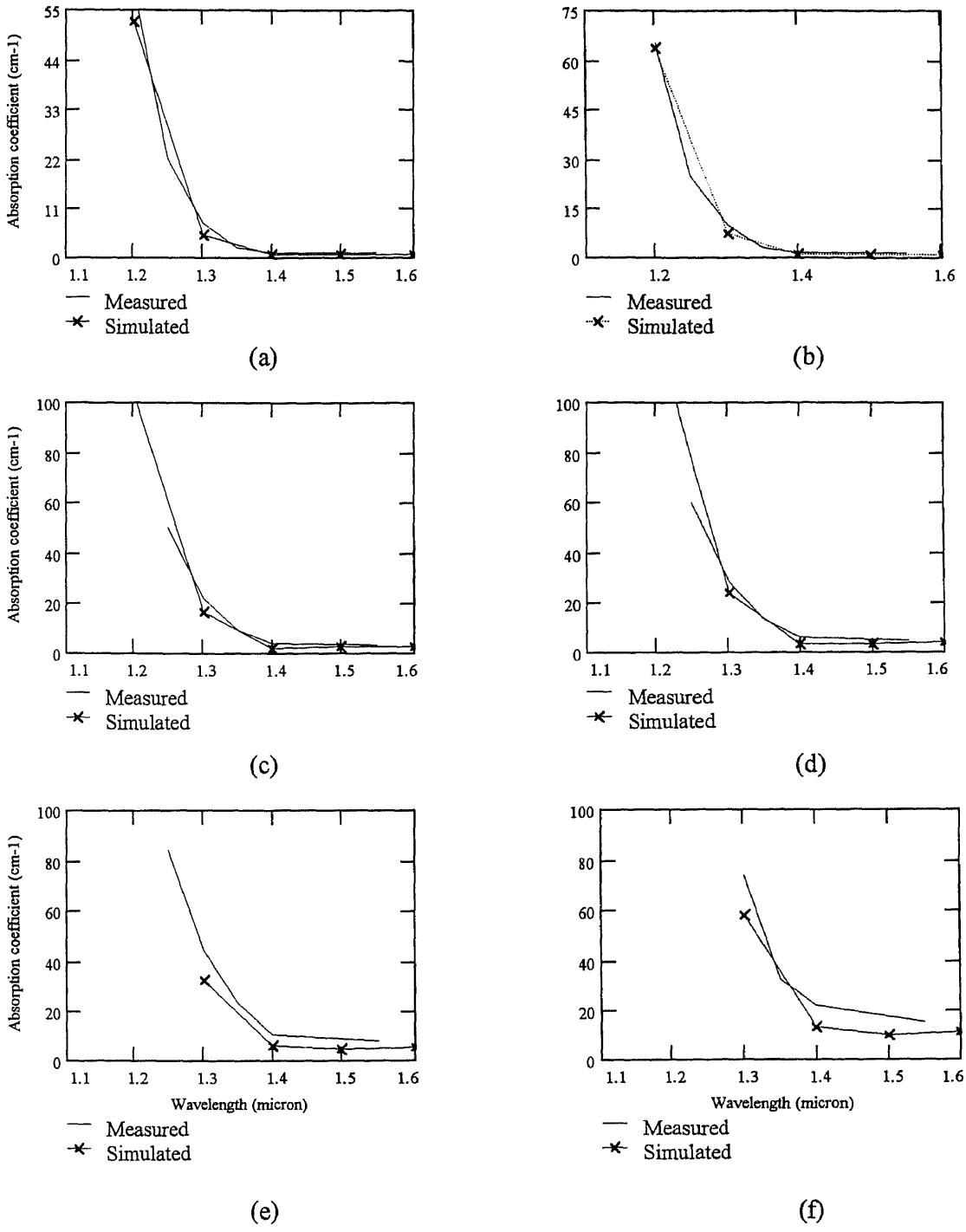

Fig.33 Comparison between the measured absorption coefficient by Timans and the simulated by Multi-Rad for n-Si, $5.5\times10^{13}cm^{-3}$ at: a) 430, b) 450, c) 500, d) 525, e) 555 and f) 600°C

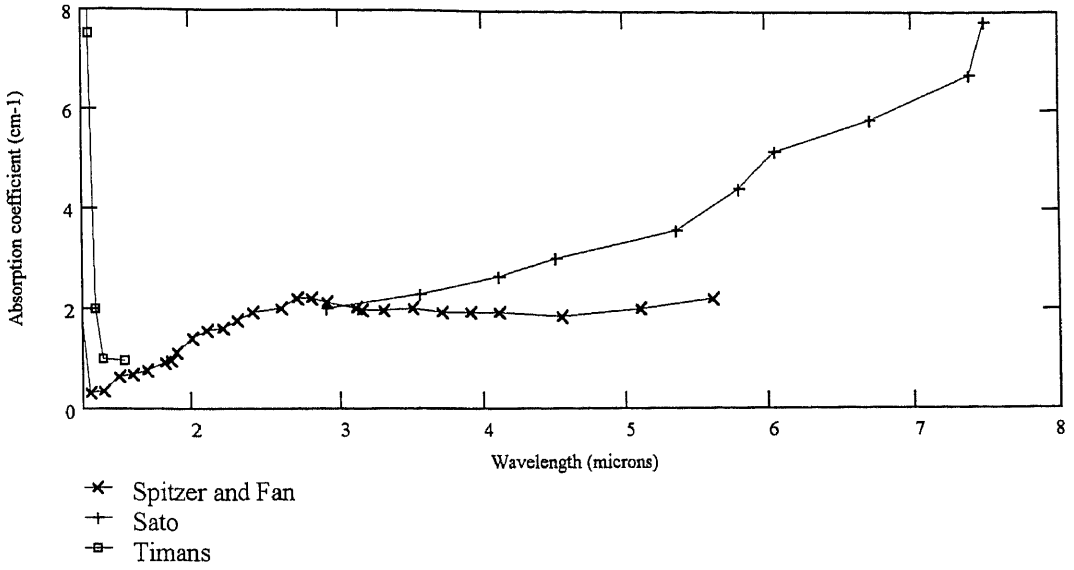

(a)

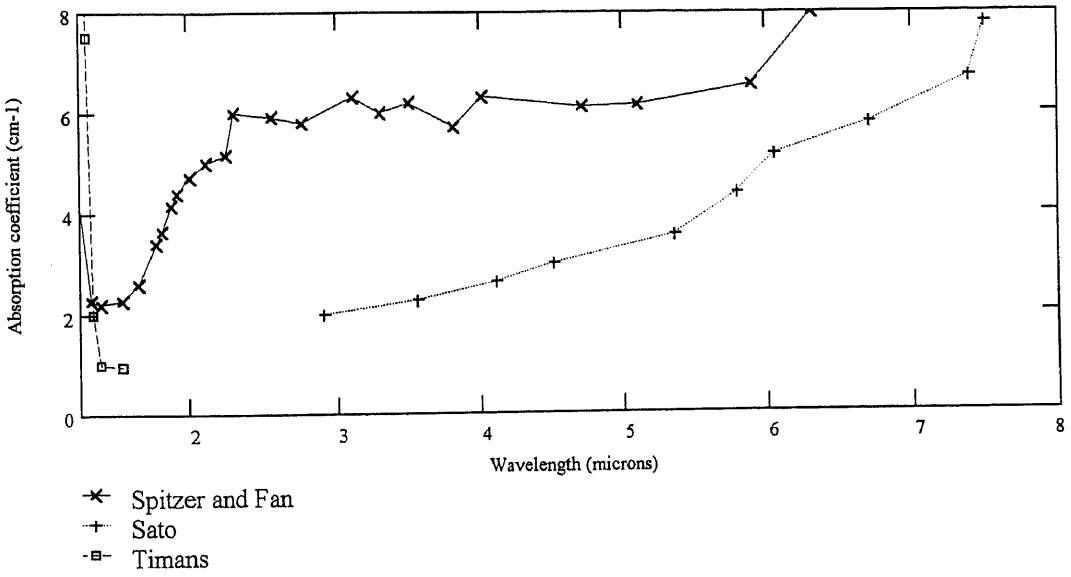

(b)

Fig.34 Comparison between the measured absorption coefficient data obtained by Spitzer and Fan, Sato, and Timans for: a) 300K ($8\times10^{16}cm^{-3}$), 693 and 703K, respectively; and b) 300K ($3.2\times10^{17}cm^{-3}$), 693 and 703K, respectively

with higher carrier concentration at T = 300K from Spitzer and Fan collection, $3.2\times10^{17}cm^{-3}$ or sample #4 is shown in Fig.34(b). In this figure, the disagreement between α's increases even further forcing one to conclude that it is hard to compare room and high temperature absorption coefficients. However, from the figure, it can be seen that if Sato data is extrapolated all the way to 1.6μm, i.e. to match Timans data, a good agreement can be found. This is because the two measurements have been performed at similar temperatures. In order to understand fully the current status of the modeling capabilities at the present time, a comparison is made for p-Si. Fig.35 shows this comparison with the data obtained by Sturm and Reaves for p-Si, $6\times10^{14}cm^{-3}$ at λ = 1.55μm as function of temperature [75]. As can be seen in the figure, the model does not agree with the measured data possibly because the data were obtained for a single-side polished sample.

We have measured the absorption coefficient of a double-side polished p-Si wafer, orientation <100>, 250μm thick, of doping concentration $7\times10^{14}cm^{-3}$. A comparison is made between our measured absorption coefficient and simulations done using Multi-Rad and the results are summarized in Figs.36(a)-(d). In Fig.36(a), the carrier concentration in this very thin sample is too low to give measurable α. For such low doping, measurements of α at or slightly above room temperature should be taken on thick samples, i.e. >1mm, similar to the measurements of Sato (t_{Sato}=1.77mm) [28]. One important result concluded from Fig.36 is that the extrinsic p-Si does not have an intraband transition similar to that found in n-Si. This has been commented on by Fan et al. [102]. Since the intraband transitions for the valence band are forbidden at k = 0, the transitions off k = 0 will only

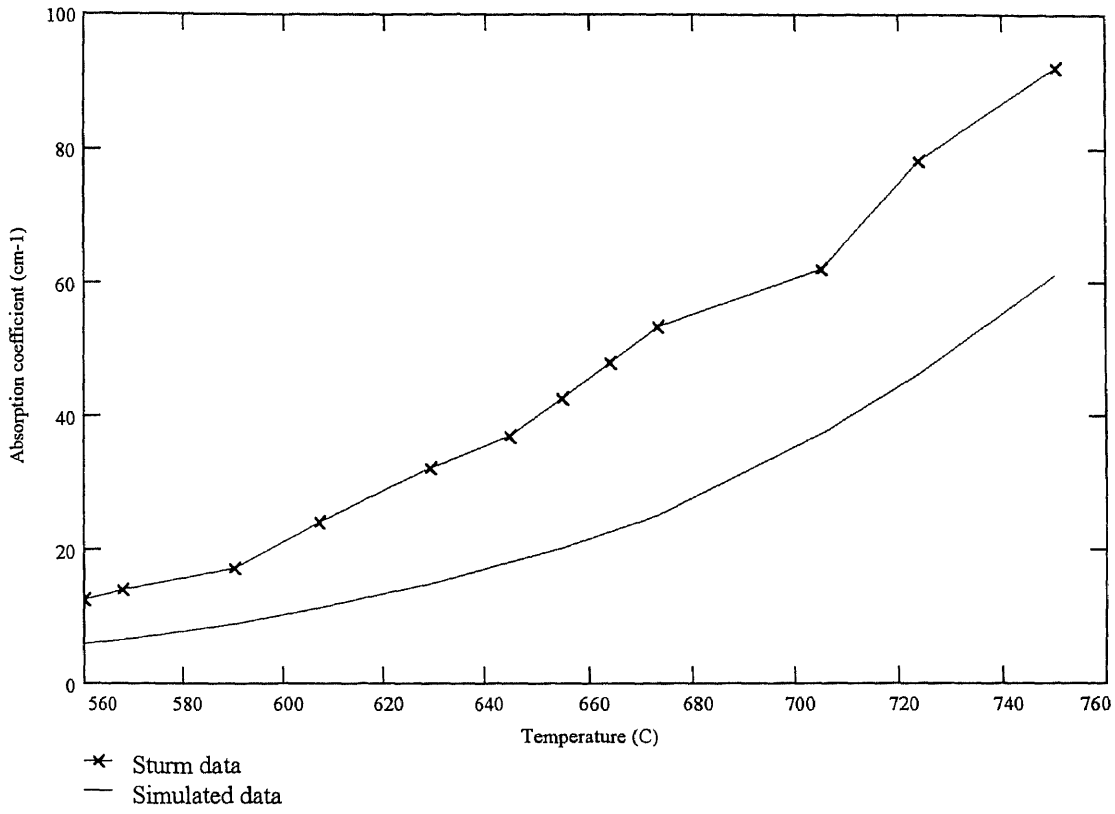

Fig.35 Comparison between the measured absorption coefficient by Sturm and Reaves and simulated by Multi-Rad for p-Si, $6\times10^{14}cm^{-3}$ at $\lambda = 1.55\mu m$

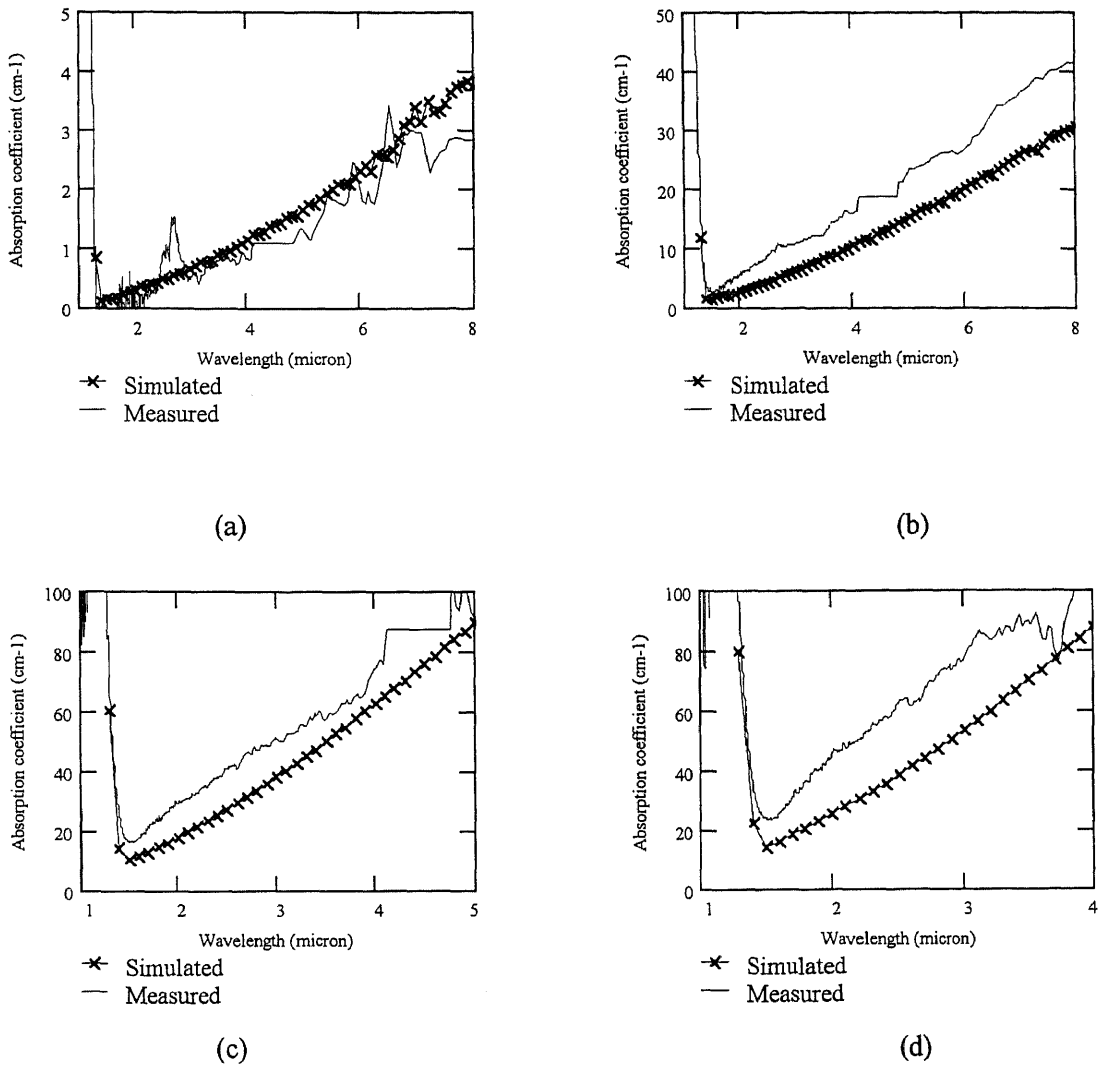

Fig.36 Comparison between the measured and simulated absorption coefficient for p-Si, $7\times10^{14}cm^{-3}$ for: a) 359, b) 479, c) 605 and d) 632°C

give rise to a very broad, featureless absorption band*. Thus, one would expect a broad background contribution to α but no discernible peak. To enhance the comparison of measured and simulated α we have removed the λ^2 dependence from plots in Fig.36 by replotting as α/λ^2. These results are presented in Fig.37. At temperature above 470°C the normalized data in Fig.37 show the 2.3μm absorption band much more clearly than in Fig.36 and reveals the same general feature as seen by Spitzer and Fan for n-Si. It has been reported by Fan et al. [102] for p-Si, at room temperature, that the absorption coefficient rises smoothly as λ^2 characteristic of free carrier absorption. As stated before, the p-Si used in the figure has a low doping concentration of $7\times10^{14}cm^{-3}$, so at temperatures corresponding to 479°C, the thermally generated free carriers exceed this number, in fact reaching $7.6\times10^{16}cm^{-3}$, causing the wafer to be in its intrinsic regime. In this case, there exist an equal number of electrons and holes. Thus, the band that arises and peaks around λ ~2.3μm is a result of conduction intraband transitions. To the best of our knowledge, this is the first time the observations of the 2.3μm absorption band as function of temperature is reported in the literature. As expected the intensity of the peak rises as function of temperature as seen from Figs.37(c) and 37(d) because of the increase in concentration of thermally generated electrons. The position of this absorption band is revealed to be essentially temperature independent consistent with its identification with the conduction band gap of ~0.5eV. The splitting of the conduction band as noted by Hensel et al. [73] is not expected to show a significant temperature dependence.

* J.C. Hensel, Physics Dept., NJIT, personal communication, Aug. 1998

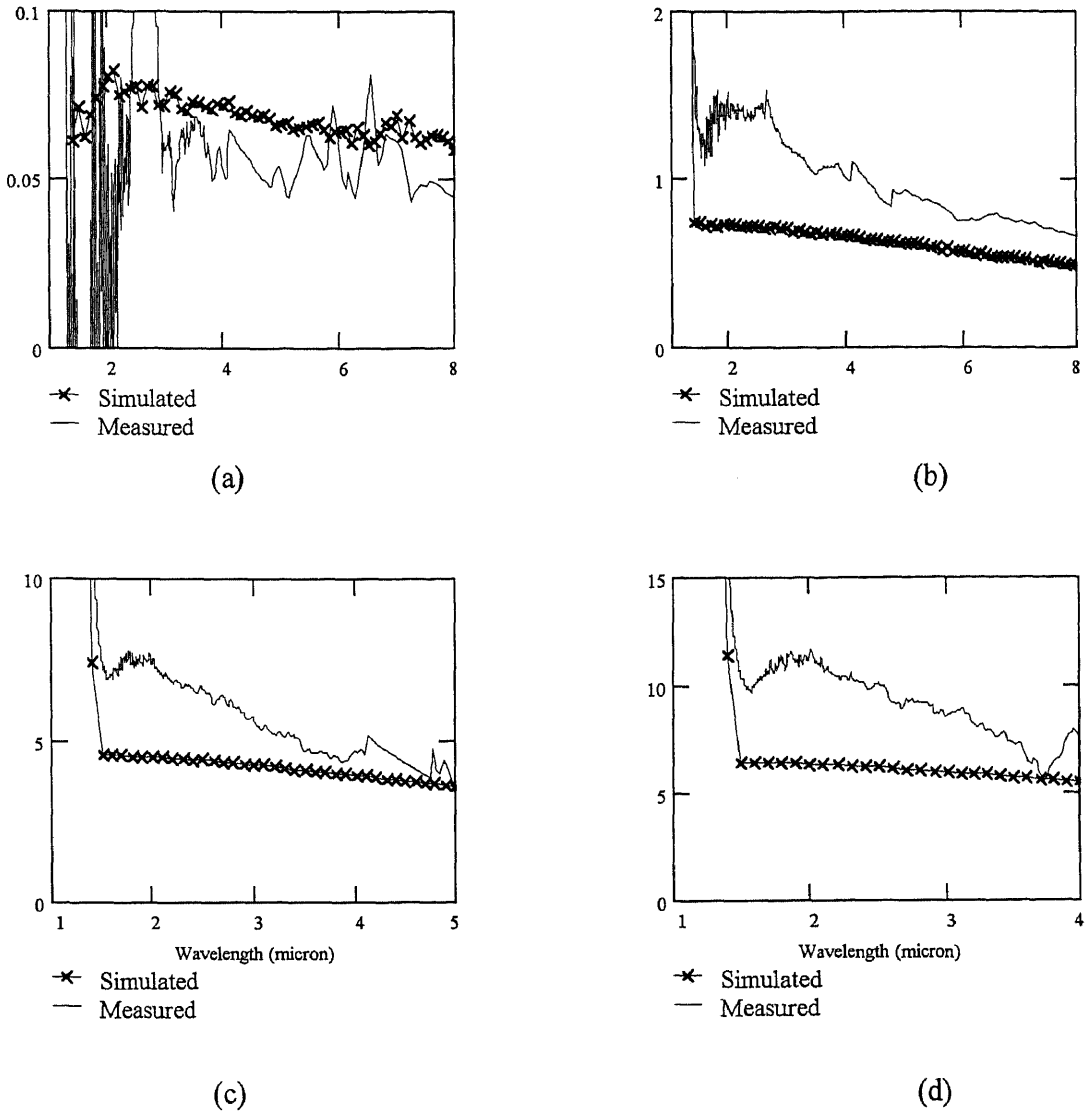

Fig.37 Comparison between the ratios of the measured and simulated absorption coefficient divided by λ^2 for p-Si, $7\times10^{14}cm^{-3}$ for: a) 359, b) 479, c) 605 and d) 632°C

To compare these results, a simple overlay of the measured over the simulated transmittance is shown in Fig.38(a)-(d). These figures show that the simulated transmittance is always larger than the measured transmissivity except for Fig.38(a).

In conclusion, it is clear that the model utilizes appropriate parameters resulting in agreement with measured α for both n and p-Si. However, to obtain very accurate α at temperatures below the opacity of silicon and at sub-bandgap energies, it is necessary to understand fully the parameters included in equation (5.5), as function of temperature, and to understand thoroughly the contribution of band structure. In n-Si, the intraband contribution at room temperature is clear but it needs to be modeled and extended to higher temperatures while for p-Si intraband transition in the valence band are not observable. One solution to the problem is to take the easy way out by using the most reliable numerically fitted model for bulk properties of silicon such as n and k performed by Li [57] and Magunov [56] and treat the problem as an optics problem rather than try to obtain the parameters from the classical Drude model which ignores subtleties such as band structure and temperature dependence of effective masses.

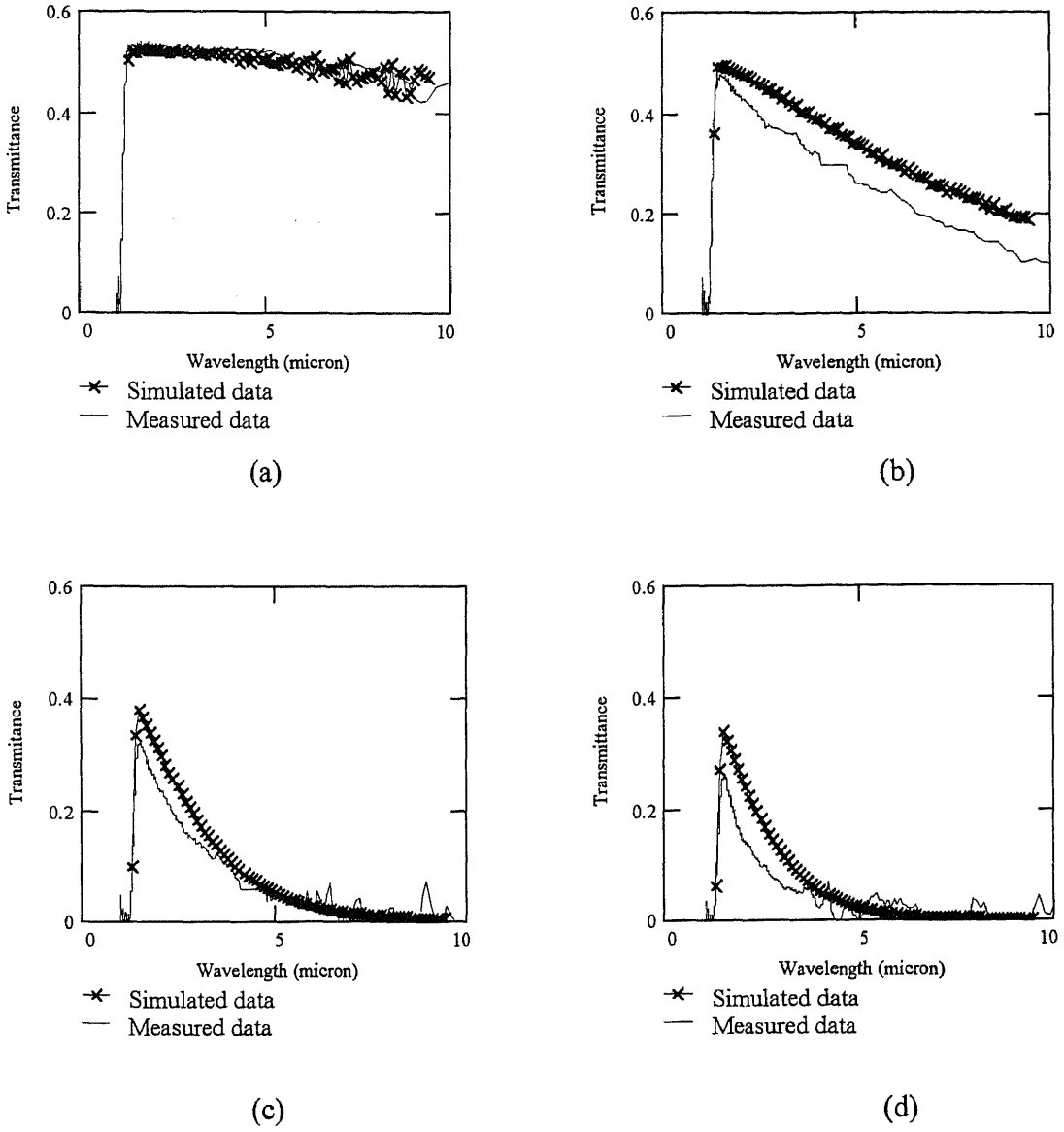

Fig.38 Comparison between the measured and simulated data for p-Si, $7\times10^{14}cm^{-3}$ for: a) 359, b) 479, c) 605 and d) 632°C

CHAPTER 6

RESULTS AND DISCUSSIONS (II)

6.1 Silicon Nitride - Si_3N_4

Non-crystalline silicon nitride Si_3N_4 is an important material in integrated circuit technology. It is used in thin-film form and can be prepared by many deposition techniques including: a) chemical vapor deposition (CVD) from a mixture of gases containing silicon and nitrogen such as SiH_4 and NH_3, b) sputtering and c) RF glow-discharge methods. It can also be deposited using RTCVD using gases such as SiH_4 and NH_3. Si_3N_4 is an attractive dielectric because of its high dielectric constant ($\varepsilon = 5.4$). Si_3N_4 is of interest to: a) optical waveguides, b) antireflection coatings and c) MOS devices. The National Technology Roadmap for Semiconductors (NTRS) for 1997 is predicting that by the year 2009 and for submicron CMOS technology of 70nm, the required gate oxide thickness will be < 1.5nm [5]. At such ultra small thickness, the oxide is expected to perform poorly with the tunneling current exceeding $1A/cm^2$. As a result, the device will degrade very fast. To solve such a problem, a thicker dielectric but with a higher dielectric constant ε is needed to maintain a high capacitance. Therefore, a combination of nitride and oxide is being sought in the form of silicon oxynitride SiO_xN_y as one of the major alternatives to SiO_2 ($\varepsilon = 3.9$) as a gate dielectric in the future MOS capacitors [103-105]. Most of the studies of optical properties and bulk properties of Si_3N_4 have been limited to the visible [106], mid IR lattice absorption bands near 0.11eV and other bands, i.e. $\lambda = 11.2\mu m$ [107]. To the best of our knowledge the optical properties of Si_3N_4 have not been studied

in the range of interest for pyrometry in RTP, i.e. 1-5μm. Philipp [108] has reported the bulk properties of Si_3N_4 from 1-24eV. He found that at 1eV, for Si_3N_4, the refractive index n = 1.998, the extinction coefficient is $< 2\times10^{-4}$, below reliable detection abilities.

Using the Spectral emissometer, temperature dependent emissivity measurements have been performed on 0.125 inch thick Si_3N_4 sample supplied by NORTON. Examples of these results for temperatures of 135°C and 805°C are presented in Fig.39. The figure shows that the Si_3N_4 absorption is very weakly dependent on temperature. The transmittance of this bulk Si_3N_4 is negligible in the wavelength range of 1-20μm. Using equations (3.7), (3.5) and neglecting k, we calculate the refractive index as function of temperature for Si_3N_4. These results are summarized in Fig.40 [109]. As can be seen in this figure, the change in n with T is very small for Si_3N_4 in the wavelength range of 1-20μm.

6.2 SiO_2/Si, SiO_2/Si/SiO_2 and SiO_2/Si/SiO_2/poly-Si Control wafers

Silicon dioxide SiO_2 accounts for 100% of the gate oxide in MOS devices and is essential for other applications such as isolation in the form of local oxidation of silicon LOCOS [111] and trench walls in processes like damacene [112]. Because of their low extinction coefficient k, dielectrics such as SiO_2 are media of low or no loss for the passage of photons. Thus, light reflected at the bottom surface of SiO_2 can constructively or destructively interfere with the light reflected at the top surface especially if there is a high degree of coherency when the thickness of the oxide is comparable to the wavelength of

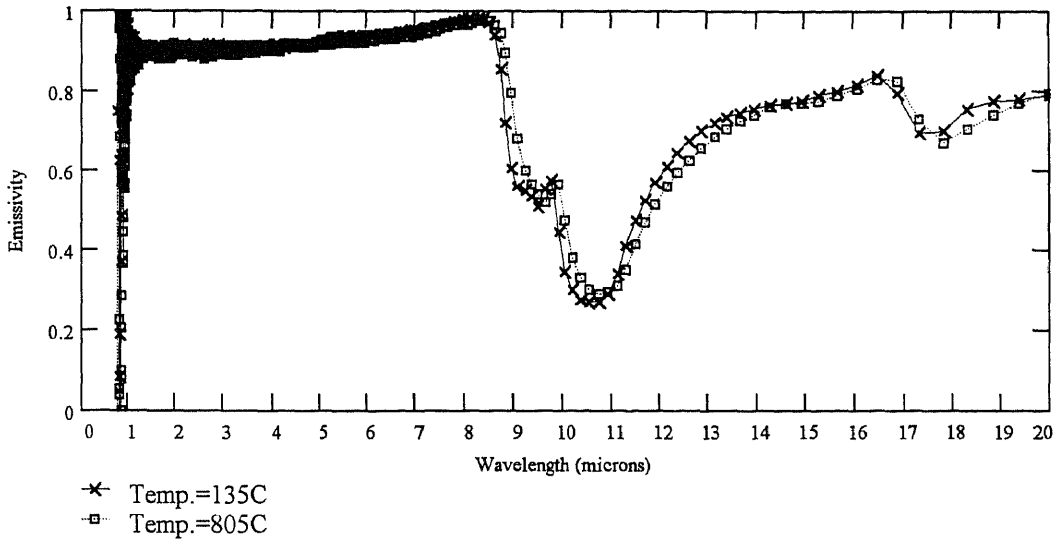

Fig.39 Refractive index as function of wavelength for bulk Si_3N_4, at two different temperatures

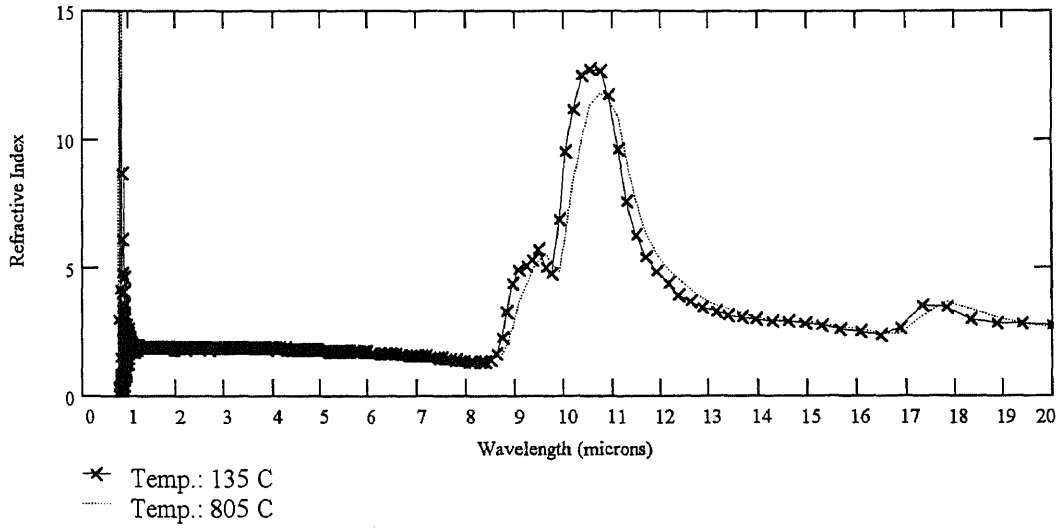

Fig.40 Emissivity as function of wavelength for bulk Si_3N_4, at two different temperatures

the light. This leads to unwanted changes in the emissivity of the underlying silicon wafer. Rapid thermally grown oxides have not been popular because of the difficulties in growing uniformly thick oxide all over the wafer. Other applications such as rapid thermal annealing of dopant that was implanted through an oxide cap might also have difficulties in measuring the accurate temperature of the wafer because of the thick oxide. For this reason, an experimental study has been performed to understand the effect of oxide on the emissivity of silicon. The samples considered are SiO_2/Si, with oxide as the top layer, of thickness of 653, 1144, 2031, 3600 and 5124A grown on a heavily doped silicon substrate. In Fig.41, the emittance of these samples is plotted as a function of temperature at the wavelength of 1.53μm. Here, we see two interesting phenomena: i) For each of the wafers under investigation, the emittance increases and then starts decreasing; ii) The order in which the wafer emittance decreases is a function of the oxide thickness (a = 2031A, b = 1144A, c = 653A, d = 3600A and e = 5124A) [109,33]. Replotting in Fig.42 the emittance for these wafers as a function of the oxide thickness at different temperatures and for the same wavelength i.e. 1.53μm, shows a peak at 2031A independent of temperature. Similar analysis has been made at λ = 2.5μm in Fig 43 [33]. Interestingly, the peak corresponding to emittance maxima is noticed to shift towards higher oxide thickness, 3600A. As expected the oxide thickness corresponding to the emittance maximum is independent of temperature for a specific wavelength.

Regarding the shift noted above, it is obvious that when the light is incident on the thin dielectric on an opaque substrate, the emissivity of the sample as a whole is a function of the interference effects due to the dielectric. Since the extinction coefficient k and hence

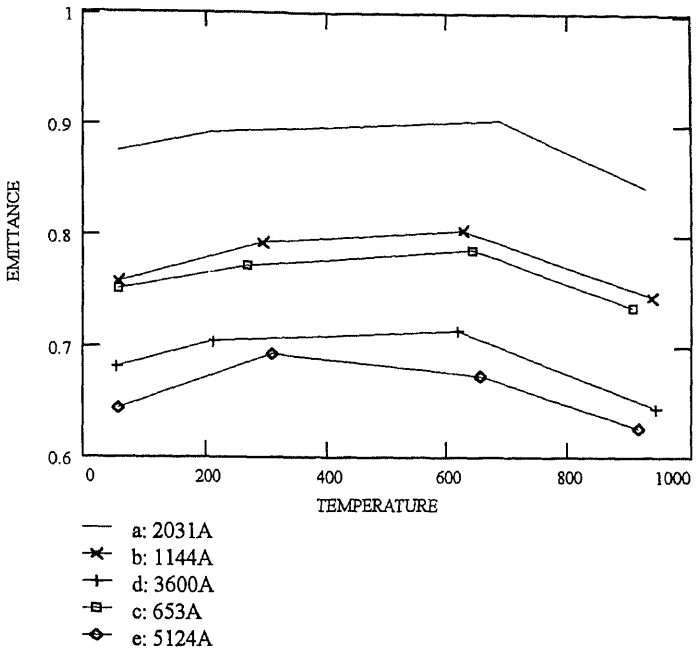

Fig.41: Emissivity as function of temperature for SiO_2/Si for different oxide thickness at λ = 1.53μm

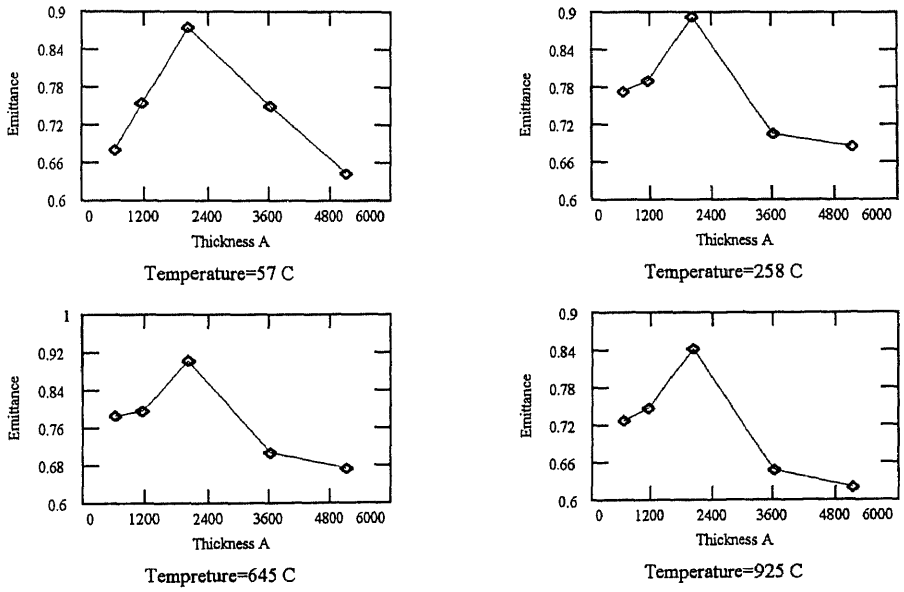

Fig.42: Emissivity of SiO_2/Si as function of oxide thickness for four different temperatures at λ =1.53μm

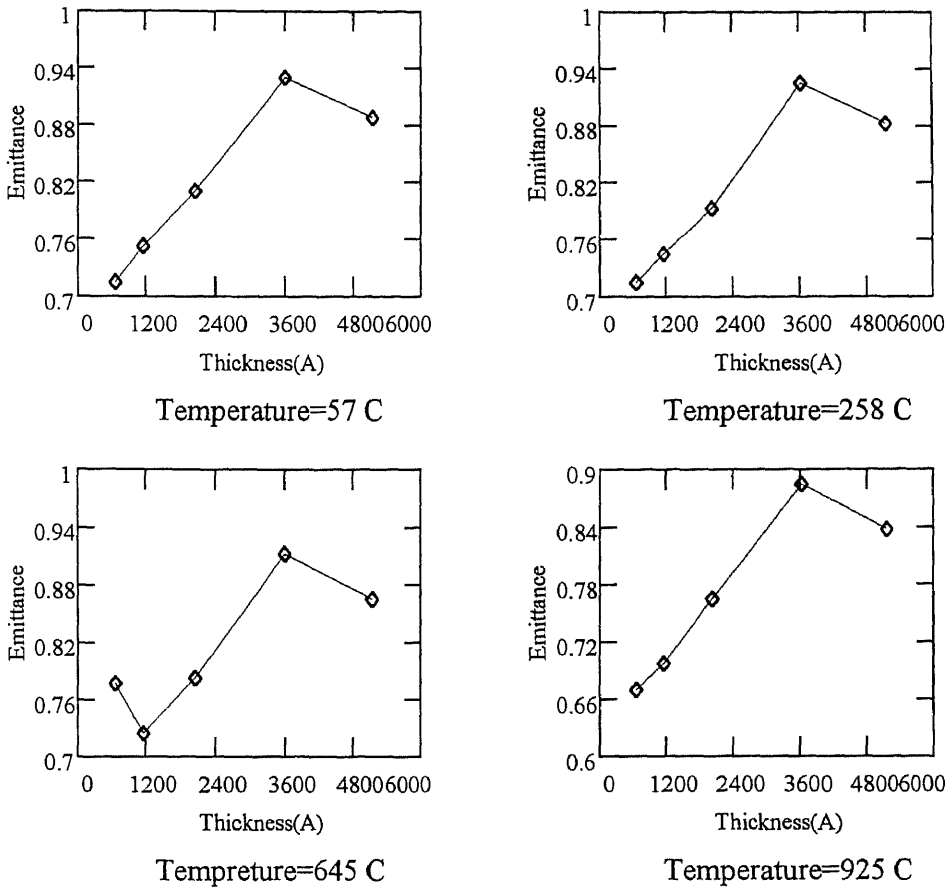

Fig.43: Emissivity of SiO_2/Si as function of oxide thickness for four different temperatures at $\lambda = 2.5\mu m$

the absorption coefficient α of the SiO_2 have a very weak dependence on temperature, the interference effect will be the dominant factor in the apparent reflectivity of the wafer. Thus, if the interference of two reflected waves, one from the top and the other from the bottom planes of the oxide is constructive, the measured reflectivity will be a maximum resulting in minimum emissivity and the opposite is true.

To continue the study of the oxide effects on the wafer emissivity at high temperatures, a sample supplied by Lucent Technologies and consisting of $SiO_2/Si/SiO_2$ structure has been investigated. Both the front and the backside oxides have the thickness of 5000A. In Fig.44, the emittance of this wafer is plotted as a function of temperature for various wavelengths (A1 at 2.5μm, B1 at 2.7μm, C1 at 3.3μm and D1 at 4.5μm). As can be seen from the figure, the emissivity as a function of temperature for the various wavelengths is almost the same with the slight exception for the emissivity corresponding to 4.5μm. However, the behavior in Fig.44 is different from the measurements performed on SiO_2/Si above (Fig.41). The emissivity saturates at a level $\varepsilon \sim 0.9$ for temperatures above 672°C as seen in Fig.44 [33]. In order to understand this behavior, consider the emissivity decrease above 600°C in Fig.41. The results show an average slope of -1.8×10^{-4} $°C^{-1}$ which is equivalent to the findings of Nulman et al [113]. for a silicon wafer with 8000A SiO_2 on both sides ($\rho = 10\Omega.cm$ at $\lambda = 4.5\mu m$). Nulman et al. found that the slope is $\sim -8.9\times10^{-5}$ $°C^{-1}$ for temperatures above 600°C. A similar effect has been confirmed by Sato [28] for a bare n-Si wafer when he found that the true reflectivity increases from 0.3 to 0.32 due to index of refraction increase. Hence this effect is due to the substrate. So the question is why is this negative slope not seen in the data in Fig.44 at higher temperatures?

For the moment this remains a puzzle. In Fig.45, some of data that are used to obtain Fig.44 are presented as a function of wavenumber. In this figure, it is shown that even at the highest temperatures considered, the emissivity either increased or remained the same. This means that the reflectivity of this sample did not increase and that the refractive index remains constant as temperature rises. It is an interesting finding that needs further study.

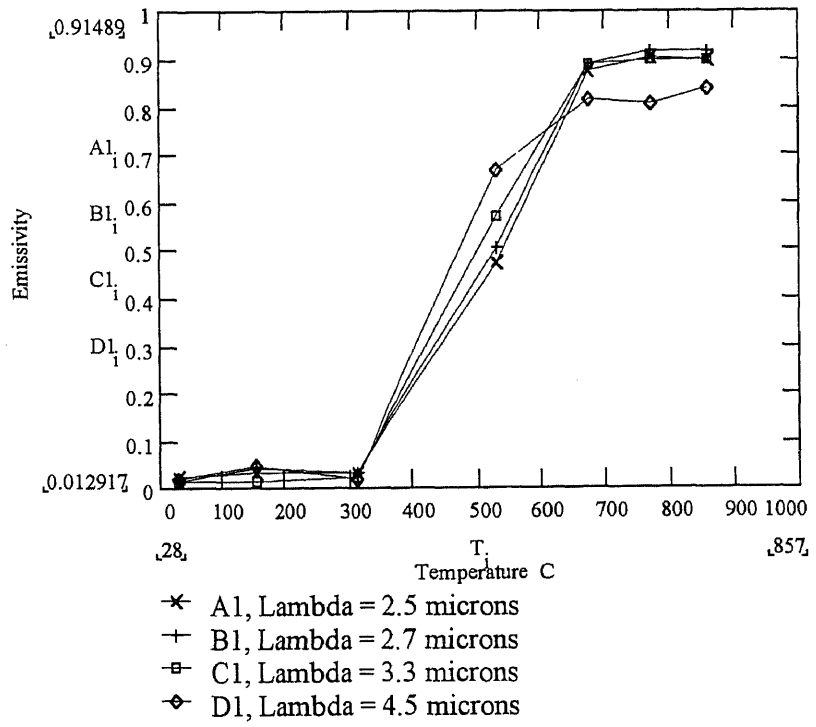

Fig.44 Emissivity as function of temperature for $SiO_2/Si/SiO_2$, with oxide thickness of 5000A from both sides, λ = 2.5, 2.7, 3.3 4.5μm

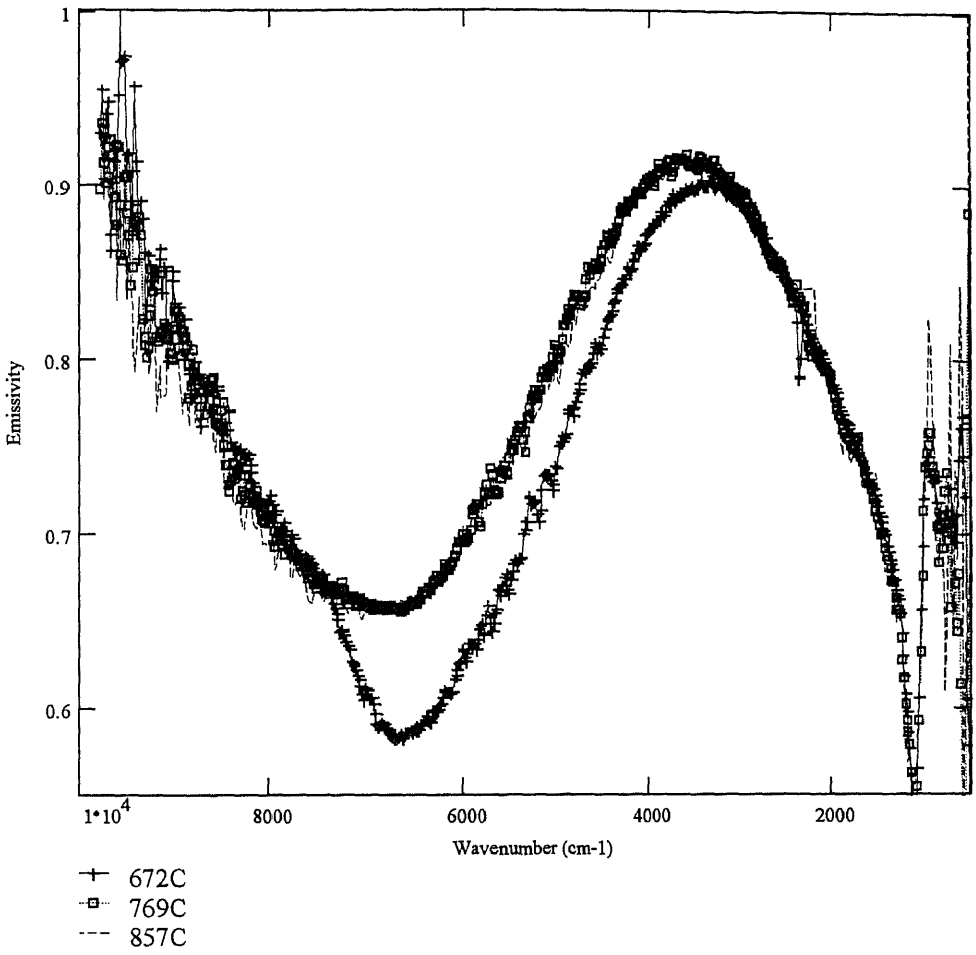

Fig.45 Emissivity as function of wavenumber for three specific temperatures of $SiO_2/Si/SiO_2$, with oxide thickness of 5000A from both sides

Most of the manufacturers of commercial RTP systems in the semiconductor industry have chosen pyrometers to operate at five specific wavelengths - 0.95, 2.5, 2.7, 3.3 and 4.5μm. In Figs.46 and 47, emissivity of sample: 4100327#7, 100A SiO_2 /700μm p-Si /1600A SiO_2 /700A poly-Si and sample: 4100326#14, 100A SiO_2 /700μm p-Si /250A SiO_2 /700A poly-Si are plotted as a function of temperature for four specific wavelengths - 2.5, 2.7, 3.3, 4.5μm. These wafers along with the others discussed in this section are called control wafers because they are used to simulate wafers in a manufacturing environment. The poly-Si layer is essential to see its effect on the emissivity of the wafer in an RTA process that is needed for dopant activation and implant anneal in the gate poly. It is also important to see its effect in stabilizing the emissivity of the wafer with deposition on the back-rough side facing the pyrometer. In Figs.46 and 47, it can be seen that the emissivity decreases as the temperature exceeds 600°C. To see the effect of the poly on the wafer emissivity, the emissivity of the front-polished incidence versus that of the back-rough incidence are plotted separately and shown in Fig.48. In this figure, the roughness effects have been to increase the emissivity for the sample with the thinner backside oxide #14, whereas the dominant effect of optical interference is clearly demonstrated in the case of the thicker backside oxide #7. Fig.49 displays the optical properties of these samples overlaid at room temperatures for front-side incidence. For sample #14, the thickness of the oxide is too thin to cause any interference effects in the considered spectrum unlike sample #7 [114].

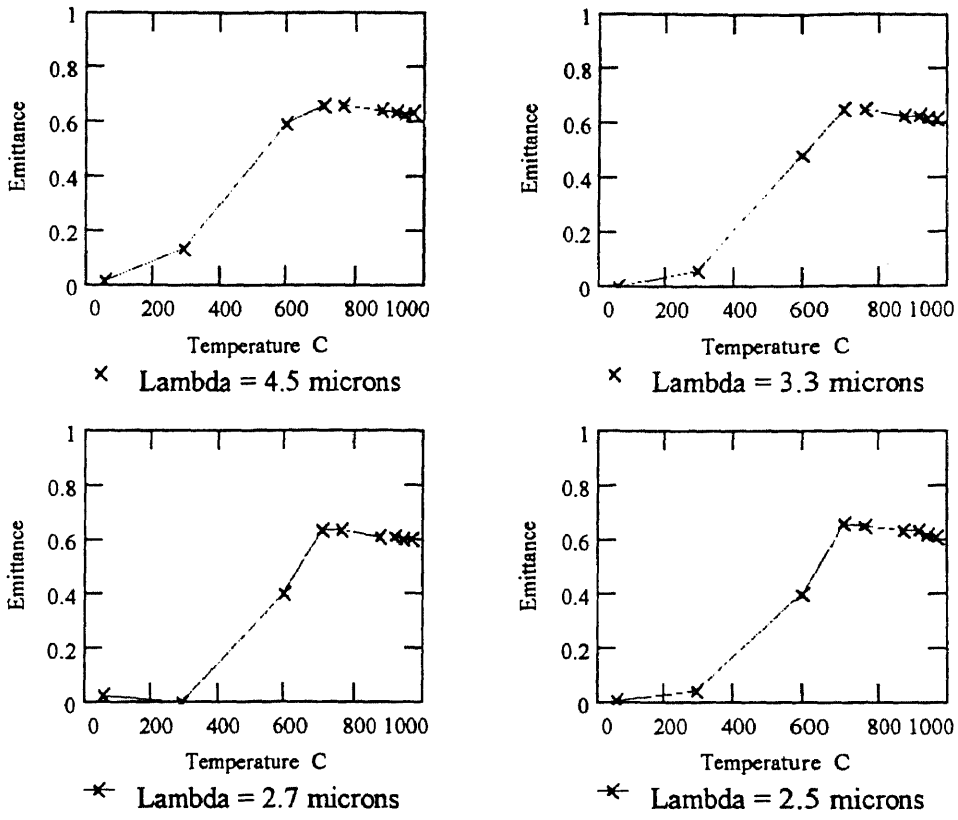

Fig.46 Emissivity as function of temperature for $SiO_2/Si/SiO_2$/poly-Si, with backside oxide thickness of 1600A, λ =2.5,2.7,3.3and 4.5μm

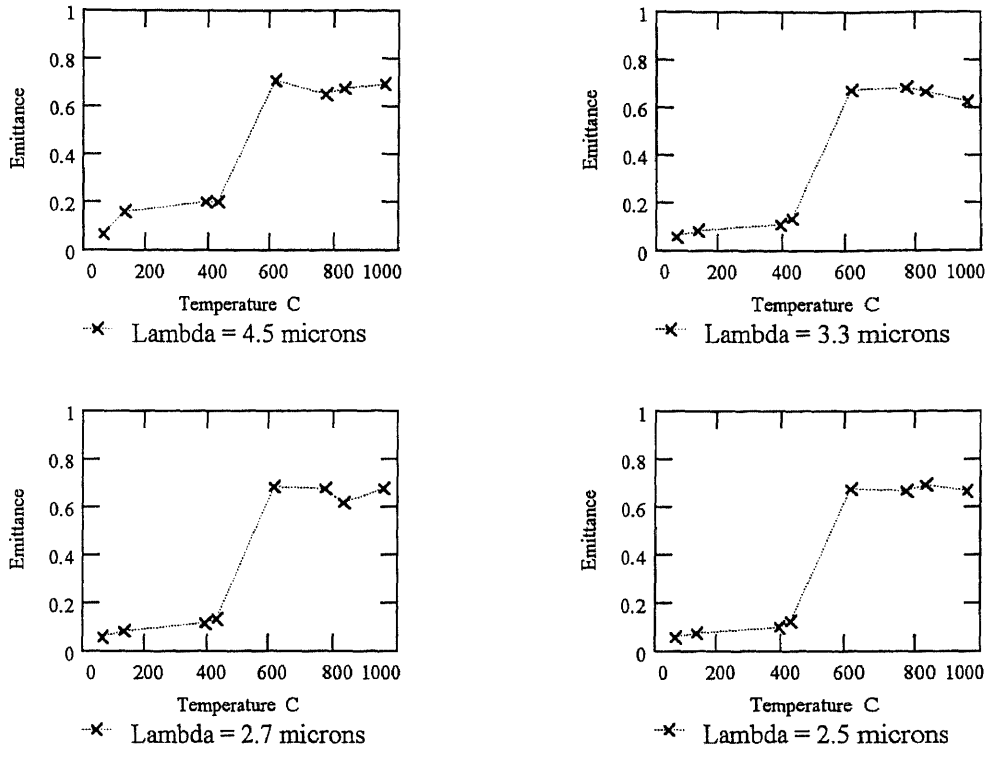

Fig.47 Emissivity as function of temperature for $SiO_2/Si/SiO_2$/poly-Si, with backside oxide thickness of 250A, λ = 2.5, 2.7, 3.3 and 4.5μm

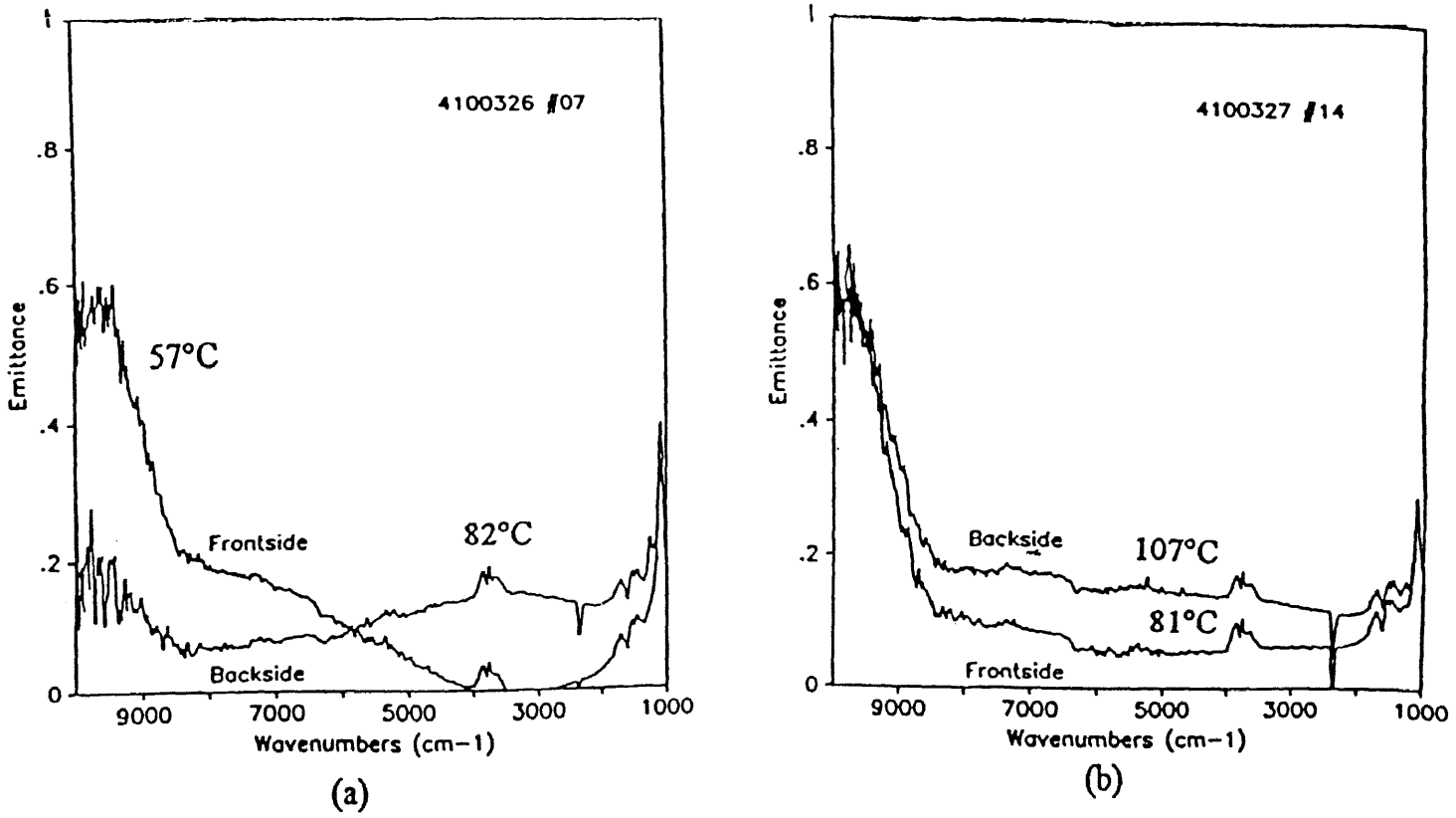

Fig.48 Comparison of frontside versus backside emissivity of SiO_2/p-Si/SiO_2/poly-Si with backside oxide thickness of 1600A for #7 and 250A for #14

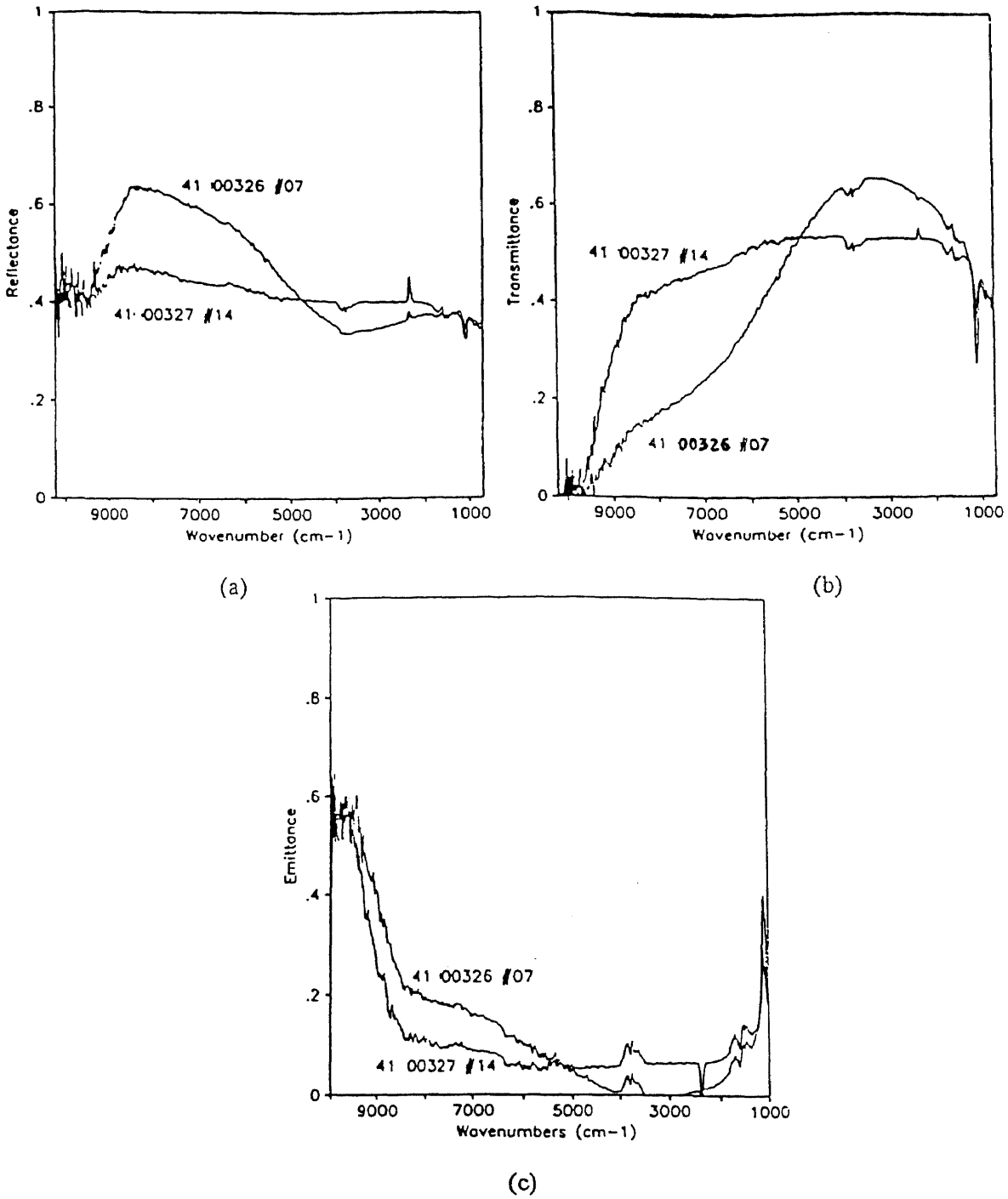

Fig.49 Measured reflectance, transmittance and emittance for SiO_2/p-Si/SiO_2/poly-Si with backside oxide thickness of 1600A for #7 and 250A for #14 250A

6.3 Separation by Implantation of Oxygen - SIMOX

Improvements in the performance of MOS transistors are expected to lead to high switching speed, high channel mobility, lower kink effect and minimal latch up effects. Such electrical properties can be obtained by utilizing ultra thin silicon on insulator (SOI) wafers [115,111]. One of the methods of fabricating SOI wafers involves the implantation of oxygen into silicon (separation by implantation of oxygen - SIMOX). Despite SIMOX being a mature technology, its optical characterization and modeling represents a challenge because of the multi-layer effects. Several studies have been made in the literature on the optical properties in the visible to near IR regime [116,117]. If SIMOX is to be the wafer for the future and RTP is the process approach, then accurate modeling for the optical properties of SIMOX in the near-mid IR is required. We have investigated the experimental and simulated optical properties of SIMOX covering the spectra of importance to the RTP and semiconductor industry [33,118,119]. The SIMOX wafer investigated in this study consisted of <100> p-type, $< 1\times10^{16}cm^{-3}$, with ~200nm thick silicon films on top of ~400nm of buried oxide. The oxide layer was formed by implantation of oxygen at 200keV to a dose of $1.8\times10^{18}cm^{-2}$ and subsequent annealing above 1300°C for several hours. In Fig.50(a) - 50(c), the measured and simulated front side incidence reflectivity, transmissivity and emissivity of the SIMOX sample have been presented for three temperatures: 21, 458 and 898°C, respectively. The backside incidence results are shown in Figs 51(a) - 51(c) for temperature: 17, 487 and 895°C. The simulated results are based on the Multi-Rad MIT/SEMATECH model discussed in chapter 5. The sample exhibits high apparent reflectivity compared to that of bare silicon

dominantly due to the multi-layer interfences. The results of the simulation are in good agreement for both the front side and backside incidence. Even the phonon contribution for wavelengths above 5 microns have been represented very well by the model. The observed differences, however, can be explained by the lack of complete knowledge of the parameters involved such as the exact thickness of the layers or the bulk properties of silicon and silicon oxide incorporated in the model. The discrepancy in Figs.50(b)-50(b*) as the experimental transmittance decreases much faster than the simulated one can partly be due to the α values considered in the model which are less than the measured ones for p-Si, and partly due to temperature reading errors. Fig.51(c) and 51(c*) show the silicon substrate effect as the sample becomes opaque. At such temperatures, the backside contribution of the oxide and thin silicon layer is simply not there. It is also noticed from Fig.50(a) that at 4000cm^{-1}, equivalent to 2.5μm, the principal maxima has its peak, while the destructive interference takes place at $\lambda \sim 1.5\mu$m. Interestingly, the destructive minima keeps decreasing in value with increasing temperatures as in Fig.50(b) and 50(c). A possible explanation is that at room temperature, the two upper layers caused a principal minima but the contribution from the backside compensated that. For temperatures above the opacity of silicon the backside contribution in the measured reflectivity vanish resulting in a zero reflection. The temperature and wavelength dependence of front side emittance of SIMOX, at selected wavelengths, is presented in Fig.52. In this figure, the emissivity values are plotted for four specific wavelengths: $\lambda = 2.5$, 2.7, 3.3 and 4.5μm as function of temperature. As can be seen in Fig.52, the emissivity is very small ($\varepsilon < 0.2$) even at high temperatures (600°C, $\lambda = 2.5$, 2.7 and 3.3μm). It approaches 0.6 at 4.5μm for T > 600°C.

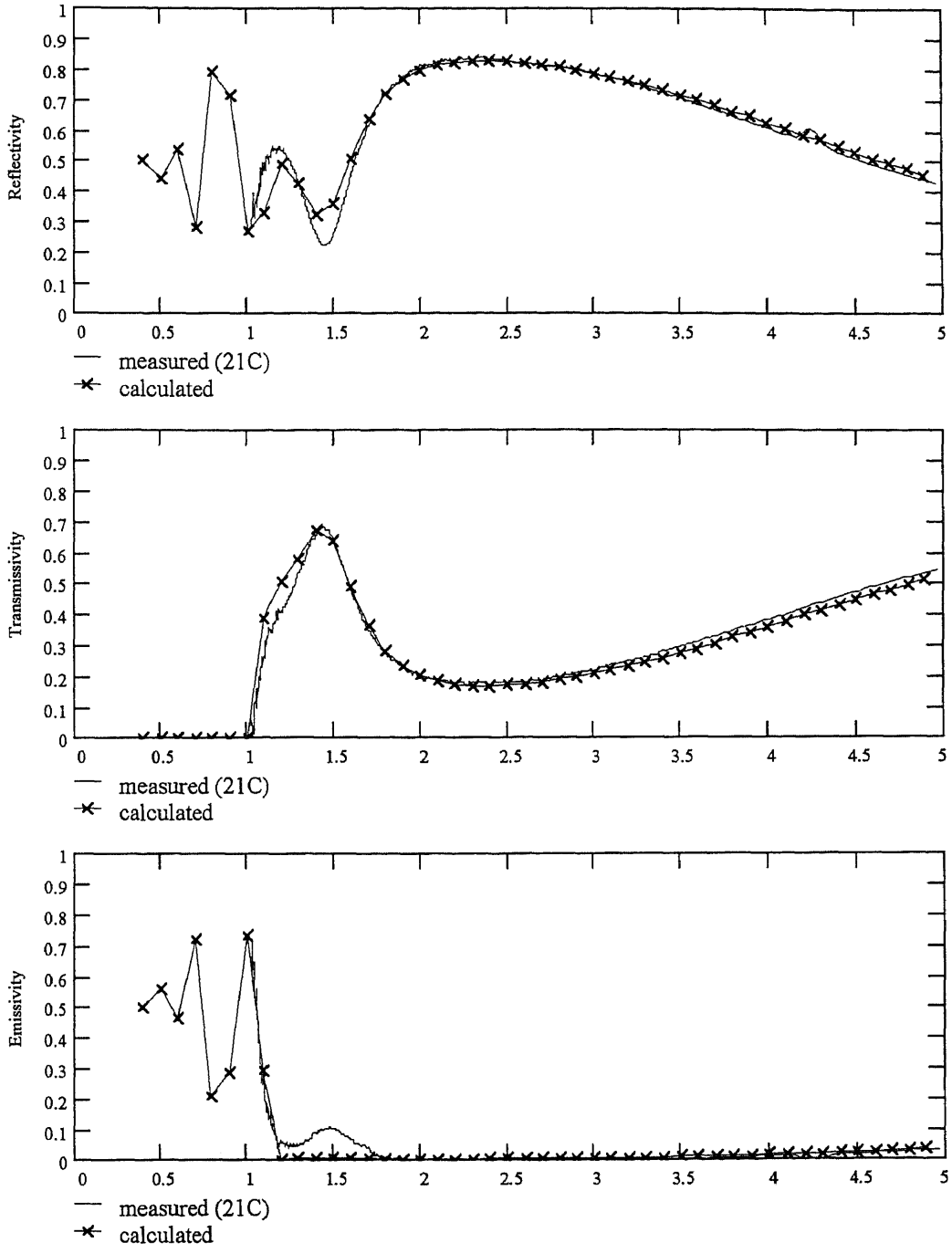

Fig.50(a) Comparison between the measured and simulated optical properties of SIMOX, incidence is on the smooth side, at 21°C

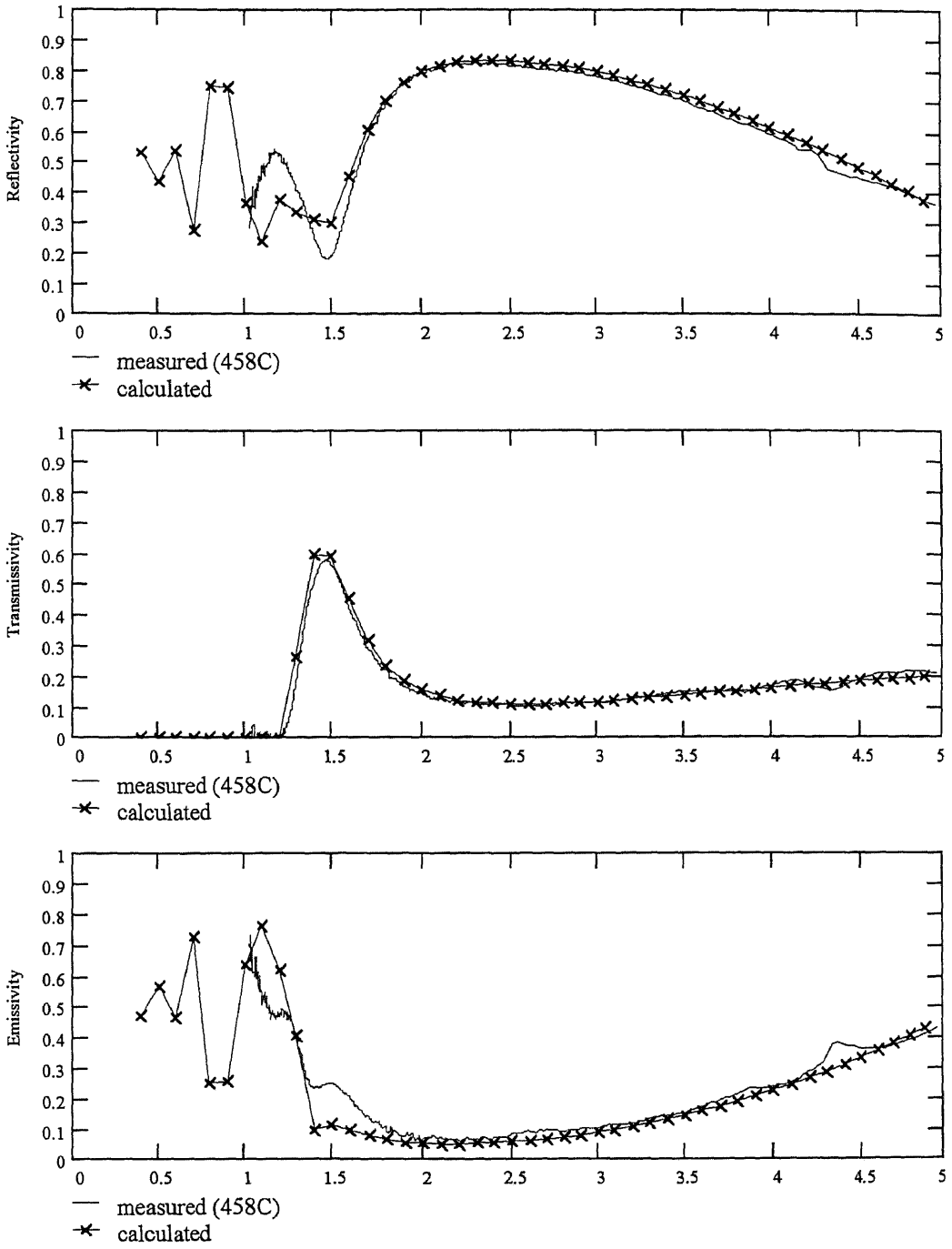

Fig.50(b) Comparison between the measured and simulated optical properties of SIMOX, incidence is on the smooth side, at 458°C

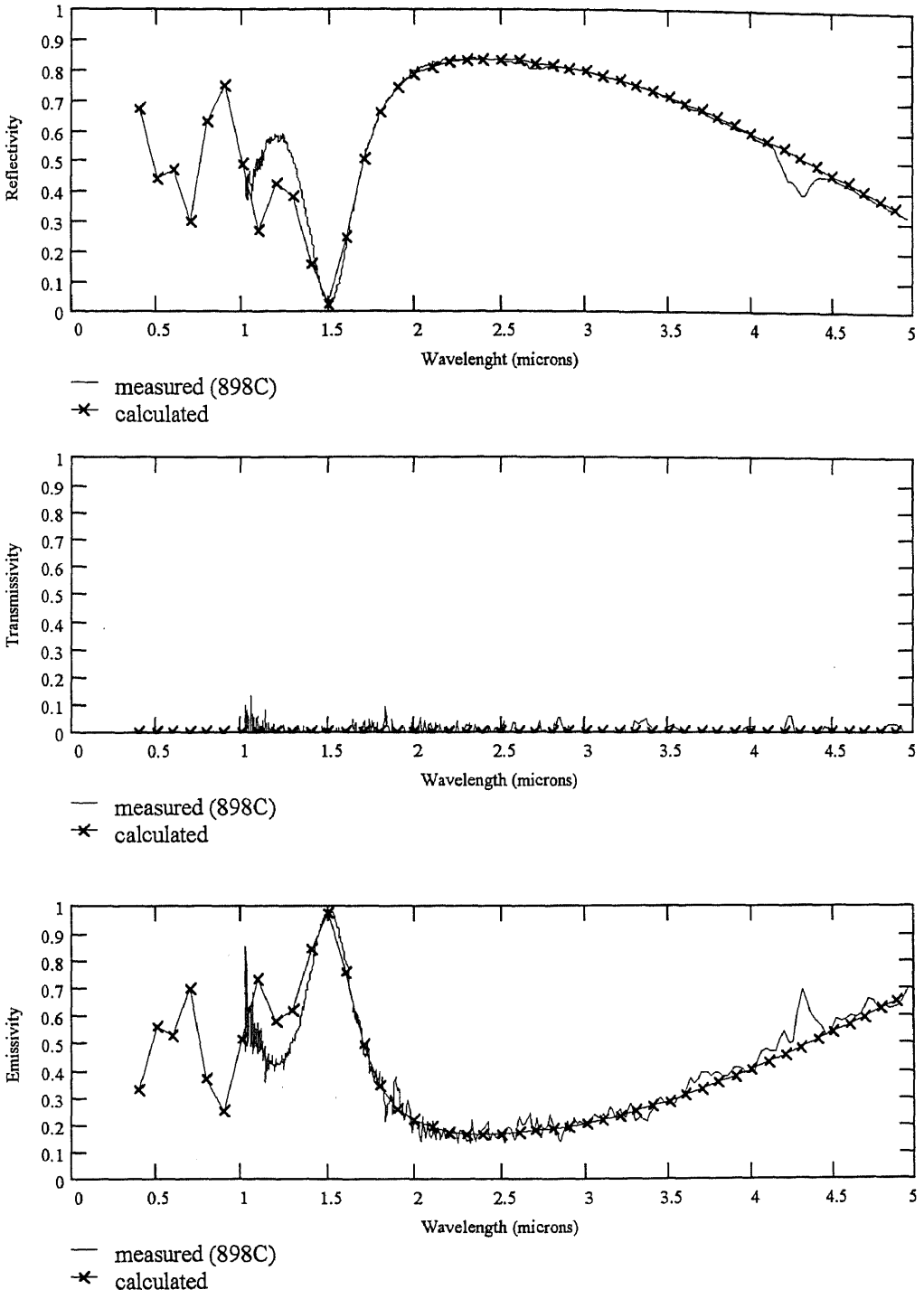

Fig.50(c) Comparison between the measured and simulated optical properties of SIMOX, incidence is on the smooth side, at 898°C

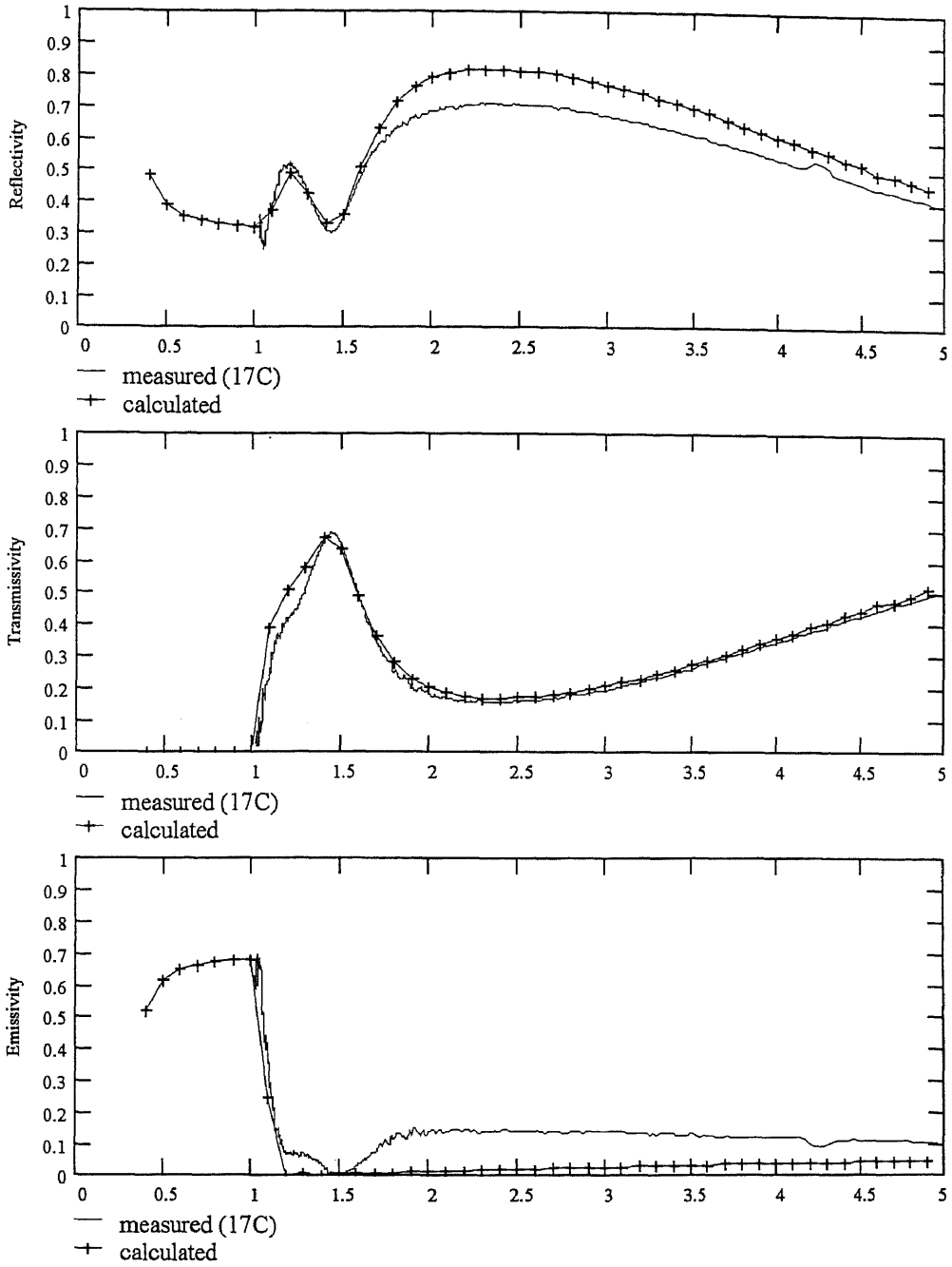

Fig.51(a) Comparison between the measured and simulated optical properties of SIMOX, incidence is on the rough side, at 17°C

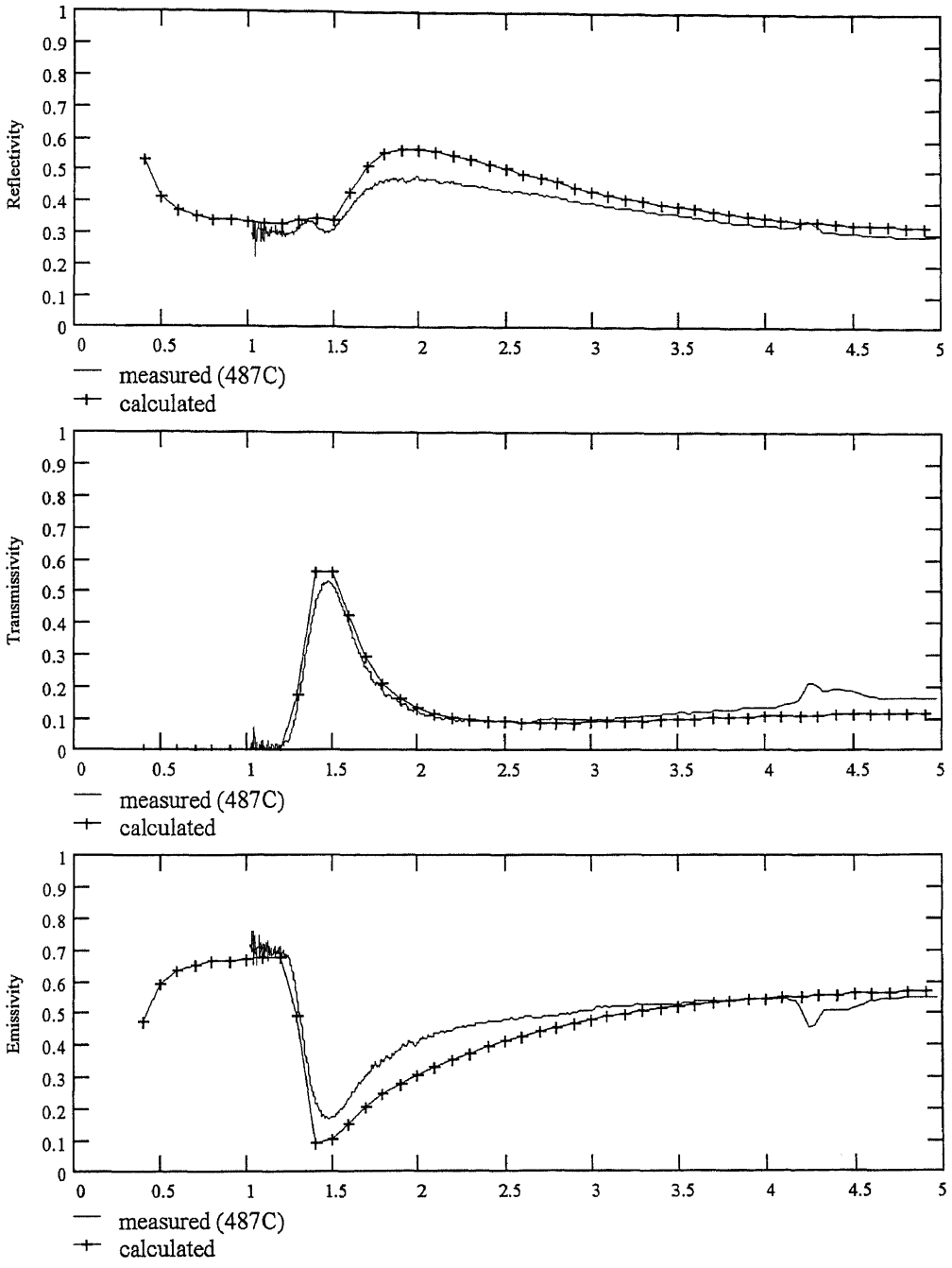

Fig.51(b) Comparison between the measured and simulated optical properties of SIMOX, incidence is on the rough side, at 487°C

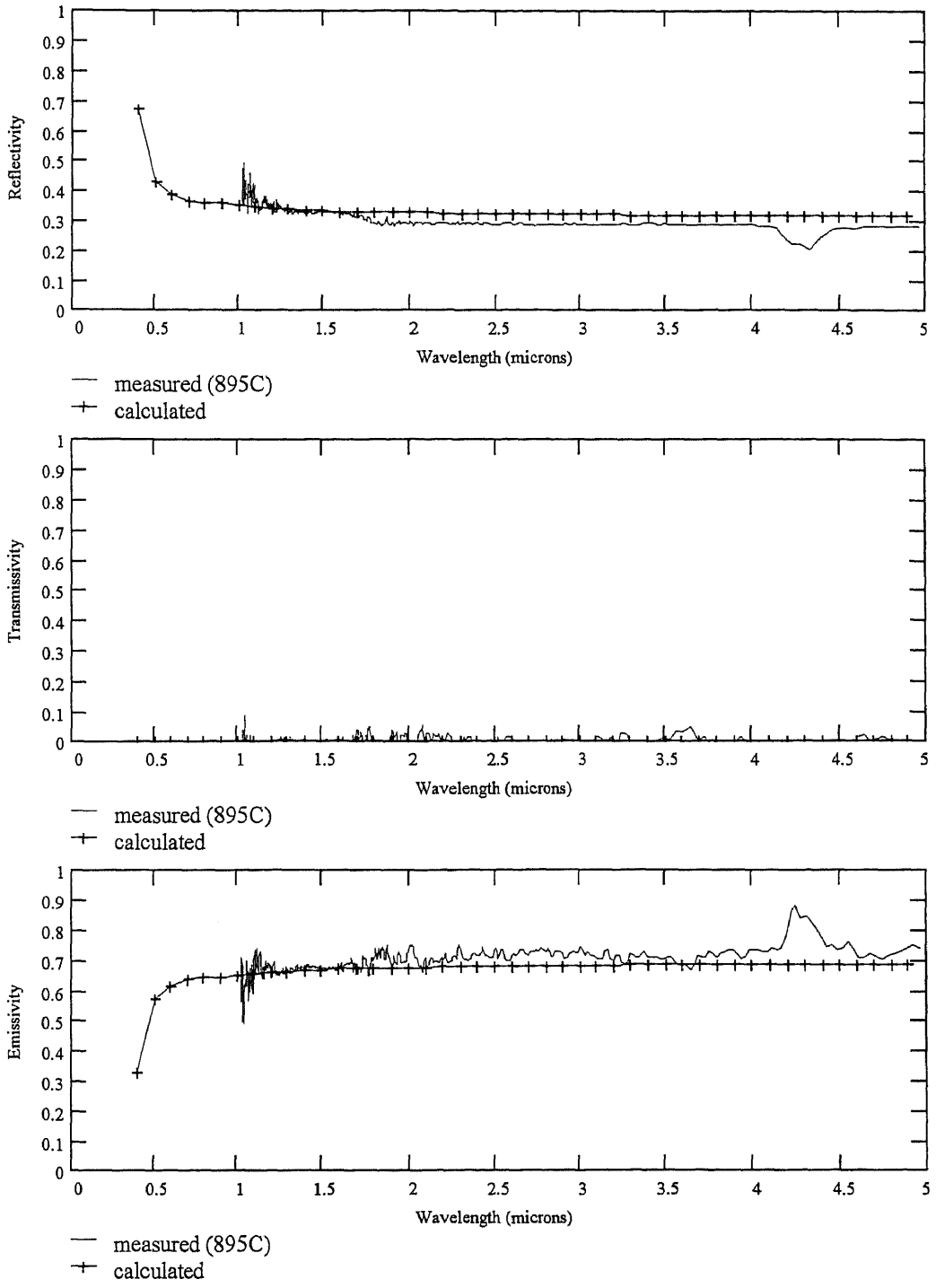

Fig.51(c) Comparison between the measured and simulated optical properties of SIMOX, incidence is on the rough side, at 895°C

Most pyrometers need a minimum threshold value of emissivity to be able to operate. Therefore, while a contact technique of measuring temperature of such a sample records high temperatures, a pyrometer that operates at the above mentioned wavelengths will have difficulty sensing a signal due to the low radiance from the sample surface. The suggested choices of wavelengths of operation for pyrometry based on Fig.52 are: (a) 0.95μm - a standard choice of applications in RTP due to zero transmittance in silicon; (b) 4.5μm - for temperatures above 600°C; (c) 1.43μm - appropriate for high temperature applications as the silicon becomes opaque; and (d) 5-6.65μm - this region corresponds to high and steady emissivity for temperatures higher than 400°C.

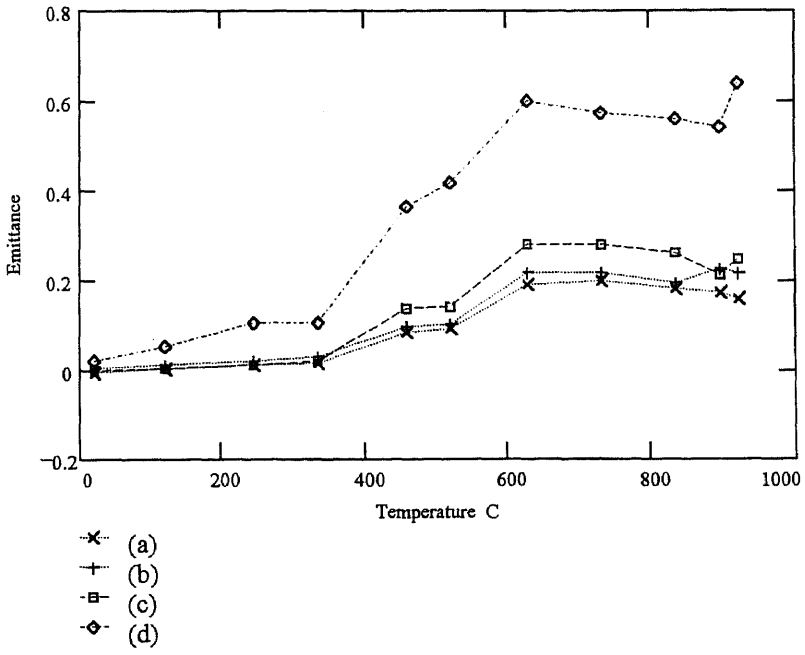

Fig.52 Emissivity as function of temperature for SIMOX, for λ = (a) 2.5, (b) 2.7, (c) 3.3 and (d) 4.5μm

CHAPTER 7

MODELING

In this chapter, models for optical properties crucial to applications of pyrometry as a non-contact method of determining temperature in RTP are discussed. As seen before, silicon wafer emissivity is quite a complicated function of three main parameters: a) Intrinsic - referring to substrate, b) extrinsic -referring to coatings and deposited or grown layers of different materials and c) chamber components combined together and defined as effective emissivity. In this section, an attempt is made to understand the first two-parameters.

7.1 An Overview

As a thermal radiative property emissivity has been used to determine temperature. Emissivity is an optical property. Equation (3.10) shows that for any incident electromagnetic ray or bundle of rays, the response of the material, both optically and radiatively, is the summation of the reflected, transmitted and emitted (absorbed) parts of the original incident intensity. Hence, determining reflectance and transmittance and calibrating for the full source incident intensity, gives us the required emissivity. The emissometer determines emissivity in this manner. Reflection and transmission are functions of the optical parameters, n and k. To interpret these optical properties, an understanding of the way materials respond to electromagnetic waves is required.

7.1.1 Optical Properties in Solids

From electromagnetic theory, the propagation of electromagnetic waves is described by Maxwell's equations. These equations set the relation between the electric field, the magnetic field and the bulk material properties such as the dielectric constant, ε_r, and the magnetic permeability. Most of the materials considered in this study and of importance to RTP have $\mu_r \sim 1$. Further, ε_r is constant throughout the homogeneous layer. Understanding the behavior of material with electric field leads us to understand the response of the material to the propagating wave. Hence, the importance of the dielectric constant [31]. In an absorbing medium, ε_r is a complex quantity defined as:

$$\varepsilon_r = \varepsilon_1 + i\varepsilon_2 \tag{7.1}$$

This parameter cannot be measured directly. It is defined as a function of the optical constants by the relation:

$$\varepsilon_r = n_c^2 \tag{7.2}$$

In an absorbing medium, the refractive index becomes complex:

$$n_c = n + ik \tag{7.3}$$

where n and k are the real refractive index and the extinction coefficient. Solving for equations (7.1) and (7.3), we get:

$$\varepsilon_1 = n^2 - k^2 \tag{7.4}$$

$$\varepsilon_2 = 2nk \tag{7.5}$$

Understanding n and k is an important issue. It can be done through the principle of causality, which leads to the well known Kramers-Kronig equations [120], which also relates the frequency dependence of n and k, ε_1 and ε_2, and α and R.

7.2 Sample Properties and their Effect on the Spectral Emissivity

Consider an electromagnetic wave incident on a single surface material, or the top surface of a double-side polished sample as in Fig.5. The material will interact with the electric field in a certain way that has been studied extensively by Fresnel in 1823 [121]. Utilizing the refraction law, Snell's law, and the reflection law, Fresnel found that depending on the electric field component orientation compared to the plane of incidence, i.e. parallel or perpendicular, the complex amplitudes of the reflected and transmitted waves are related to the incident part by the following relations:

$$T_{\text{II}} = \frac{(2n_1 \cos\vartheta_i)}{n_2 \cos\vartheta_i + n_1 \cos\vartheta_t} A_{\text{II}} \tag{7.6}$$

$$T_{\perp} = \frac{2n_1 \cos\vartheta_i}{n_1 \cos\vartheta_i + n_2 \cos\vartheta_t} A_{\perp} \tag{7.7}$$

$$R_{\text{II}} = \frac{n_2 \cos\vartheta_i - n_1 \cos\vartheta_t}{n_2 \cos\vartheta_i + n_1 \cos\vartheta_t} A_{\text{II}} \tag{7.8}$$

$$R_{\perp} = \frac{n_1 \cos\vartheta_i - n_2 \cos\vartheta_t}{n_1 \cos\vartheta_i + n_2 \cos\vartheta_t} A_{\perp} \tag{7.9}$$

Where, $T_{||}$, $T_{\perp}$, $R_{||}$, and $R_{\perp}$ are the transmitted and reflected amplitudes of the wave, with the electric field parallel (TM), perpendicular (TE), respectively, θ_i and θ_t are the angles of incidence externally and internally, respectively. To obtain reflectivity and transmissivity from the above equations, the following relations are used:

$$\rho = |R|^2 / |A|^2 \tag{7.10}$$

$$\tau = \{(n_2\cos\theta_t)/(n_1\cos\theta_i)\} \; |T|^2 / |A|^2 \tag{7.11}$$

regardless of the polarization component. n_2 is the refractive index of the sample or the penetrated material, and n_1 is the refractive index of the vacuum (air) or the medium of

incidence. In real situation where the electromagnetic wave is incident upon a medium with two surfaces, there will be multiple internal reflection effect. Assuming normal incidence and perfectly parallel planes that have exactly the same reflectivity and transmissivity as in Fig.53, we can proceed as follows:

Light incident on bottom plane is I_o, internally reflected rays from the top or bottom surfaces are referred to as $I_{1,2,...}$, any reflected intensities that exit the sample from the incident light side are referred to as $R_{1,2,...}$, and any transmitted intensities that exit the sample from the opposite side to the incident light side are referred to as $T_{1,2,...}$. In this case R will be the same as equation (3.5), and the true transmissivity is the same as equation (3.6) and is $t = e^{-\alpha d}$ where d is the sample thickness.

$$I_1 = I_o (1-R)t \tag{7.12}$$

$$I_2 = I_1 R t = I_o (1-R) t^2 R \tag{7.13}$$

$$I_3 = I_2 R t = I_o (1-R) t^3 R^2 \tag{7.14}$$

$$I_4 = I_3 R t = I_o (1-R) t^4 R^2 \tag{7.15}$$

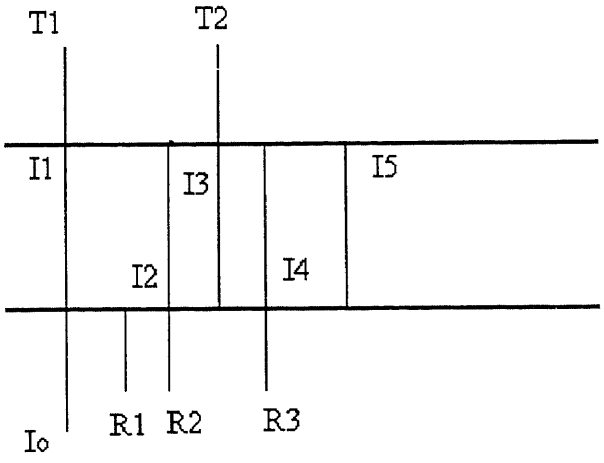

Fig.53 The effect of multiple internal reflections on the apparent reflectivity and transmissivity of a double-side polished specimen

$$I_5 = I_4Rt = I_o(1-R)t^5R^4 \tag{7.16}$$

Intensity returned	Intensity transmitted
$R_1 = I_oR$	$T_1 = I_1(1-R) = I_o(1-R)^2t$
$R_2 = I_2(1-R) = I_o(1-R)^2t^2R$	$T_2 = I_3(1-R) = I_o(1-R)^2t^3R^2$
$R_3 = I_4(1-R) = I_o(1-R)^2t^4R^3$	$T_3 = I_5(1-R) = I_o(1-R)^2t^5R^4$
$R_4 = I_6(1-R) = I_o(1-R)^2t^6R^5$	$T_4 = I_7(1-R) = I_o(1-R)^2t^7R^6$

Intensity returned: ρ^* = fraction of intensity returned from the light incident side,

$$\rho^*I_o = I_oR + I_2(1-R) + I_4(1-R) + I_6(1-R) + \ldots \tag{7.17}$$

$$\rho^*I_o = I_oR + I_o(1-R)^2t^2R + I_o(1-R)^2t^4R^3 + I_o(1-R)^2t^6R^5 \tag{7.18}$$

$$\rho^* = R + (1 - R)^2t^2R[1 + t^2R^2 + t^4R^4 + \ldots] \tag{7.19}$$

$$\rho^* = R + (1 - R)^2t^2R/(1 - t^2R^2) \tag{7.20}$$

$$\rho^* = (1 - t^2R^2)\text{-}1[R - t^2R^3 + (1 - R)^2t^2R] \tag{7.21}$$

$$\rho^* = (1 - t^2R^2)\text{-}1[R\text{-}t^2R^3 + t^2R + t^2R^3 - 2t^2R^2] \tag{7.21}$$

$$\rho^* = R\{1 + t^2 - 2t^2R\}/(1\text{-}t^2R^2) = R\{1 + [t^2 - 2t^2 + t^2R^2]/(1 - t^2R^2)\} \tag{7.22}$$

$$\rho^* = R\{1 + t^2(1 - R)^2/(1 - t^2R^2)\} \tag{7.23}$$

which is the same as equation (3.9) or apparent reflectivity. Now for the total transmitted intensity: τ^* = fraction transmitted from the side opponent to the light incident side.

$$\tau^*I_o = T_1 + T_2 + T_3 + \ldots \tag{7.24}$$

$$\tau^*I_o = I_1(1 - R) + I_3(1 - R) + I_5(1 - R) + \ldots \tag{7.25}$$

$$\tau^*I_o = (1 - R)[I_1 + I_3 + I_5 + \ldots] \tag{7.26}$$

$$\tau^*I_o = (1 - R)[I_o(1 - R)t + I_o(1 - R)t^3R^2 + I_o(1 - R)t^5R^4 + \ldots] \tag{7.27}$$

$$\tau^* = (1 - R)^2 t[1 + t^2R^2 + t^4R^4] \quad (7.28)$$

$$\tau^* = (1 - R)^2 t/(1 - t^2R^2) = (1 - R)^2 t/(1 - t^2R^2) \quad (7.29)$$

which is the same as equation (3.8). Using equation (3.10) and substituting for τ^* and ρ^* leads to:

$$\varepsilon = 1 - R\,[1 + t^2 - 2t^2R]/(1 - t^2R^2) - (1 - R)^2 t/(1 - t^2R^2) \quad (7.30)$$

$$\varepsilon = \{1 - t^2R^2 - R - Rt^2 + 2t^2R^2 - t + 2tR - tR^2\}/(1 - t^2R^2) \quad (7.31)$$

$$\varepsilon = \{1 - R - t^2R(1 - R) - (1 - R)^2 t\}/(1 - t^2R^2) \quad (7.32)$$

$$\varepsilon = (1 - R)\,\{1 - t^2R - (1 - R)t\}/(1 - t^2R^2) \quad (7.33)$$

$$\varepsilon = (1 - R)\,\{(1 + tR)(1 - t)/(1 + tR)(1 - tR)\} \quad (7.34)$$

$$\varepsilon = (1 - R)(1 - t)/(1 - tR) \quad (7.35)$$

which is the same as equation (3.4). For single layer structure, the above equations would be sufficient to obtain the optical properties. For two or more layers, however, the problem gets more complicated, and the theory of thin films coatings can be used [122,123]. The easiest approach is to find the relation between the tangential electric and magnetic fields at the two interfaces of each film [31]. The result has been found to fit in a matrix form by the pioneering work of Abeles [121]. For the film m in a multi-layer structure, the matrix form follows [31,121] as:

$$\begin{pmatrix} E_I \\ H_I \end{pmatrix} = \begin{pmatrix} \cos\delta_m & -i\sin\delta_m / \gamma_m \\ -i\gamma_m \sin\delta_m & \cos\delta_m \end{pmatrix} \begin{pmatrix} E_{II} \\ H_{II} \end{pmatrix} \quad (7.36)$$

where δ_m is the phase difference:

$$\delta_m = 2\pi n_m d_m \cos\theta_m/\lambda \quad (7.37)$$

γ_m is a function of the polarization. For (TE) or s-polarization:

$$\gamma_m = n_m \cos\theta_m / Z_o \tag{7.38}$$

and for (TM) or p-polarization:

$$\gamma_m = n_m / Z_o \cos\theta_m \tag{7.39}$$

where Z_o is the air impedance, approximately 377Ω, [31].

Considering a wafer with more than one layer on top of it, the use of the matrix form will prove to be helpful. The full stack of layers will be represented by one characteristic matrix that is a product of the multiplication of each layer's characteristic matrix. A detailed explanation on the approach to the matrix theory can be found in Moller's "Optics" [124]. The next step is to utilize the matrix form in generating the true reflectivity and transmissivity directly from Fresnel's formulae, equations (7.6)-(7.9), and then relating them to equations (7.10) and (7.11). This results in:

$$\rho = \left| \frac{(m_{11} + \gamma_{sub} m_{12})\gamma_0 - m_{21} - \gamma_{sub} m_{22}}{(m_{11} + \gamma_{sub} m_{12})\gamma_0 + m_{21} + \gamma_{sub} m_{22}} \right|^2 \tag{7.40}$$

$$\tau = \frac{4\,\mathrm{Re}(\gamma_0)\,\mathrm{Re}(\gamma_{sub})}{\left|(m_{11} + \gamma_{sub} m_{12})\gamma_0 + m_{21} + \gamma_{sub} m_{22}\right|^2} \tag{7.41}$$

where γ_{sub} could be for TE or TM, but cannot be representing both of them, and sub represents the substrate value, while γ_o is for the medium of incidence. Fitting this in equations (3.8) and (3.9) results in the apparent reflectivity and transmissivity for the whole stack. It is important to note that the validity of equations (7.40) and (7.41) is restricted to non-absorbing medium of incidence. This is because of the difficulties arising from the coupling between incident and reflected fields in an absorbing medium. For RTP purposes, however, it turns out that n>>k for the substrate minimizing the error in treating

the substrate as transparent and applying equations (7.40) and (7.41) when the transmission of light through the substrate is significant.

Intrinsic Emissivity:

Absorption in silicon (of special interest) or any other semiconductor can be divided into four regions:

- Above fundamental edge 0.4-0.8μm: here the photon energy is high and no thin transmittive films can be produced. If a model is needed for this region, the transmissivity can be ignored even at low temperatures, and equation (3.7) can be used after modeling for reflectivity.
- Fundamental edge 0.8-1.1μm: Absorption is also very high in this region. Applied Materials uses this region, 0.95, for their choice of wavelength for the pyrometer, to avoid having to deal with transmissivity. For silicon the absorption edge has been observed to decrease with the increase in temperature and pressure, $dE_G/dT = -2.8\times10^{-4}$ and $dE_G/dp = -1.5\times10^{-6}$eV/ bar [125]. The temperature dependence of the absorption edge was shown in Fig.19, where the strong absorption at short wavelengths, before the free carrier absorption, shifts towards longer wavelengths or towards decreased photon energies reflecting a decrease in the bandgap with temperature. Modeling for the fundamental absorption is a tedious task. The work of Macfarlane et al. on the temperature dependence of the absorption edge of silicon at temperature between 4.2 and 415K and wavelength region between ~0.95-1.35μm have resulted in a semi-empirical model [126,127].
- Free-Carrier absorption: This has been discussed thoroughly in chapter 5.
- Lattice vibration: This absorption occurs in the mid-IR, i.e. > 6μm. In any spectral

analysis of emissivity around this range and at relatively low temperatures the effect due to lattice vibration would dominate and will be in the form of structure superimposed on free-carrier absorption. At high temperatures, absorption due to lattice vibration is masked by the immense effect of free-carriers at the same region.

7.3 Available Models

Surveying optics, we find that the relations that define and predict the optical properties of a given slab of material have been known and documented for a long time. It started with the (a) Fresnel's equations that enabled the calculation of the reflected and transmitted amplitudes at a certain boundary for two different polarizations (TM and TE), (b) Maxwell's equations that describes the electric and magnetic fields associated with the wave, (c) Abeles's [128] hypothesis of the matrix method and the characteristic matrix of substrate or stack of substrate and thin films which is convenient for calculation purposes, and finally (d) Jacobsson's study [129] of media with continuous varying refractive index. The only obstacle that the optical models have to overcome currently is in predicting the behavior of surface roughness, particularly extreme degrees of roughness at low temperatures as was shown in chapter 5. Thus, in theory, with the available models in the literature, predicting the optical behavior should be possible. But this is not the case because of the lack of complete knowledge of the bulk properties of silicon such as the refractive index n and extinction coefficient k. In an attempt to close the loop over this subject, models and software packages that treat the optical properties have been proposed by several groups. One such model was put forward by Fiory [130,33]. It uses

the basic equations for apparent reflectivity. Wavelength range of 0.3 - 0 5μm is covered and constant values of n and k are used. It also utilizes the Abeles matrix theory in treating more than one layer. The attenuation is assumed to be high due to an infinite substrate. This model has some limitations especially at wavelengths above 1.2μm, where the transmissivity of silicon cannot be ignored. The model has been extensively utilized to study the effect of dielectrics, such as SiO_2 and Si_3N_4. For Si_3N_4 calculated values of refractive indices as in Fig.40 were used in the permitted range of wavelengths to generate the emissivity results of poly-Si/Si_3N_4/Si. The emissivity values of poly-Si/SiO_2/Si and poly-Si/Si_3N_4/Si as function of the poly-Si thickness at four different wavelength are shown in Figs.54 and 55 [33]. A model, that uses Mathcad based codes, has been supplied by Applied Materials. This model ignores the transmissivity of silicon and works in a manner similar to Fiory's model. The maximum number of layers that can be handled by this model is three layers, contrary to the ability of the previous model of handling more layers. FTG is a commercially available model. Here transmittance is calculated based on equations (3.8) and (7.41). It is an interactive model that can be interfaced with optical constants at the shortest wavelength range possible. The only limitation here is in determining the temperature dependent optical constants. This is indeed a gray area, in the sense that not much is known in the literature about high temperature values of n and especially k. Fig.56 shows a simulation of the reflectance and transmittance of SIMOX. It shows good agreement at low temperatures with the experimental data except for the region where the fundamental edge absorption occurs. The reason is that the high value of the extinction coefficient in this region are not considered by the model in its

present form. The Multi-Rad model proposed by MIT/SEMATECH is a very sophisticated model that can handle the spectral optical properties as well as the total absorption, reflection and transmission. As seen earlier in chapter 5, this model utilizes the Drude approximation to determine the effects of doping and temperature on the optical constants n and k. The model also utilizes the n values reported by Magunov [57] and relates the Drude model results to those obtained by Sturm, Timans and Vandenabeele and Maex [75,78,63]. The model utilizes the best known k values, reported by Sato [28], in the lattice vibration region or $\lambda>6\mu m$, and the Macfarlane numerical model at the fundamental absorption region or $\lambda<1.15\mu m$. Fig.57 shows a comparison between the Multi-Rad simulated and measured optical properties of a single-side polished 700μm Si/ 1600A SiO_2/ 700A Si control wafer. It can be seen from this figure that the disagreement between the room temperature simulated optical properties and the measured properties are due mainly to the surface roughness. Finally, the NREL/Sopori PV-Optics model, as mentioned in chapter 5, is the most extensive model that treats non-planar surfaces from 0.4-1.2μm. Beside using general optics rules, the model also utilizes the known optical constants n and k obtained from different sources for various temperatures and doping concentrations. It also does tedious calculations that resemble the Monte-carlo simulations for individual rays of light incident on planar or non-planar surfaces. The model is currently being extended to include the mid-IR. Figs.58 and 59 display the abilities of the model in distinguishing between smooth side incidence versus rough side incidence. From all of the above, it is clear that the optical models found in the literature can indeed predict the response of the materials under study if and only if the material constants are known to

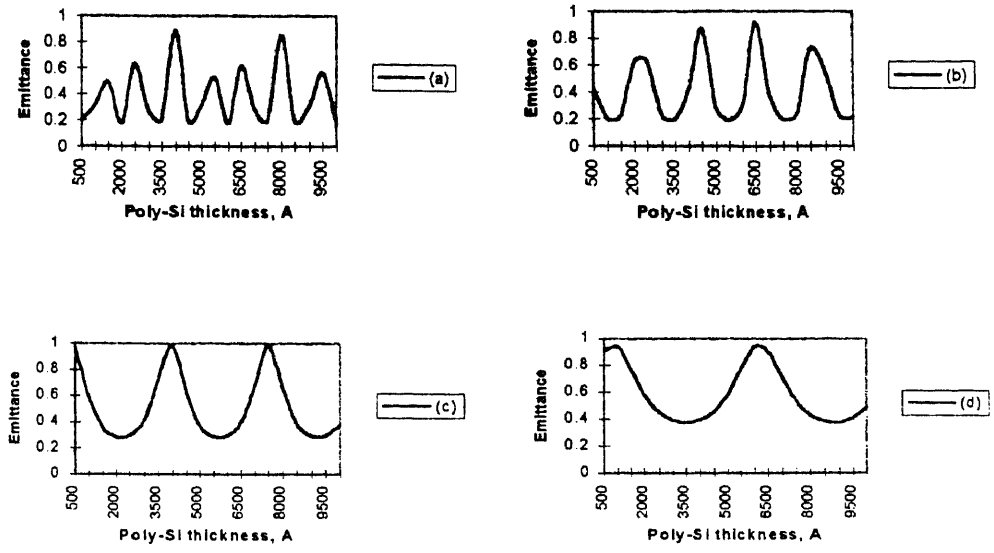

Fig.54 Simulated emissivity as function of poly-Si thickness for poly-Si/SiO_2/Si, oxide thickness = 2000A for: a) 0.95, b) 1.53, c) 2.5 and d) 3.8μm

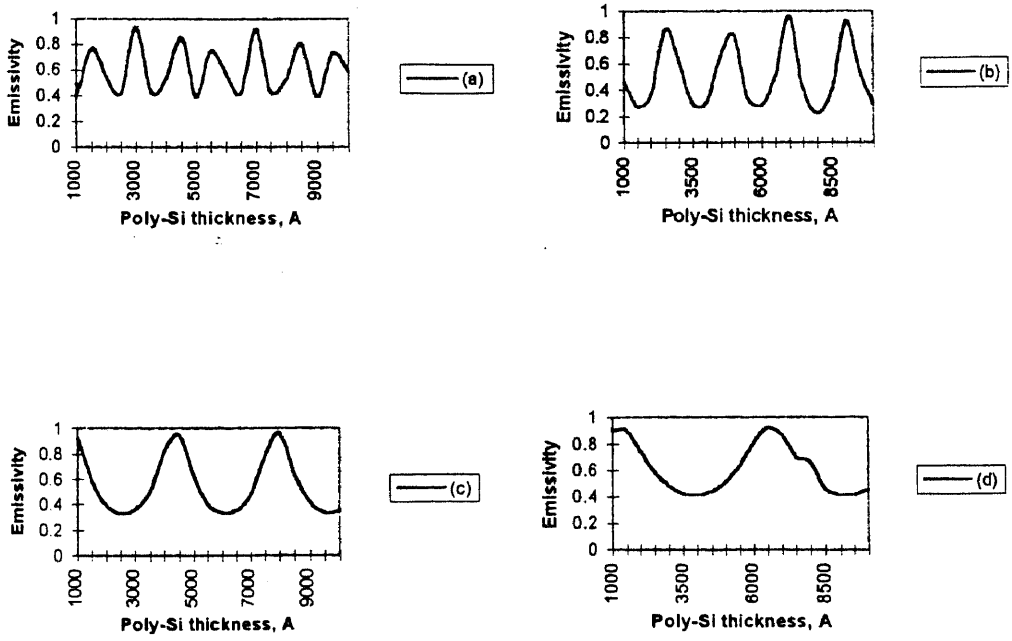

Fig.55 Simulated emissivity as function of poly-Si thickness for poly-Si/Si_3N_4/Si, nitride thickness = 2000A for: a) 0.95, b) 1.53, c) 2.5 and d) 3.8μm

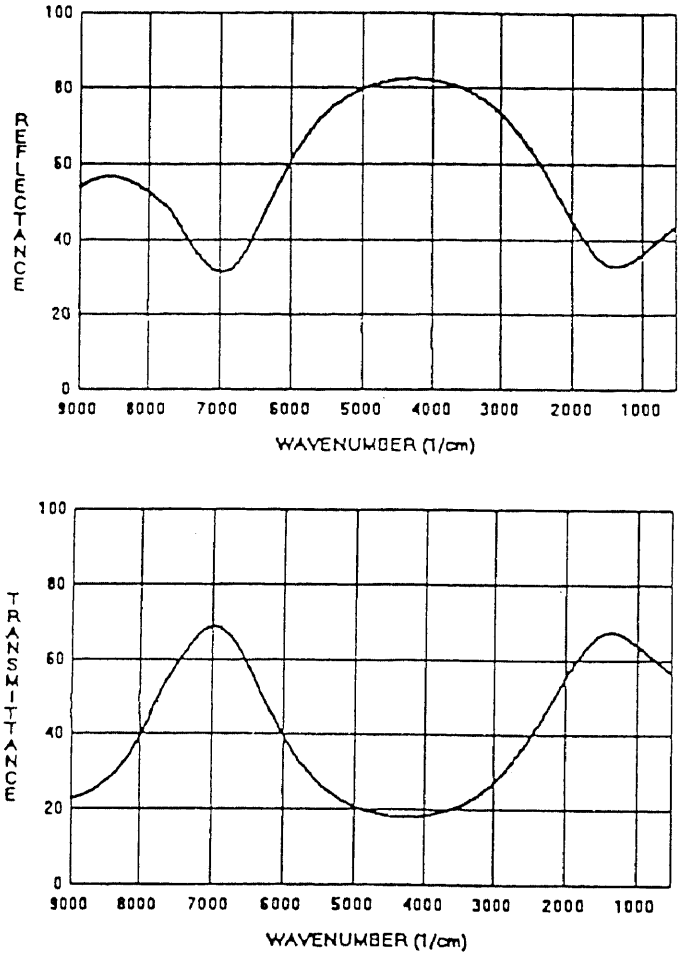

Fig.56 Simulated (a) reflectance and (b) transmittance of SIMOX at room temperature

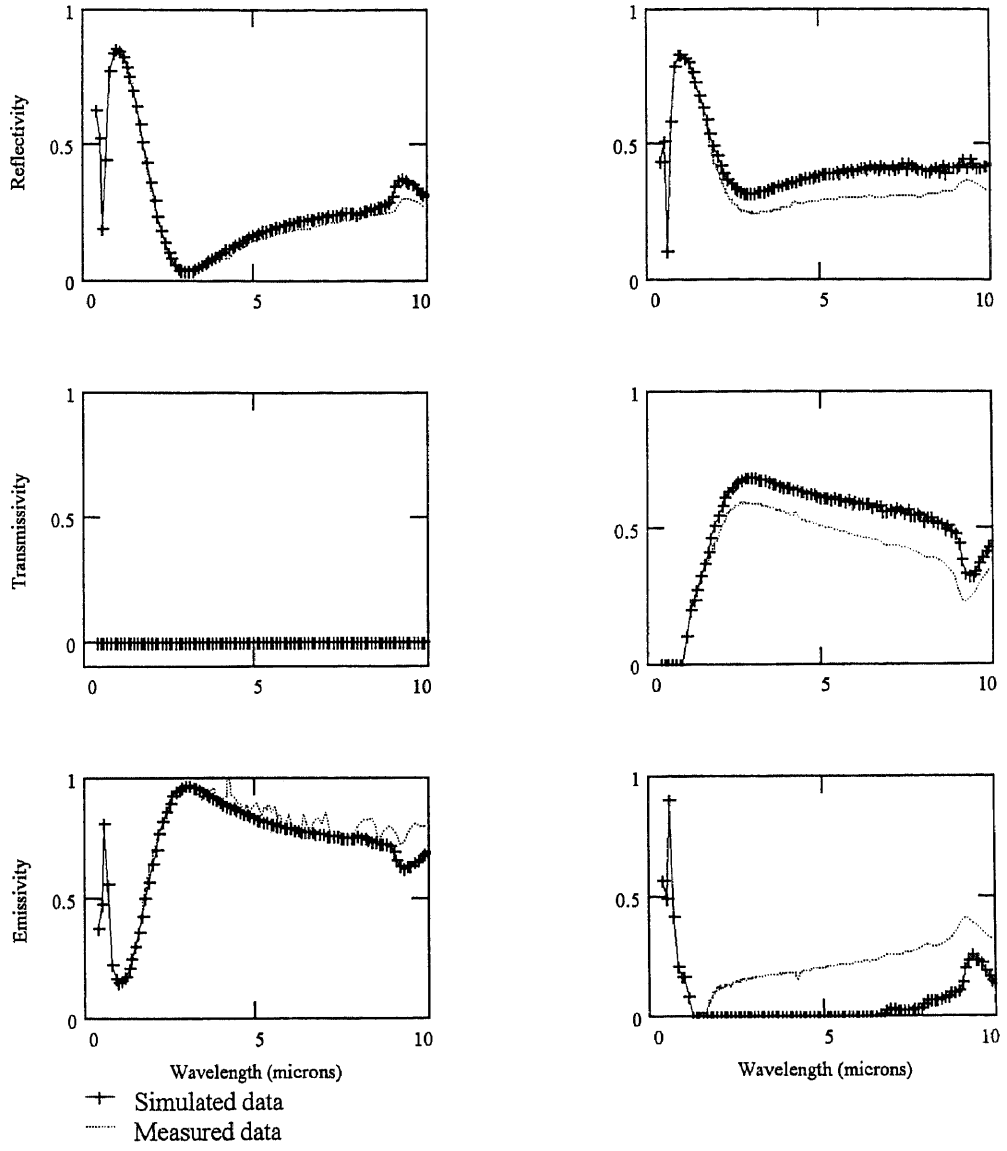

Fig.57 Comparison between simulated and measured optical properties of a control wafer: 700μm Si/ 1600A SiO_2/ 700A Si, at (a) 809 and (b) 38°C

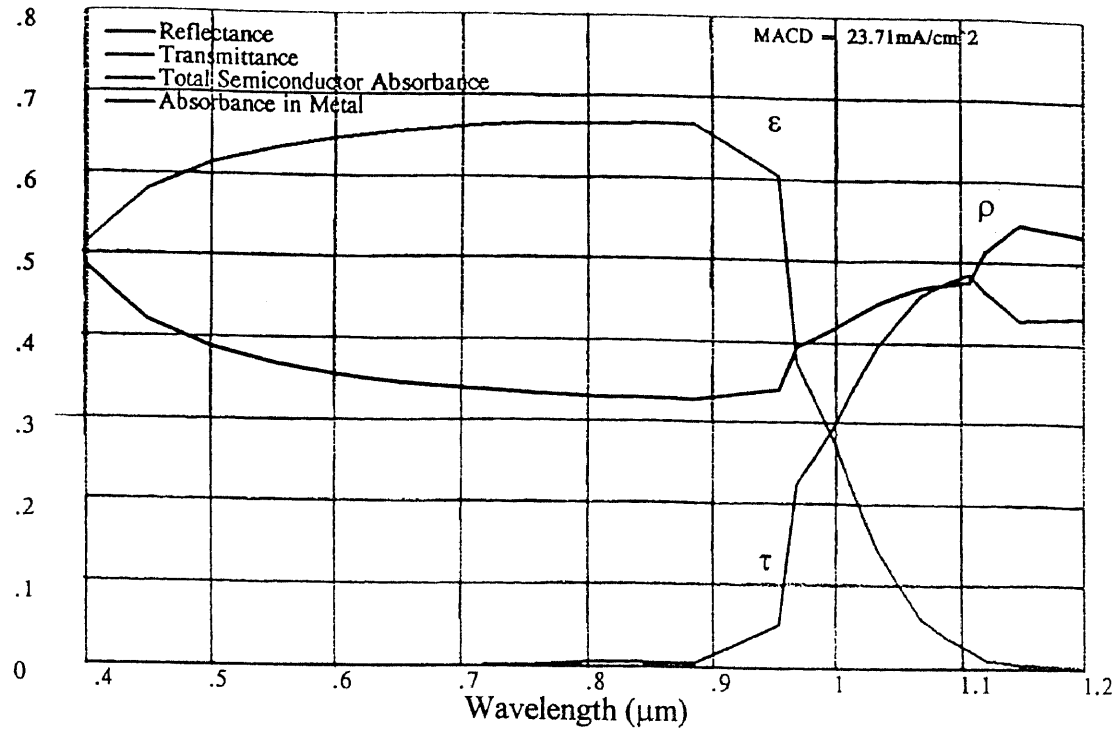

Fig.58 Simulation of the optical properties of a single-side polished 20μm Si, with the incidence on the smooth side, assuming a constant angle between the grooves = 70.2°

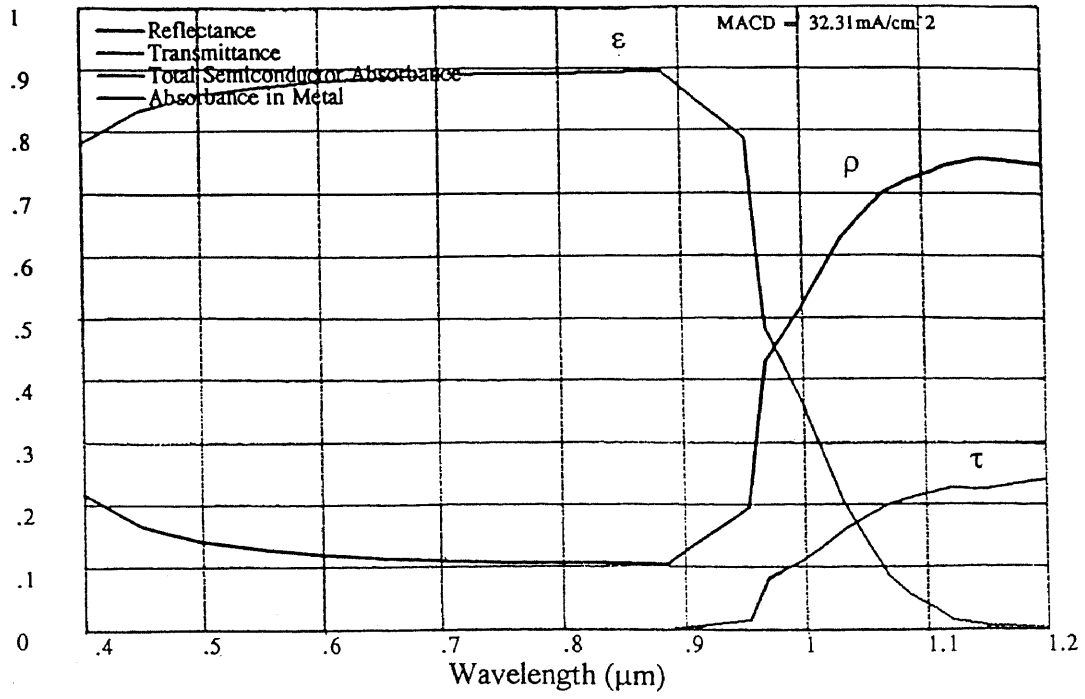

Fig.59 Simulation of the optical properties of a single-side polished 20μm Si sample with the incidence on the rough side, assuming a constant angle between the grooves = 70.2°

a high accuracy at low and high temperatures and the surface effects are compensated for. The most severe limitation lies in the short range of wavelengths due to lack of data. The spectral emissometer described in this work has indeed been able to fill the void in being able to generate experimental data of these optical constants as function of wavelength and temperature.

CHAPTER 8

WAFER EMISSIVITY INDEPENDENT TEMPERATURE MEASUREMENT TECHNIQUES

It has been demonstrated in the preceding chapters that the detected radiation of a sample in an RTP chamber by a pyrometer is a function of the layers on top of the substrate and the surroundings and chamber components. The resultant emissivity is referred to as effective emissivity. Changes in thickness of thin films on top of the wafer as well as the reflective interior of the RTP chamber can indeed cause a large error in temperature determination as was found by Pettibone et al. [34]. Moreover, it is important in an industrial environment to establish a reliable and reproducible in-situ monitoring technique associated with a steady and wafer independent recipe for the process. As explained thoroughly in a joint paper between AMD and STEAG-AST [131], wafers tested with mid-IR operating pyrometer (2.8μm) show a variation of more than 50°C from run to run depending on the backside roughness and history of the wafer. According to the current sets of standards followed by the industry and instructed by the National Technology Roadmap for Semiconductor (NTRS) [5] such temperatures differences which lead to large non-uniformities in dopant distribution and film thickness are not tolerable. For this reason the RTP industry has initiated some alternatives in non-contact temperature determination. These suggested techniques still utilize pyrometry and radiation detection as the temperature monitoring tool. They do, however, enhance or stabilize the emissivity independence of the starting wafer and in some cases of the layers deposited or grown on

the wafer. In this chapter, a survey of some of the most innovative and promising techniques proposed and experimented by some of the industry leaders are reported.

8.1 Hotliner

The Hotliner is the sample of choice considered in this section. The composition of the Hotliner is as follows: 57nm Si_3N_4/25nm SiO_2/700μm p-Si/25nm SiO_2/57nm Si_3N_4. The substrate is heavily boron doped <100> CZ-Si, > $1\times10^{19}cm^{-3}$, with resistivity ρ = $0.001\Omega.cm^{-1}$. The oxide is grown thermally and the nitride was deposited using LPCVD. As explained in chapter 5.3, at such high doping concentrations, the wafer becomes opaque and the emissivity of silicon is expected to saturate at the gray body level of 0.7. It is expected also that such levels of doping and rms industrial surface roughness of the order of ~1μm will have minimal effect on the radiative properties due to the opaqueness of the wafer. The radiative properties of this wafer have been studied using the spectral emissometer at temperatures ranging from 155-954°C from the front and the backside incidence. Figs.60(a)-60(c) show the smooth side incidence measured reflectivity, transmissivity and emissivity of the Hotliner at three different temperatures. As can be seen in these figures, the emissivity of the Hotliner is high in the entire spectrum considered, i.e. 1-20μm, with an average value >0.71. To verify the above statement on the effect of roughness in the case of this sample, the rough incidence optical properties of the Hotliner are reported in Fig.61. As can be seen in the figure, a slight increase in emissivity over that when the incidence is on the smooth side on the account of reflectivity is noticed. The high doping in the substrate enhances the absorption mechanism at three

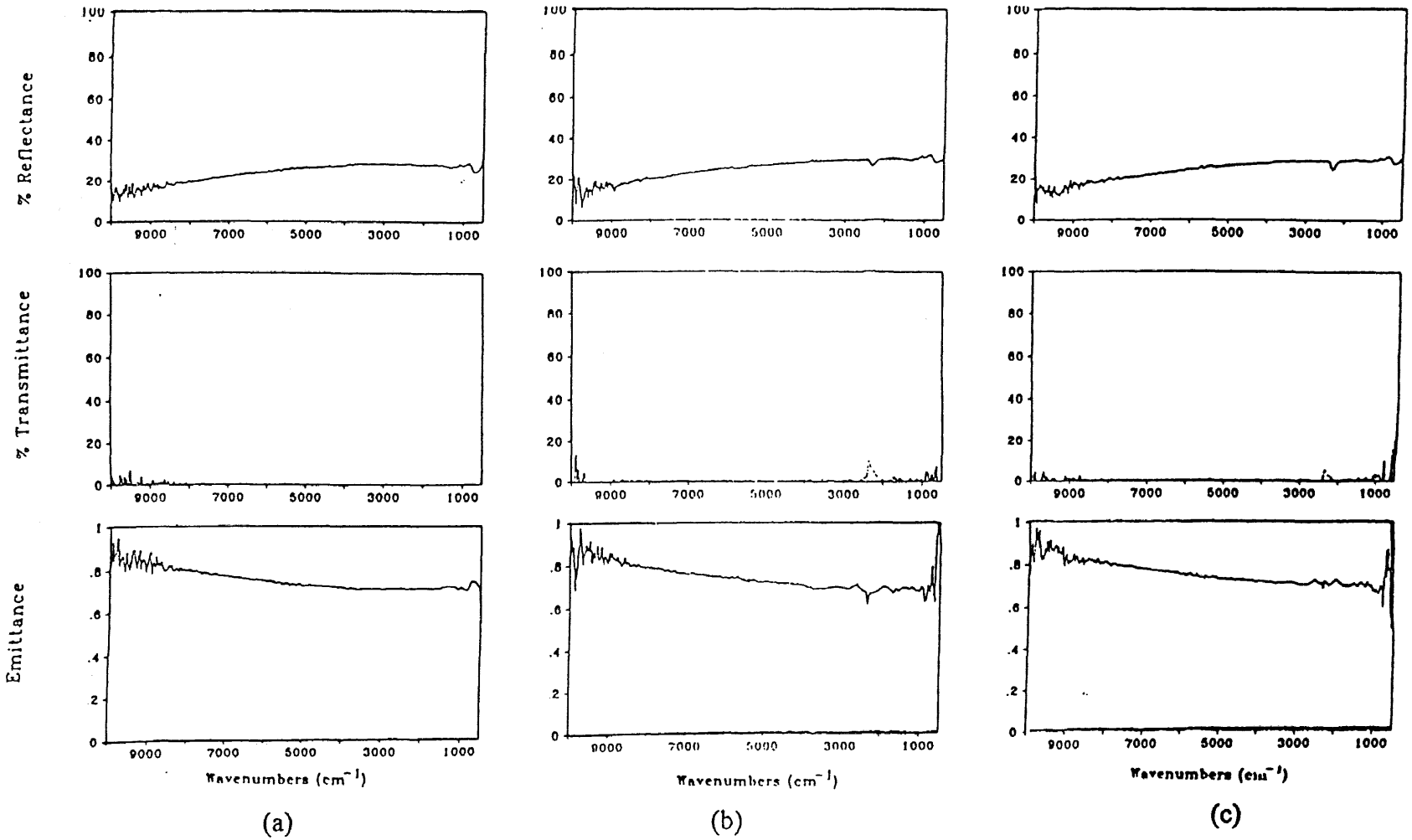

Fig.60 Experimental Optical Properties of the smooth front side of the Hotliner at three different temperatures: (a) 155, (b) 565 and (c) 954°C.

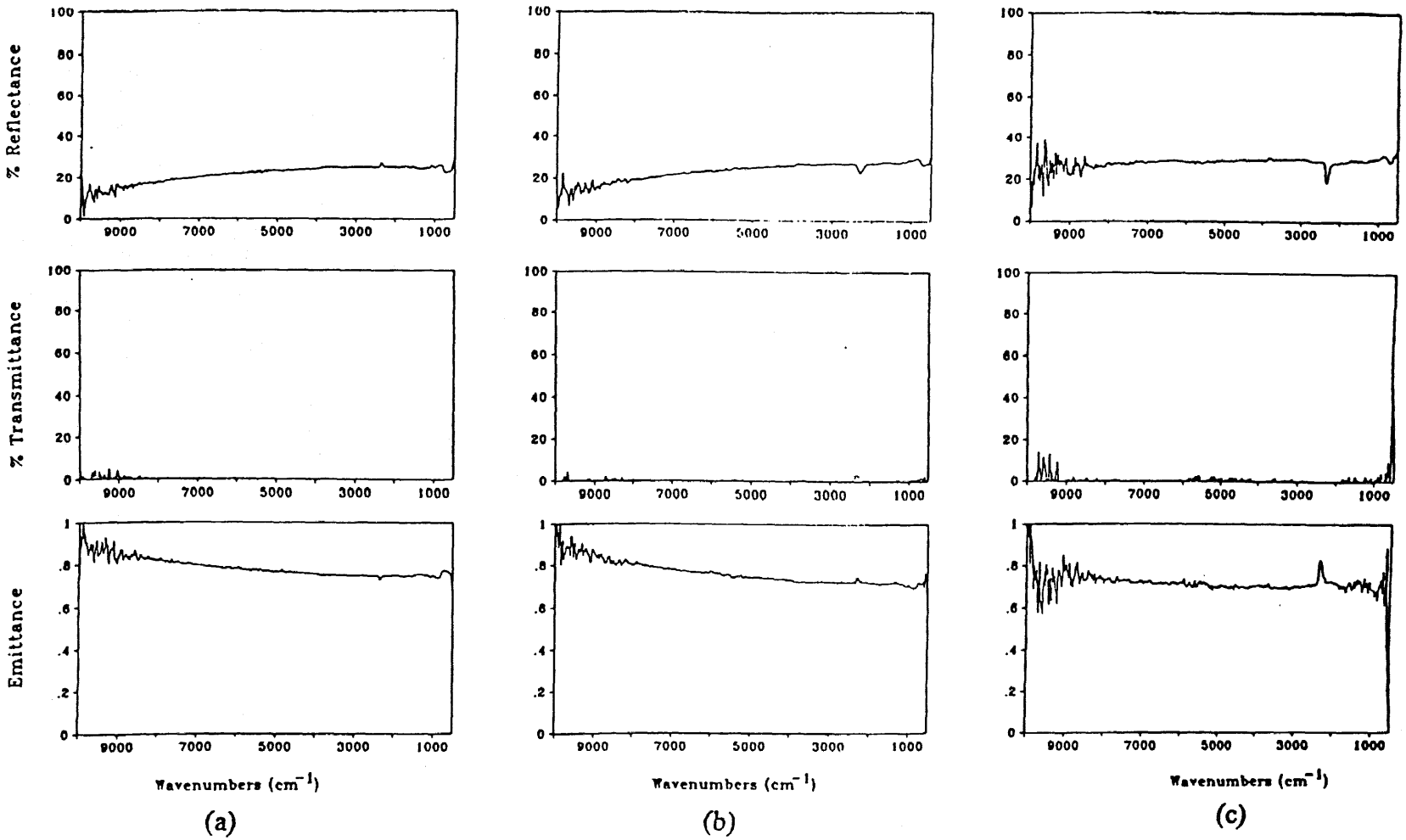

Fig.61 Experimental optical properties of the backside of the Hotliner at three different temperatures: (a) 142, (b) 563, (c) 942°C

regions. These regions comprise of (a) the band gap reduced by doping to degeneracy [125], (b) the impurity region from 1.13-1.5μm and (c) the free carrier region from 1.5-20μm.

The effect of coatings on the heavily doped silicon in the Hotliner is very minimal. It is expected to enhance the emissivity by a very small fraction. This is because of the smaller refractive index for both the oxide and the nitride as compared with silicon. The presence of thin layers leads to decrease in reflectivity at the surface of the two dielectrics and increases the absorption in the bulk of the silicon substrate. The function of coatings is to form a buffer layer and a protective shield for the silicon substrate when placed inside the STEAG-AST Electronic RTP chamber. Indeed, the purpose of this highly emissive Hotliner is to become a stable part of the processing chamber that is situated beneath the processed wafer facing the pyrometer. Its presence is to enable a wafer emissivity independent temperature measurement. It also enhances the emissivity of the process wafer in the RTP by being situated at a very short distance (<1cm) from the backside of the wafer resulting in a more efficient process. As can be seen in Fig.62, the pyrometer, operating at 2.8μm, is situated behind the gold chamber, the bottom lamps, the quartz, and the Hotliner. Thus, it is important that the Hotliner be protected from various effects of processes such as annealing, oxidation etc. A thin nitride layer is deposited to from a diffusion barrier to oxidation. In order to improve the adhesion of the nitride to silicon, a thin layer of oxide is deposited between the nitride and the silicon substrate. It is expected that the Hotliner will last for > 100,000 process runs. Using the Hotliner as in Fig.62, with the pyrometer looking at the Hotliner backside instead of the wafer backside, allowed

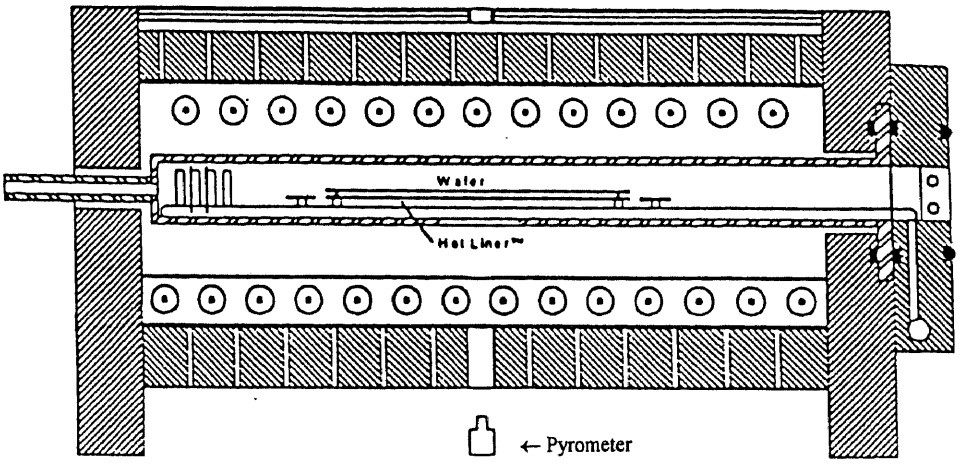

Fig.62 A view of the AST-RTP process chamber showing the pyrometer (at the bottom), lamps, quartz tube, wafer and the Hotliner (beneath the wafer)

a range of ±4°C from wafer to wafer. Hence the need was eliminated for a full calibration of each wafer to optimize for backside differences. At low temperatures a pyrometer looking at the backside of the wafer will be also looking at the heat source such as tungsten-halogen lamps. Due to the consequent interference effects, this causes an error in the temperature reading and hence causes difficulties in process control. This confirms the need of such technique for low temperatures applications of RTP. In their calibration [131], STEAG-AST and AMD, have used the conventional implant monitor wafers and a readily available four point probe metrology to optimize for the lamp correction tables. The results of uniformity across the wafer both during the ramping rate and the steady state has been very promising.

8.2 Modeling for the Hotliner

In this part of the study, Multi-Rad has been utilized extensively to analyze and simulate the experimentally obtained spectral properties acquired using the emissometer. To see the effect of the thin films on the overall emissivity of the Hotliner, the spectral properties of a highly doped p-type, 1.3×10^{19} cm^{-3}, silicon wafer has been simulated at 155°C. The result is shown in Fig.63(a). In this figure, the optical properties are overlaid in the same frame with the same scale. As can be seen in the figure, the results are in good agreement, qualitatively, with the experimental data of the Hotliner. In Fig.63(b) a simulation is made using the same silicon wafer with an oxide layer of 250A on the front side. The effect of the oxide is minimal. Fig.63(c) shows the results for nitride on top of the oxide, in other words, the Hotliner from one side. It can be seen that at the wavelength of interest in

the RTP chamber, i.e, 0.95-4.5μm, no interference effects are observed due to the very thin nature of the films on the silicon substrate. At shorter wavelengths of 0.6-0.7μm, the Hotliner shows high emissivity.

The effect of the changes in film thickness on the spectral properties is simulated in Fig.63(d). In this figure the thickness of the nitride and oxide is increased to 770A and 350A, respectively. As can be seen in this figure the peak at which the emissivity of the wafer is almost 1 moves to the right towards longer wavelength from 0.7μm to 0.9μm. This effect is due to changes in reflectivity of thin layers. It has been shown in previous studies [33,114] that constructive and destructive interferences caused by the dielectric layers affect the emissivity accordingly. It has also been shown that as the thickness of the dielectric increases, the emissivity peak shifts towards longer wavelengths.

8.3 Comparisons with Other Approaches

Low temperature measurements in RTP has proven to be problematic. The importance of low temperature processes for cluster-based tools has led to many innovative emissivity independent temperature measurement techniques. One such technique is the above mentioned STEAG-AST approach of the Hotliner approach. Other than having uniformity and repeatability, the Hotliner has the advantage of efficiency in heating the wafer in a blackbody (BB) cavity type from the backside. The Hotliner also has the advantage of a high and steady emissivity throughout the whole spectrum even at low temperatures, thus enabling the pyrometer to work at a very wide range of wavelengths. Another similar approach is the AG Associates approach. Their approach of an emissivity independent

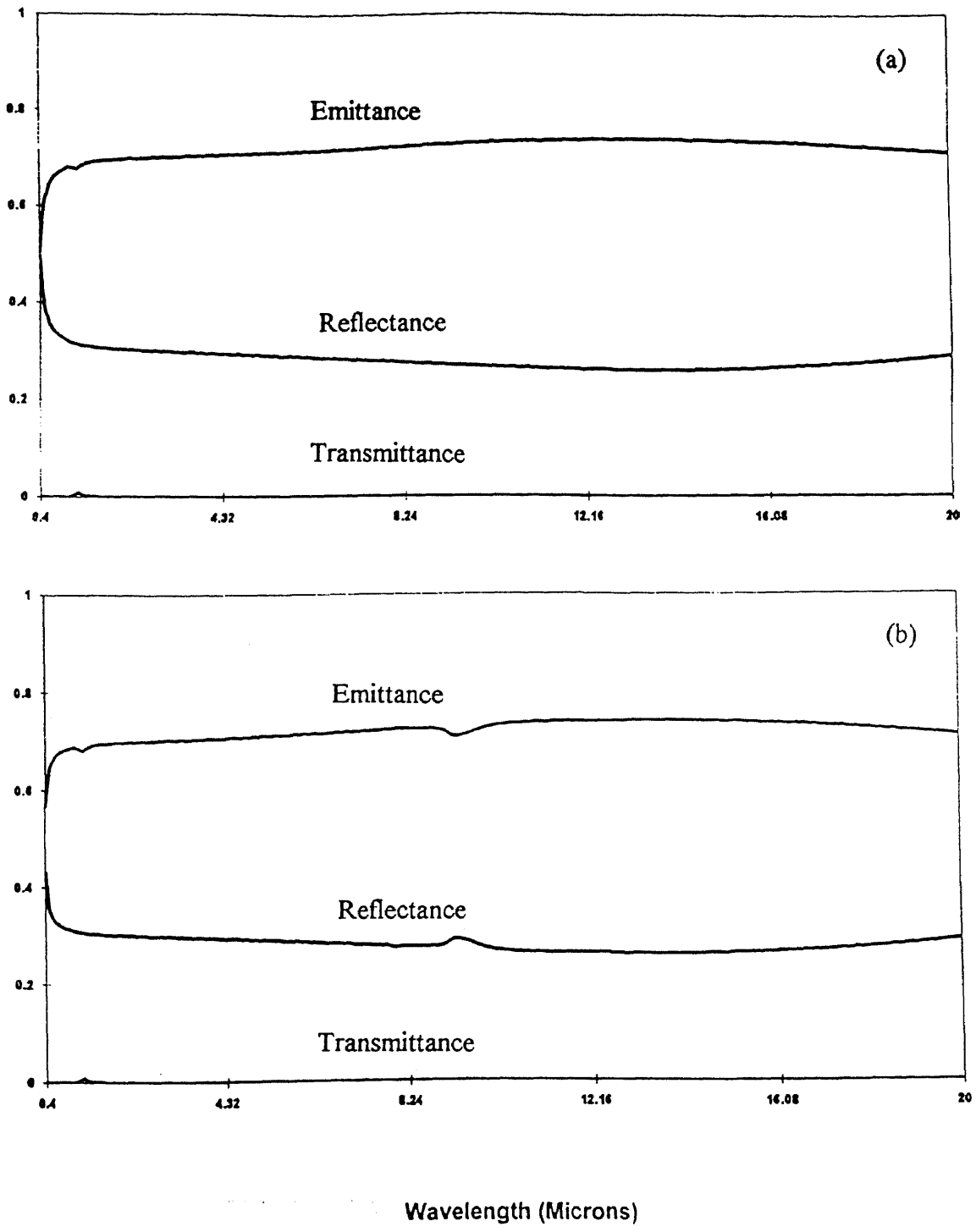

Fig.63 Simulated radiative properties of (a) heavily doped 700μm thick p-Si, $1.3\times10^{19}cm^{-3}$, and (b) 25 nm SiO_2/ 700μm p-Si, at 155°C

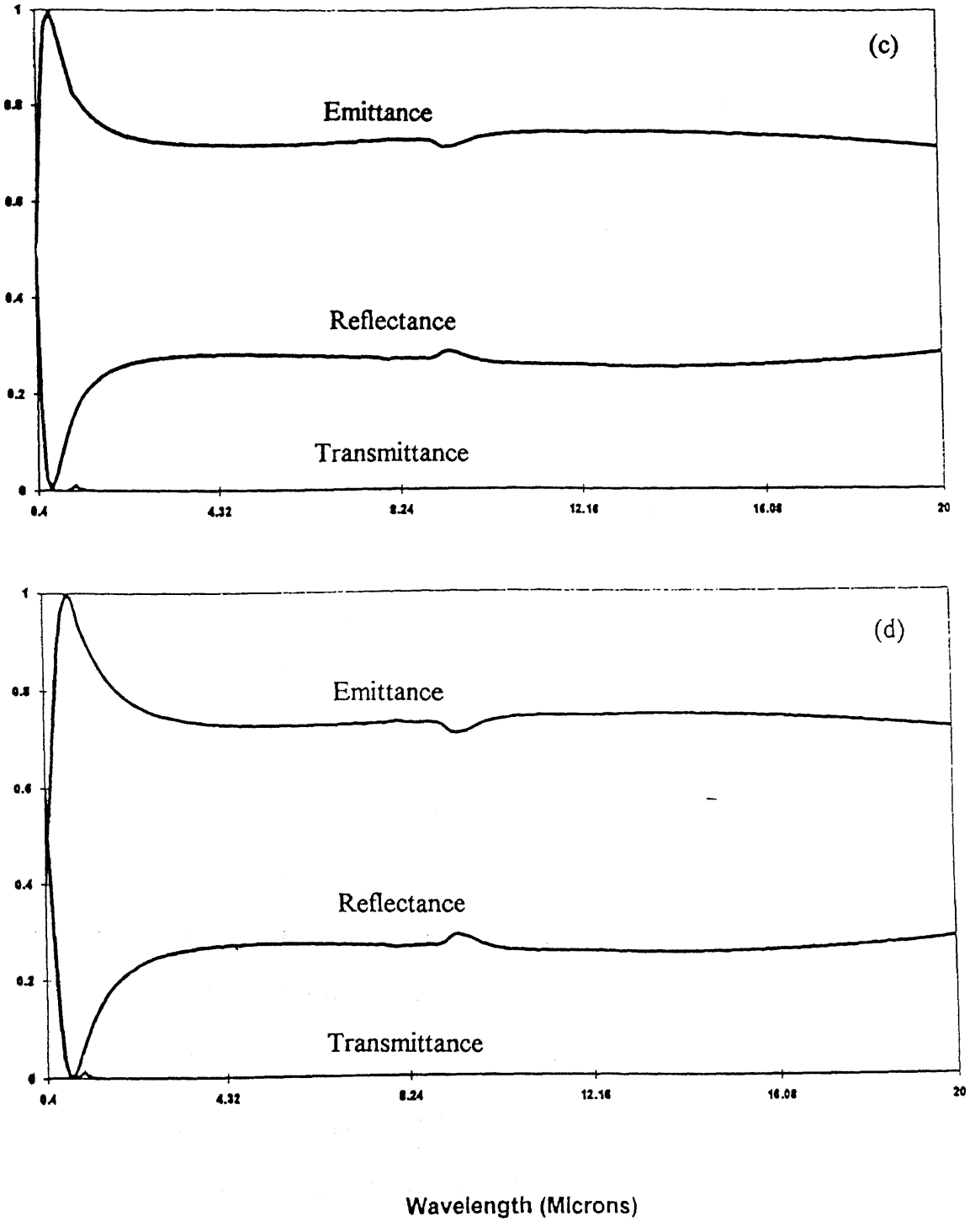

Fig.63 Simulated radiative properties of (c) 57nm Si_3N_4/ 25nm SiO_2/ 700μm p-Si, and (d) 77nm Si_3N_4/ 35nm SiO_2/ 700μm p-Si, at 155°C

temperature measurements, and the stages that led to it, is very simple and explained thoroughly in [132]. Here the chamber also has upper and lower lamps, and an opaque shield, referred to as hot plate, between the backside of the wafer and the lower lamps. Here the shield nature has not been conveyed, but again is treated as heavily doped silicon that has a net emissivity of 0.68. The manufacturers make the assumption that under a perfect match in the power supplied to the upper and lower lamps, or the power supplied to the top surface of the wafer and the bottom surface of the shield, the temperature determination for the wafer under process will be independent of the backside coatings of the wafer. This technique requires an open loop type of control. Assuming this perfect thermodynamically exchange of energy between the backside of the wafer and the top of the shield the temperature of the hotliner will determine the process wafer temperature. Thus, under these conditions a thermocouple can be used. However, as a dielectric like SiO_2 is thermally grown or another thin film is deposited in an RTCVD chamber on the top surface of the wafer thermodynamic equilibrium is upset tending to complicate the temperature measurements process. As a matter of fact, AMD and STEAG-AST have also mentioned that the Hotliner has improved the RTA process only. The influence of oxide growth (RTO) or deposition (RTCVD) has not been examined. Another approach by AG Israel [133], and Applied Materials (AMAT) has been to develop a perfect reflector. The AGI reflectors have two different shapes, planar mirror and a hemispherical one. The reflectors are capable of reaching a reflectivity of (>0.99) at a very narrow band at λ = 0.85μm. This technique utilizes the effective emissivity principle through enhancing the emissivity using a BB type cavity [14]. In this configuration, as the wafer is irradiated with

photon flux from lamps at both sides, it will absorb and emit an integrated radiance equivalent to:

$$M(T) = \sigma\varepsilon T^4 \tag{8.1}$$

where, σ is the Stefan-Boltzmann constant, ε is the emissivity of the wafer and T is the temperature of the wafer at that instant. After the first reflection from the perfect reflector situated beneath the wafer, the integrated radiance becomes:

$$M(T) = \sigma\varepsilon(1-a)T^4 \tag{8.2}$$

where, a is the fractional amount of light absorbed by the wafer. After n cycles of this reflection and radiation process, and applying Kirchoff's law as in equation (1), the light intensity emitted from the backside of the wafer becomes:

$$M(T) = \sigma\varepsilon[\textstyle\sum_{n=0\to\infty}(1-a)^n]T^4 = \sigma\varepsilon[\sum_{n=0\to\infty}(1-\varepsilon)^n]T^4 = \sigma\varepsilon_{eff}T^4 \tag{8.3}$$

As n approaches infinity, the effective emissivity becomes:

$$\varepsilon_{eff} = \varepsilon/[1-(1-\varepsilon)] = \varepsilon/\varepsilon = 1 \tag{8.4}$$

Thus, in theory, a very high and constant emissivity is achieved independent of the emissivity of the process wafer. It has been reported that in a range of $0.65 < \varepsilon_{eff} < 0.95$, the temperature reading is within $\pm 1°C$. This is indeed a great achievement. AGI has reported that they have calibrated their methodology using TC wafers up to 750°C and for RTCVD purposes, where very high temperatures may not be needed. The AMAT reflector is made of film stacks compatible with silicon processing. AMAT utilizes several pyrometers situated in small holes in the gold reflector and the process wafer is rotated to eliminate any effects on the pyrometer due to uneven distribution of the radiation. One concern about this technique and other such techniques is the edge of the process wafer.

At the edge the truly BB type cavity produced by the configurations discussed so far does not apply. Moreover, for device manufacturing purposes the edge of the wafer contributes to waste material. Despite the edge problem, AST and AMD have reported that these effects known as photon box during ramping up, and edge effect during steady state heating, were factored in the calibration technique and the results were very promising. From all of the above, it is clear that the industry is attempting to reach its goals and standards. It can be also concluded that pyrometry is still the solution for temperature monitoring but with innovative approaches.

CHAPTER 9

REMARKS

9.1 Limitations of the Emissometer

- In the spectral emissometer, the blackbody source (see Fig.1) is maintained at a constant operating temperature of 900°C. Wien's displacement law states:

$$\lambda_{max} = 2898 / T \qquad (9.1)$$

where T is the absolute temperature in Kelvin, and λ is the wavelength in microns corresponding to the peak of the blackbody. This is equivalent to $\lambda_{max} = 2.7\mu m$ at 900°C or 1173K. At wavelengths much shorter than λ_{max} the distribution falls off drastically. Thus, there is not enough signal at wavelengths less than 1.1μm for the Ge detector to operate efficiently. The solution for better operation may be in a) blackbody operating at a higher temperature, or b) a detector that operates more efficiently at near IR such as InGaAs or Si detector.

- The highest reliable temperature the emissometer can reach in theory is the temperature of the blackbody source, i.e. 900°C. This is because the sample's radiated signal will be higher than the calibration source and errors will be unavoidable in determining reflectivity, transmissivity and emissivity from equations (4.1) and (4.2). This can be explained as follows: The blackbody radiance at temperature T integrated over angle is according to Planck's law:

$$R_{bb}(T) = C_1/\lambda^5 \exp(C_2/\lambda T - 1) \qquad (9.2)$$

in units of W/m^2 per 1μm wavelength interval where λ is the wavelength (μm), $C_1 = 3.7404\times10^8\ Wm^{-2}\mu m^4$, and $C_2 = 14384\ K\mu m$. As the temperature of the sample increases

above 1173K, its radiance according to equation (4.5) $R_v^b(T)$ increases rapidly and $R_v(T)$ in equation (4.1) approaches M_o in equation (4.2) simply because the signal due to $\rho_v(T)R_v^b(T_{bb})$ in equation (4.2) becomes small compared to $R_v(T)$ as shown in Fig.64. Fig.64 shows the decreasing differences between equations (4.1) and (4.2) at many regions of the wavelength considered (1-10μm).

- The heating method used currently is propane/oxy-acetylene. It is difficult to control the sample temperature. The use of flames is not a clean process and is not compatible with the requirements of the IC industry. On the other hand, it is easy to calibrate for the contribution of the flames in the IR spectra, such as CO_2 and H_2O. These contributions have clear IR signatures at 2400cm^{-1} for CO_2 and at 1600 and 3500 cm^{-1} for H_2O.
- MCT detector, which needs to be cooled by liquid N_2 continuously, needs to be recalibrated and vacuum sealed every 1-2 years. Otherwise, water molecules contaminate the dewar leading to enhanced absorption for wavelengths greater than 1.6μm onward.
- Finally, at extreme samples roughness the radiative properties may be affected strongly especially for temperatures below the opacity of the sample.

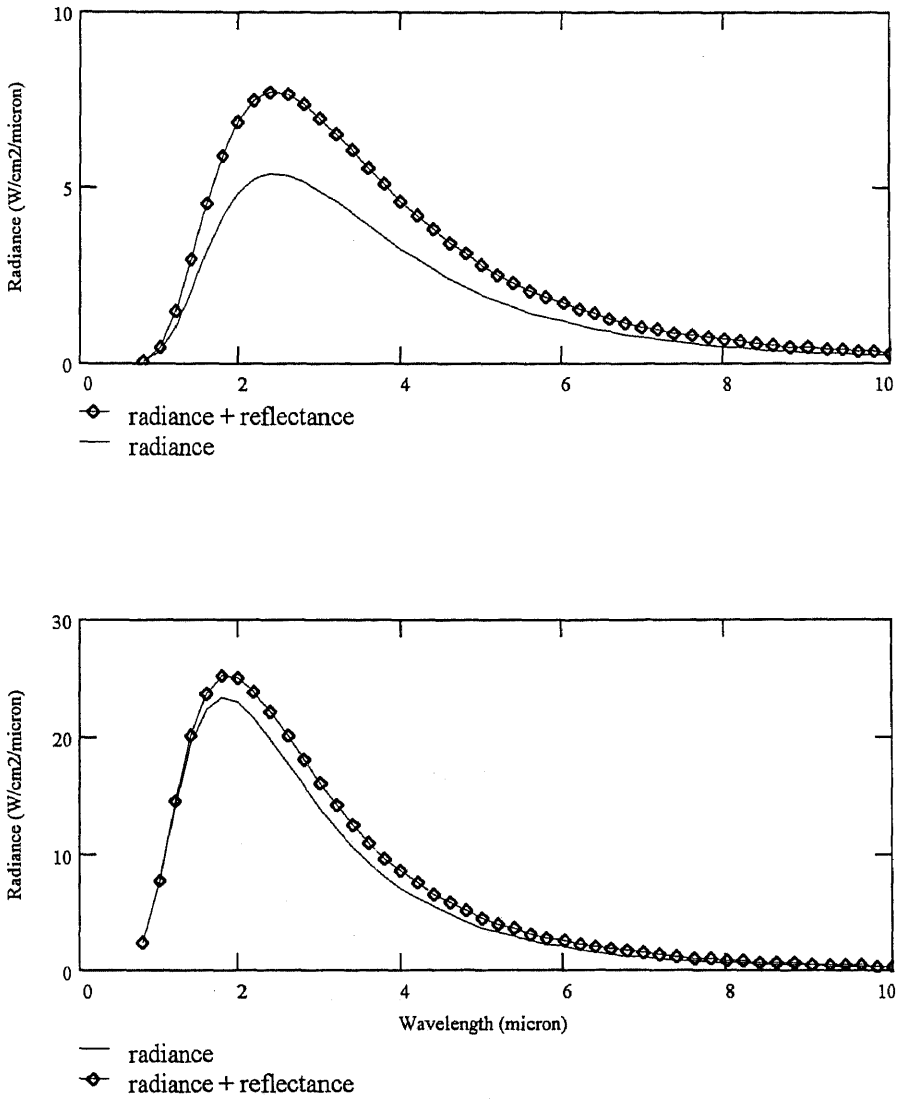

Fig.64 Comparison between radiance ($R_v(T)$) and radiance + reflectance ($R_v(T) + \rho R_{bb}(900)$) of a silicon wafer for a) 900°C and b) 1300°C

CHAPTER 10

CONCLUSIONS AND FUTURE WORK

10.1 Conclusions

The detailed study of the emissivity measurements and modeling of silicon related materials and structures presented in this work leads to the following conclusions:

- Comparative analysis of the various temperature measurement techniques available to the silicon industry leads to defining pyrometry as the tool for non-contact temperature monitoring in RTP.
- Spectral emissometery is established as the methodology to measure simultaneously the reflectance, transmittance and emittance of silicon and silicon related structures as function of temperature and wavelength.
- The first detailed study of the optical properties of a) single versus double-side polished silicon wafers and b) front-smooth versus back-rough sides of the same single-side polished wafer has been performed. The Vandenabeele-Maex (VM) one-parameter model has been utilized extensively to analyze the experimental data. The model is an attempt to extend the principles of optics that are applicable to the case of double-side polished wafers and has proven to be inaccurate in particular when applied to rough-side incidence of a single-side polished wafer.
- Measured optical properties have been deconvoluted to yield the absorption coefficient α as function of wavelength (free carrier range or 1-10μm), temperature, doping concentration for p-Si. The Multi-Rad model, developed by MIT/SEMATECH,

has been utilized extensively to compare the available knowledge in simulating the absorption coefficient α with that obtained experimentally. This comparison has proved that the current knowledge of bulk silicon optical constants is not sufficient for our present needs. The modeled α has higher values in n-Si and lower values in p-Si than the measured α. The model is based on the Drude approximation and a λ^2 dependence for the free carrier absorption. It does not account for the conduction intraband transition observed in n-Si in the range of 1.6-5μm. The study has also proved that even for p-Si, in the intrinsic regime, silicon still exhibits a conduction intraband transition. To the best of our knowledge, this is the first time that high temperature observations of this phenomenon have been reported.

- The optical properties of Si_3N_4 have been reported for the first time in the 1-20μm range. In the literature, the refractive index of Si_3N_4 has been reported in the visible to near-IR or ≥1μm.
- The first detailed experimental study on SIMOX has been performed in this work. This is a promising technology for the IC industry. Some of the major wavelengths for operation of the pyrometers in RTP such as 2.5, 2.7 and 3.4μm have proved to be bad choices in the SIMOX case due to interference effects. The study has concluded with suggested wavelengths that will enable the pyrometer to detect enough radiated signal from SIMOX wafers.
- Models that are available commercially or as research tools have been utilized extensively to simulate the optical properties of silicon related materials and structures.

- Novel and innovative wafer emissivity independent temperature measurement techniques have been surveyed.

10.2 Recommendations for Future Work

The work presented in this study has led to the following recommendations for future work:

- A detailed study of the effects of roughness on the optical properties of silicon is required for different degrees of roughness and treatment history. Simulations that are based on statistical random methods such as the Monte-Carlo technique may be appropriate. Such simulations are being incorporated in complex models such as the PV-Optics model by Sopori. This model is currently applicable to wavelengths in the visible-near IR and needs to be extended to the mid-IR.
- Studies that are aimed at obtaining optical constants of silicon such as refractive index n and extinction coefficient k at temperatures above 600°C are required. This is possible using the spectral emissometer but requires an alternative method of heating and possibly the deposition of thin silicon films on transparent substrates such as sapphire or glass in order to maximize the silicon transmittance and to support the thin film.
- A detailed study of the conduction intraband transition that appears in n-Si at all temperatures and in p-Si at the intrinsic regime is required. The band structure needs to be fully accounted for in any model that claims a high accuracy and expects to yield $\pm 2°C/3\sigma$.
- A complete knowledge of the parameters of the Si valence band involved in the calculation of the free carrier absorption coefficient is needed. These parameters include

the conductivity effective mass and the density of state effective mass that are not constants and can change by a factor of 2 as a function of temperature causing a large error in the prediction of α.

- Blackbodies capable of operating at higher temperatures are required to obtain higher signal to noise ratio at the wavelength corresponding to silicon fundamental absorption region in the emissometer.

REFERENCES

[1] P.H. Irving, "Real-time optical thermometry during semiconductor processing.", *IEEE Journal of Selected Topics in Quantum Electronics*, vol. 11, no. 4, pp. 1047-1052, Dec. 1995.

[2] S. Munley and J. Goldman, "Input parameter SPC for diffusion furnaces", *Solid State Technology*, vol. 41, no. 2, pp. 69-74, Feb. 1998.

[3] C. Ratliff, C. Porter, A. Laser and A. Dip, "A fast ramping batch processor for diffusion and oxidation applications", in *Proc. 5th Int. Conf. on Advanced Thermal Processing Semiconductors RTP'97*, New Orleans, Louisiana, Sep. 1997, pp. 55-63.

[4] D. Pattnaik, "Design, fabrication and characterization of silicon microlenses for IR-CCD image sensors", Master Thesis, Dep. Elect. and Comp. Eng., New Jersey Institute of Technology, Newark, New Jersey, May 1998.

[5] D. Lindholm, "Thermal tool requirements and the 1997 national technology roadmap for semiconductors", in *Proc. 5th Int. Conf. on Advanced Thermal Processing of Semiconductors RTP'97*, New Orleans, Louisiana, Sep. 1997, pp. 25-27.

[6] R.B. Fair, *Rapid Thermal Processing Science and Technology*. San Diego, CA: Academic Press, 1993.

[7] W.J. Schaffer, D. Schey, M.L. Bowman, W.A. Mcgahan, J.K. Boisen, Y.E. Strausser and M.E. Bran, "300-mm premetal dielectric processing", *Solid State Technology*, vol. 40, no. 9, pp. 117-126, Sep. 1997.

[8] F. Robertson, "300-mm factory trends", *Solid State Technology*, vol. 40, no. 10, pp. 101-103, Oct. 1997.

[9] S. Myers, " The I300I/J300 joint guidance agreement: its impact on the 300-mm transition", *Solid State Technology*, vol. 40, no. 10, pp. 105-109, Oct. 1997.

[10] E. Ward, R. Howarth, H. Hayes and B. Bracamonte, "Accelerated time to market for future 300-mm fabs", *Solid State Technology*, vol. 40, no. 11, pp. 99-106, Nov. 1997.

[11] A. Bordeaux, "Environmental, health and safety issues for future fabs", *Solid State Technology*, vol. 40, no. 12, pp. 109-112, Dec. 1997.

[12] S. J. Brunkhorst and D.W. Sloat, "The impact of the 300-mm transition on silicon wafer suppliers", *Solid State Technology*, vol. 41, no. 1, pp. 87-90, Jan. 1998.

[13] The National Technology Roadmap for Semiconductors, *Semiconductor Industry Association*, San Jose, California, Dec. 1994.

[14] F. Roozeboom, "History and perspectives of rapid thermal processing", in *Advances in Rapid Thermal and integerated Processing*, Editor F. Roozeboom, Dortdrecht, The Netherlands: Kluwer Academic Publishers, Dordrecht, 1995, pp. 1-34.

[15] N.M. Ravindra, "Rapid thermal processing", *NJIT Research*, vol. 3, pp. 26-34, Spring, 1995.

[16] R. Velagapudi, "Investigation of optical properties of InP, AlN and sapphire for applications in non-contact semiconductor process monitoring", Master Thesis, Dep. Elect. and Comp. Eng., New Jersey Institute of Technology, Newark, New Jersey, Jan. 1998.

[17] N. Hajji and J.E. Spruiell, "Radiation pyrometry of semi transparent sheets I: Gray media", *Polymer Engineering and Science*, vol. 34, no. 2, pp. 116-121, Jan. 1994.

[18] C. Schietinger, "Wafer temperature measurement in RTP", in *Advances in rapid Thermal and Integrated Processing*, edited by F. Roozeboom, Dortdrecht, The Netherlands: Kluwer Academic Publishers, 1995, pp. 103-123.

[19] T.J. Quinn, *Temperature*. New York, NY: Academic Press, 1983.

[20] T. Limperis, and J. Mudar, *The Infrared Handbook*. Editors: W.L. Wolfe, G.J. Zissis, Washington, DC: Office of Naval Research, Dept. of the Navy, 1989, ch. 11, pp. 1-40.

[21] N. M. Ravindra., F.M. Tong, W. Schmidt, W. Chen, S. Abedrabbo, A. Nanda, T. Speranza and A.M. Tello, "Spectral emissometer - A novel diagnostic tool for semiconductor manufacturing", in *Proc. 5th Int. Symp. Semiconductor Manufacturing ISSM'96*, Tokyo, Japan, Oct. 1996, pp. 101-104.

[22] B. Sopori and T. Marshall, "Optical confinement in thin silicon films: A comprehensive ray optical theory", in *Proc. IEEE PVSC*, Louisville, Kentucky, May 1993, pp. 127-132.

[23] P.J. Timans, "Temperature measurement strategies for rapid thermal processing in semiconductor manufacturing", in *Proc. 4th Int. Conf. Advanced Thermal Processing of Semiconductors RTP'96*, Boise, Idaho, Sept. 1996, pp. 145-156.

[24] J.F. Snell, *Handbook of Optics*. Editors: W.G. Driscol and W. Vaughan, New York, NY: McGraw Hill, 1978, pp.1-27.

[25] D. Peyton, H. Kinoshita, G.Q. Lo and D.L. Kwong, " Systems-oriented survey of non-contact temperature measurement techniques for rapid thermal processing", in *Proc. Int. Soc. Optical Eng. SPIE*, edited by R. Singh and M. Moslehi, Oct. 1990, pp. 295-308.

[26] V.M. Donnely and J.A. McCaulley, " Infrared-laser interferometric thermometry: A nonivasive technique for measuring semiconductor wafer temperatures", *J. Vac. Sci. Technol.*, vol. A8, no. 1, pp. 84-92, Jan. 1990.

[27] P.J. Timans, "The role of thermal radiative properties of semiconductor wafers in rapid thermal processing", in *Proc. Mat. Res. Soc.*, vol. 429, 1996, pp. 3-14.

[28] K. Sato, "Spectral emissivity of silicon", *Jpn. J. App. Phys.*, vol. 6, no. 3, pp. 339-347, Mar. 1967.

[29] J.M. Palmer, "The measurement of transmission, absorption, emission, and reflection" , in *Handbok of Optics*. Editors: M. Bass, E.W. Van Stryland, D.R. Williams and W.L. Wolfe, vol. II, New York, NY: McGraw Hill, 1995, ch. 25, pp. 1-25.

[30] F. Abeles, "Optics of thin films", in *Advanced Optical Techniques*. Editor: A.C.S. Van Heel, New York, NY: American Elsevier Publishing Company, Inc., 1967, ch. 5, pp. 145-187.

[31] P. J. Timans, "The thermal radiative properties of semiconductors", in *Advances in Rapid Thermal and Integrated Processing*, Edited by F. Roozeboom, Dordrecht, The Netherlands: Kluwer Academic Publishers, 1996, pp. 35-101.

[32] F.Y. Sorrell, J.A. Harris and R.S. Gyurcsik, "A global model for rapid thermal processors", *IEEE Trans. Semiconductor Manfacturing*, vol. 3, no. 4, pp. 183-188, Nov. 1990.

[33] S. Abedrabbo, N.M. Ravindra, W. Chen, V. Rajasekhar, T. Golota, O.H. Gokce, A.T. Fiory, B. Nguyenphu, A. Nanda, T. Speranza, W. Maszara and G. Williamson, "Temperature dependent emissivity of multilayers on silicon", in *Proc. Mat. Res. Soc.*, vol. 470, 1997, pp. 69-79.

[34] D.W. Pettibone, J.R. Suarez and A. Gat, "The effect of thin dielectric films on the accuracy of pyrometric temperature measurements", in *Proc. Mat. Res. Soc.*, vol. 52, 1986, pp. 209-216.

[35] J. Nulman, B. Cohen, W. Blonigan, S. Antonio, R. Meinecke and A. Gat, "Pyrometric emissivity measurements and compensation in an RTP chamber", in *Proc. Mat. Res. Sos.*, vol. 146, 1989, pp. 461-469.

[36] J. R. Markham K. Kinsella, R.M. Carangelo, C.R. Brouillette, M.D. Carangelo, P.E. Best and P.R. Solomon, "A bench top FT-IR based instrument for simultaneously measuring surface spectral emittance and temperature", *Rev. Sci. Inst.*, vol. 64, no. 9, pp. 2515-2522, Sept. 1993.

[37] D.P. DeWitt, National Institute for Standards and Technology, Gaithesburg, MD, personal communication, Apr. 1997.

[38] P.E. Freeland, "Oxygen percipitaion in silicon at 650°C", *J. Electrochem. Soc.*, vol. 127, pp. 754-756, Mar. 1980.

[39] O.H. Gokce, S. Amin, A. Patel, V. Rajasekhar, S. Abedrabbo and N.M. Ravindra, J.G. Fleming, P.J. Zanzucchi, R.J. Paff and D.J. Szostak, "Effect of annealing on CVD W-Si-N/SiO_2/Si structures", in *Proc. Int. Conf. Advanced Thermal Processing of Semiconductors RTP'97*, New Orleans, Louisiana, Sept. 1997, pp. 412-419.

[40] D. Jenning, "Effect of varying emissivity during titanium silicidation on RTP temperature control", in *Proc. Int. Conf. Advanced Thermal Processing of Semiconductors RTP'97*, New Orleans, Louisiana, Sept. 1997, pp. 217-222.

[41] W.G. Spitzer and H.Y. Fan, "Determination of optical constants and carrier effective mass of semiconductors", *Phys. Rev.*, vol. 106, no. 5, pp. 882-890, June 1957.

[42] Y. Mishima, M. Hirose and Y. Osaka, "Optical determination of mobility and carrier concentration in heavily doped polycrystalline silicon", *J. App. Phys.*, vol. 51, no. 2, Feb. 1980.

[43] J.R. Ferraro and K. Krishnan, Editors, *Practical Fourier Transform Infrared Spectroscopy*. Orlando, FL: Academic Press, 1990.

[44] D. Minkov, R. Swanepoel, "Computerization of the optical characterization of a thin dielectric film", *J. Opt. Eng.* vol. 32, no. 12, pp. 3333-3337, Dec. 1980.

[45] D. Minkov, " Singularity of the solution when using spectrum envelopes for the computation of the optical constants of a thin dielectric layer", *Optik*, vol. 90, no. 2, pp. 80-84, Feb. 1992.

[46] D. Minkov, "Computation of the optical constants of a thin dielectric layer from the envelopes of the transmission spectrum, at inclined of the radiation", *J. Modern Optics*, vol. 37, no. 12, pp. 1977-1986, Dec. 1990.

[47] D. Minkov, "Calculation of the optical constants of a thin layer upon a transparent substrate from the reflection spectrum", *J. Phys. D: Appl. Phys.*, vol. 22, no. 8, pp. 1157-1161, Aug. 1989.

[48] R. Swanepoel, "Transmission and reflection of an absorbing thin film on an absorbing substrate", *South African J. Phys.*, vol. 12, no. 4, pp. 148-156, April 1989.

[49] R. Swanepoel, "Determination of the thickness and optical constants of amorphous silicon", *J. Phys. E: Sci. Instrum.*, vol. 16, no. 12, pp. 1214-1222, Dec. 1983.

[50] R. Swanepoel, "Determination of surface roughness and optical constants of inhomogeneous amorphous silicon films", *J. Phys. E: Sci. Instrum.*, vol. 17, no. 4, pp. 896-903, April 1984.

[51] V.K. Subashiev, G.B. Dubrovskii and A.A. Kukharskii, " Determination of the optical constants and free carrier concentration from the coefficient of reflection in highly doped semiconductor material", *Sov. Phys. - Solid State*, vol. 6, no. 4, pp. 1078-1081, Oct. 1964.

[52] L. Michailovits, M.I. Torok and I. Hevesi, "Extended fringe pattern method for the analysis of the absorption coefficient", *Thin Solid Films*, vol. 139, pp. 143-146, 1986.

[53] D.F. Edwards and E. Ochoa, "Infrared refractive index of silicon", *App. Optics*, vol. 19, no. 24, pp. 4130-4131, Dec. 1980.

[54] A.T. Friberg and I. Kajanto, "Optical measurement of temperature with single-crystal silicon", *Rev. Sci. Instrum.*, vol. 60, no. 8, pp. 2764-2767, Aug. 1989.

[55] G.E. Jellison, Jr. and H.H. Burke, "The temperature dependence of the refractive index of silicon at elevated temperatures at several laser wavelengths", *J. App. Phys.*, vol. 60, no. 2, pp. 841-843, July 1986.

[56] J.C. Sturm, P.V. Schwatz and P.M. Garone, " Silicon temperature measurement by infrared transmission for rapid thermal processing applications", *App. Phys. Lett.*, vol. 56, no. 10, pp. 961-963, Mar. 1990.

[57] A.N. Magunov, "Temperature dependence of the refractive index of silicon single-crystal in the 300-700K range", *Opt. Spectrosc.*, vol. 73, no. 2, pp. 205-206, Aug. 1992.

[58] H.H. Li, "Refractive index of silicon and germanium and its wavelength and temperature dependencies", *J. Phys. Chem. Ref. Data*, vol. 9, p. 561, 1980.

[59] H.J. Goldsmid, R.W. Monk and B.A. Moys, "Incandescence from thin sheets of silicon", *High Temperatures - High Pressures*, vol. 1, pp. 429-436, 1969.

[60] M. Born and E. Wolf, *Principles of Optics*. 4th edition, Oxford, England: Pergamon Press, 1970, pp. 267-333.

[61] E. Yablonovitch and G.D. Cody, "Intensity enhancement in textured optical sheets for solar cells", *IEEE Trans. Elect. Dev.*, vol. ED-29, no.2, pp. 300-305, Feb. 1982.

[62] S. Abedrabbo, J.C. Hensel, O.H. Gokce, F.M. Tong, B. Sopori, A.T. Fiory and N.M. Ravindra, "Issues in emissivity of silicon", in *Proc. Mat. Res. Soc.*, Apr. 1998. (in press)

[63] P. Vandenabeele and K. Maex, "Influence of temperature and backside roughness on the emissivity of Si wafers during rapid thermal processing", *J. Appl. Phys.*, vol. 72, no. 12, pp. 5867-5875, 1992.

[64] P. Vandanabeele and K. Maex, "Emissivity of Silicon Wafers During Rapid Thermal Processing", in *Proc. Int. Soc. Opt. Eng. SPIE*, vol. 1393, Oct. 1990, pp. 316-336.

[65] R.A. Smith, *Semiconductors*. 2nd edition, Cambridge, England: Cambridge University Press, 1961, pp. 216-222.

[66] S. Abedrabbo, J.C. Hensel, A.T. Fiory, B. Sopori, W. Chen and N.M., Ravindra, "Perspectives on emissivity measurements and modeling in silicon", *Materials Science in Semiconductor Processing*, (In press).

[67] D. Redfield, "Multiple-pass thin-film silicon solar cell", *Appl. Phys. Lett.*, vol. 25, pp. 647-648, Dec. 1974.

[68] P. Campbell and M.A. Green, "Light trapping properties of pyramidally textured surfaces", *J. Appl. Phys.*, vol. 62, no. 7, pp. 243-249, July 1987.

[69] B.L. Sopori, J. Madjdpour and C. Gaylord, "PV Optics: Cell and module design", in *Proc. 7th Workshop on the Role of Impurities and Defects in Silicon Device Processing*, Vail, CO, Aug. 1997, pp. 231-232.

[70] N.W. Ashcroft and N.D. Mermin, *Solid State Physics*. Orlando, FL: Saunders Brace College Publishers, 1976, pp. 1-28.

[71] R.E. Hummel, *Electronic Properties of Materials*. New York, NY: Springer Verlag, 1985, pp. 146-164.

[72] H.F. Wolf, *Simiconductors*. New York, NY: Wiley-Interscience, 1971, p. 75.

[73] J.C. Hensel, H. Hasegawa and M. Nakayama, "Cyclotron resonance in uniaxially stressed silicon. II. nature of the covalent bond", *Phys. Rev.*, vol. 138, no. 1A, pp. 225-238, Apr. 1961.

[74] J.C. Hensel and G. Feher, "Cyclotron resonance experiments in uniaxially stressed silicon: valence band inverse mass parameters and deformation potentials", *Phys. Rev.*, vol. 129, pp. 1041-1062, Feb. 1963.

[75] J.C. Sturm and C.M. Reaves, "Silicon temperature measurement by infrared absorption: Fundamental processes and doping effects", *IEEE Trans. Elect. Dev.*, vol. 39, pp. 81-88, Jan. 1992.

[76] J. Hebb and K.F. Jensen, *Multi-Rad User Manual*, Cambridge, MA: MIT, Sponsored by SEMATECH, 1997.

[77] W. Spitzer and H.Y. Fan, "Infrared absorption in n-type silicon", *Phys. Rev.*, vol. 108, no. 2, pp. 268-270, Oct. 1957.

[78] P.J. Timans, "Emissivity of silicon at elevated temperatures", *J. Appl. Phys.*, vol. 74, no. 10, pp. 6353-6364, Nov. 1993.

[79] S.C. Wood, P.P. Apte, T. King, M.M. Moslehi and K.C. Saraswat, "Pyrometry modeling for rapid thermal processing", in *Proc. Int. Soc. Opt. Eng. SPIE*, vol. 1393, Oct. 1990, pp. 337-348.

[80] F.J. Morin and J.P. Maita,"Electrical properties of silicon containing arsenic and boron", *Phys. Rev.*, vol. 96, no. 1, pp. 28-35, Oct. 1954.

[81] W.E. Beadle, J.C.C. Tsai and R.D. Plummer, "Physical properties", in *Quick Reference Manual*. New York, NY: John Wiley & Sons, 1985, ch. 2, pp. 42-43.

[82] H. Brooks, "J3. scattering by ionized impurities in semiconductors", *Phys. Rev.*, vol. 83, pp. 879, 1951.

[83] C. Herring and E. Vogt, "Transport and deformation-potential theory for many-valley semiconductors with anisotropic scattering", *Phys. Rev.*, vol. 101, no. 3, pp. 944-961, Feb. 1956.

[84] J. M. Dorkel and PH. Leturcq, "Carrier mobilities in silicon semi-empirically related to temperature, doping and injected level", *Solid-State Electronics*, vol. 24, no. 9, pp. 821-825, 1981.

[85] H.R. Shanks, P.D. Maycock, P.H. Sidles and G.C. Danielson, "Thermal conductivity of silicon from 300 to 1400 K", *Phys. Rev.*, vol. 130, no. 5, pp. 1743-1748, June 1963.

[86] R.G. Morris and J.J. Martin, "Thermal conductivity measurements of silicon from 680 to 1000 K", *J. App. Phys.*, vol. 34, no. 8, pp. 2388-2389, Aug. 1963.

[87] D.E. Burk, "An empirical fit to Minority hole mobilities", *IEEE Electron Dev. Lett.*, vol. EDL-5, no. 7, pp. 231-233, July 1984.

[88] J. Dziewior and D. Silber, "Minority-carrier diffusion coefficients in highly doped silicon", *App. Phys. Lett.*, vol. 35, no. 2, pp. 170-173, July 1979.

[89] A. Neugroshel, "Minority-carrier diffusion coefficients and mobilities in silicon", *IEEE Electron Dev. Lett.*, vol. EDL-6, no. 8, pp. 425-427, Aug. 1985.

[90] C-T. Sah, P.C.H. Chan, C-K. Wang, R. L-Y.Sah, K. A. Yamakawa and R. Lutwack,"Effect of zinc impurity on silicon solar-Cell efficiency", *IEEE Trans. Electron Dev.*, vol. ED-28, no. 3, pp. 304-312, Mar. 1981.

[91] M. Loung and A. Shaw, "Quantum transport theory of impurity-scattering-limited mobility in n-type semiconductors including electron-electron scattering", *Phys. Rev. B*, vol. 4, no. 8, pp. 2436-2441, Oct. 1971.

[92] N.D. Arora, J.R. Hauserand D.J. Roulston, "Electron and hole mobilities in silicon as a function of concentration and temperature", *IEEE Trans. Electron Dev.*, vol. ED-29, no. 2, pp. 292-769, Feb. 1982.

[93] R.A. Logan and A.J. Peters, "Impurity effects upon mobility in silicon", *J. Appl. Phys.*, vol. 31, no. 1, pp. 122-124, Jan. 1960.

[94] V. Grivitskas and M. Willander, "The role of intercarrier scattering in excited silicon", *Solid-State Electronics*, vol. 27, no. 6, pp. 565-572, June 1984.

[95] P. Norton, T. Braggins and H. Levinstein, "Impurity and lattice scattering parameters as determined from hall and mobility analysis in n-type silicon", *Phys. Rev. B*, vol. 8, no. 12, pp. 5632-5653, Dec. 1973.

[96] W.R. Thurber, R.L. Mattis, Y.M. Liu and J.J. Filliben, "Resistivity-dopant density relationship for boron-doped silicon", *J. Electrochem. Soc.*, vol. 127, no. 10, pp. 2291-2294, Oct. 1980.

[97] S.S. Li, "The dopant density and temperature dependence of hole mobility and resistivity in boron doped silicon", *Solid-State Electronics*, vol. 21, pp. 1109-1117, 1978.

[98] C. Jacoboni, C. Canali, G. Ottaviani and A.A. Quaranta, "A Review of some charge transport properties of silicon", *Solid-State Electronics*, vol. 20, pp. 77-89, 1977.

[99] P.P. Debye and E.M. Conwell, "Electrical properties of n-type germanium", *Phys. Rev.*, vol. 93, no. 4, pp. 693-706, Feb. 1954.

[100] D.B.M. Klaassen,"A unified mobility model for device simulation-I. Model equations and concentration dependence", *Solid-State Electronics*, vol. 35, no. 7, pp. 953-959, July 1992.

[101] D.B.M. Klaassen, "A unified mobility model for device simulation-II. Model temperature dependence of carrier mobility and lifetime", *Solid-State Electronics*, vol. 35, no. 7, pp. 961-967, July 1992.

[102] H.Y. Fan, M.L. Shepherd and W.G. Spitzer, "Infrared absorption and energy-Band strucutre of germanium and silicon", in *Proc. A.C. Photoconductivity Conf.*, New York, NY: John-Wiley & Sons, Inc., 1956, pp. 184-203.

[103] J. Kuehne and S. Hattangady, "Kinetics, chemical composition and reoxidation kinetics of rapid thermal N_2O oxynitrides growth", in *Proc. 4th Int. Conf. Rapid Thermal Processing RTP'96*, Boise, Idaho, Sep. 1996, pp. 207-211.

[104] S.P. Tay, Y.Z. Hu and Y. Wasserman, "Manufacturability of rapid thermal N_2O oxynitridation for ultrthin gate dielectrics in 0.25mm CMOS process and beyond", in *Proc. 5th Int. Conf. Rapid Thermal Processing RTP'97*, New Orleans, Louisiana, Sep. 1997, pp. 129-134.

[105] G.C. Xing, D. Lopes and G.E. Miner, "The study of N_2O oxidation uniformities of RTP centura rapid thermal processing", in *Proc. 5th Int. Conf. Rapid Thermal Processing RTP'97*, New Orleans, Louisiana, Sep. 1997, pp. 155-162.

[106] T. Chu, C. Lee and G. Gruber, "The properties of amorphous silicon nitride films", *J. Electrochem. Soc.*, vol. 114, no. 7, pp. 717-722, July 1967.

[107] E.A. Taft, "Characterization of silicon nitride films", *J. Electrochem. Soc.*, vol. 118, no. 8, pp. 1341-1346, Aug. 1971.

[108] H.R. Philipp, "Optical functions of amorphous Si_3N_4", in *Properties of Silicon*. By INSPEC, The Institution of Electrical Engineers, Old Woking, Surray, England: The Gresham Press, Sep. 1987, pp. 1034-1036.

[109] N.M. Ravindra, S. Abedrabbo, W. Chen, F.M. Tong, A.K. Nanda and T. Speranza, "Temperature dependent emissivity of silicon related materials & structures", *IEEE Transactions on Semiconductor Manufacturing*, vol. 11, no. 1, pp. 30-39, Feb. 1998.

[110] P.J. Ashby, "IR absorption due to N in Si", in *Properties of Silicon*. By INSPEC, The Institution of Electrical Engineers, Old Woking, Surray, England: The Gresham Press, July 1987, pp. 321-323.

[111] A. Bellaouar and M.I. Elmasry, "Low power digital VLSI design: circuits and systems", second edition, Norwell, MA: Kluwer Academic Publishers, 1996, pp. 13-62.

[112] L. Geppert, "Solid state", *IEEE Spectrum*, vol. 35, no. 1, pp. 23-28, Jan. 1998.

[113] J. Nulman, S. Antonio and W. Blonigan, "Observation of silicon wafer emissivity in rapid thermal processing chambers for pyrometric temperature monitoring", *Appl. Phys. Lett.*, vol. 56, no. 25, pp. 2513-2515, June 1990.

[114] N. M. Ravindra., F.M. Tong, S. Abedrabbo, W. Chen, A. Schmidt, A. Nanda, T.Speranza and A.M. Tello, "Applications of spectral emissometry to silicon related materials", in *Proc. 4th Int. Conf. Rapid Thermal Processing RTP'96*, Boise, Idaho, Sept. 1996, pp. 190-204.

[115] R. Schork and H. Ryssel, "Formation of ultra thin SOI-layer by implantation of nitrogen", in *Proc. IEEE Intl. SOI Conf.*, Apr. 1992, pp. 16-20.

[116] I.P. Lisovskii, A.G. Revesz and H.L. Hughes, "Infrared absorption study of buried oxide of single and triple-implanted SIMOX structures", in *Proc. 7th Int. Symp. Silicon-on-Insulator Technology and Devices*, May 1996, pp. 133-141.

[117] A.H. Jayatissa, " Spectroscopic ellipsometry of SIMOX (separation by implanted oxygen) : Thickness distribution of buried oxide and optical properties of top - Si layer", *Jpn. J. Appl. Phys.*, vol. 36, no. 5A, part 1, pp. 2581-2586, 1997.

[118] N.M. Ravindra, O.H. Gokce, F.M. Tong, S. Abedrabbo, V. Rajasekhar, A. Patel, G. Williamson, W. Maszara, A. Nanda and T. Speranza, "Temperature and wavelength dependent emissivity of SIMOX", in *Proc. 3rd Int. Workshop on Thermal Investigation of Ics and Microstructures*, Cannes, France, 1997, pp. 40-42.

[119] N.M. Ravindra, S. Abedrabbo, O.H. Gokce, F.M. Tong, A. Patel, V. Rajasekhar, G. Williamson and W. Maszara, "Radiative properties of SIMOX", *IEEE Transactions on Components, Packaging, and Manufacturing Technology*, Sept. 1998 (In press).

[120] J.D. Jackson, *Classical Electrodynamics*. New York, NY: John-Wiley & Sons, Inc., 1975, pp. 269-327.

[121] M. Born and E. Wolf, *Principles of Optics*. 4th edition, Oxford, England: Pergamon Press, 1970, pp. 1-70.

[122] E. Hecht and A. Zajak, *Optics*. Reading, MA: Addison Wesley, 1974, pp. 312-316.

[123] H.A. Macleod, *Thin Film Optical Filters*. New York, NY: Mcgraw-Hill, 1986, pp. 11-48.

[124] K.D. Moeller, *Optics*. Mill Valley, CA: University Science Books, 1988, pp. 206-212.

[125] T.S. Moss, G.J. Burrell and B. Ellis, *Semiconductor Opto-Electronics*. New York, NY: John Wiley & Sons, INC., 1973, pp. 297-300.

[126] N. M. Ravindra, W. Chen, F.M. Tong and Arun Nanda, "Emissivity measurements and modeling - an overview", in *Transient Thermal Processing Techniques in Electronic Materials*, edited by N. M. Ravindra and R.K. Singh, Warrendale, PA: TMS-The Minerals, Metals, Materials Society, Aug. 1996, pp. 159-164.

[127] G.G. Macfarlane, T.P. Mclean, J.E. Quarrington and V. Roberts, "Fine structure in the absorption-edge spectrum of Si", *Phys. Rev.*, vol. 111, no. 5, pp. 1245-1254, 1958.

[128] F. Abeles, "Investigation on the propagation of sinusoidal electromagnetic waves in statified media. Application to thin films", Ann. de Physique, vol. 5, pp. 596-640, 1950.

[129] R. Jacobsson, *Progress in Optics*. Editor: E. Wolf, vol. 5, Amsterdam, Holland: North Holland Publishing, 1965, p. 247.

[130] A.T. Fiory, Bell Laboratories, Lucent Technologies, Murray Hill, NJ, personal communication, Mar. 1997.

[131] P.J. Timans, "Temperature measurement in rapid thermal processing", *Solid State Technology*, vol. 40, no. 4, pp. 63-74, Apr. 1997.

[132] Z. Atzmon, Z. Doitel, A. Harnik, S. Levi, A. Thon, P. Alezra and H. Gilboa, "Rapid thermal CVD with emissivity-independent temperature sensing system", in *Proc. 5th Int. Conf. Rapid Thermal Processing RTP'97*, Louisiana, New Orleans, Sept. 1997, pp. 114-117.